

SYNTHESIS, CHEMISTRY AND STRUCTURE OF BORON-DOPED
CARBON NANOTUBES AND NANOFIBERS

BY
LING WANG

A THESIS
SUBMITTED TO THE FACULTY OF
ALFRED UNIVERSITY

IN PARTIAL FULFILLMENT OF THE REQUIREMENTS
FOR THE DEGREE OF
DOCTOR OF PHILOSOPHY
IN
MATERIALS SCIENCE AND ENGINEERING

ALFRED, NEW YORK

DECEMBER, 2006

Alfred University theses are copyright protected and may be used for education or personal research only. Reproduction or distribution in part or whole is prohibited without written permission from the author.

SYNTHESIS, CHEMISTRY AND STRUCTURE OF BORON-DOPED
CARBON NANOTUBES AND NANOFIBERS

BY

LING WANG

B.S. NATIONAL UNIVERSITY OF
DEFENCE TECHNOLOGY, CHINA (1994)

M.S. NATIONAL UNIVERSITY OF
DEFENCE TECHNOLOGY, CHINA (1998)

SIGNATURE OF AUTHOR _____ (Signature on file)

APPROVED BY _____ (Signature on file)
LINDA E. JONES, ADVISOR

(Signature on file)
VASANTHA R. W. AMARAKOON,
ADVISORY COMMITTEE

(Signature on file)
ALASTAIR N. CORMACK, ADVISORY COMMITTEE

(Signature on file)
DOREEN D. EDWARDS, ADVISORY COMMITTEE

(Signature on file)
WALTER A. SCHULZE, CHAIR,
ORAL THESIS DEFENSE

ACCEPTED BY _____ (Signature on file)
ALASTAIR N. CORMACK, DEAN,
KAZUO INAMORI SCHOOL OF ENGINEERING

ACCEPTED BY _____ (Signature on file)
WILLIAM M. HALL, ASSOCIATE PROVOST FOR
GRADUATE AND PROFESSIONAL PROGRAMS
ALFRED UNIVERSITY

ACKNOWLEDGMENT

I would like to express my deepest appreciation to my advisor, Dr. Linda Jones. Her guidance, encouragement, patience and support throughout my years in Alfred not only made this thesis possible but also will inspire me in my future careers and life.

I appreciate the efforts of my thesis committee, Dr. Cormack, Dr. Amarakoon and Dr. Edwards, who made important suggestions for this thesis in record time. I would like to thank Dr. Schulze for his friendly support and discussion. I would also like to take this opportunity to show my great gratitude to Chris Maier, my colleague and comrade, for his tremendous help and support.

My financial support, which was arranged by Dr. Jones and Dr. Edwards, came from the Kazuo Inamori School of Engineering at Alfred University. Part of this research project was conducted through the High Temperature Material Laboratory User Program at Oak Ridge National Laboratory, sponsored by the U.S. Department of Energy under the contract HTML 2006-012.

A sincerest Thank You goes to the great group of scientists at Oak Ridge National Laboratory, especially to Dr. Jane Howe for arranging my visit.

Many thanks to the people who make Alfred a home: Diane Cox, Susan Meacham, and Sheila Foreman. Also thanks to my local Chinese folks at Alfred: Wei Yang and Yuefei Gong.

Last, but not least, my gratitude goes to my husband, Liwei, for his understanding and inspiration....thank you.

TABLE OF CONTENTS

	Page
ACKNOWLEDGMENTS.....	iii
TABLE OF CONTENTS.....	iv
LIST OF TABLES.....	vii
LIST OF FIGURES.....	viii
ABSTRACT.....	xiii
1 INTRODUCTION.....	1-1
2 X-RAY DIFFRACTION FROM UNIRRADIATED NUCLEAR GRAPHITES.....	2-1
2.1 Introduction.....	2-1
2.2 Materials, Experimental, and Data Analysis	2-3
2.2.1 Materials	2-3
2.2.2 X-ray Diffraction	2-3
2.2.3 Data Analysis.....	2-3
2.3 Results and Discussion.....	2-6
2.3.1 Crystal Structure of Unirradiated Nuclear Graphites.....	2-6
2.3.2 X-ray Diffraction Approach on Carbon.....	2-8
2.4 Conclusions.....	2-10
References.....	2-11
3 COMPUTER SIMULATION: INFLUENCE OF BORON ON CARBON NANOTUBE STRUCTURE.....	3-1
3.1 Introduction.....	3-1
3.2 Background.....	3-2
3.3 Experimental Procedures.....	3-5
3.3.1 Computer Modeling of Structure	3-5
3.3.2 Synthesis of Boron-doped Carbon Nanotubes.....	3-6
3.3.3 Transmission Electron Microscopy.....	3-6
3.4 Results and Discussion.....	3-7
3.4.1 Modeling of Boron-doped Carbon Lattice.....	3-7

3.4.2 Boron-doped Carbon Nanotubes via CVD Process.....	3-12
3.5 Conclusions.....	3-14
References.....	3-15
4 SYNTHESIS OF BORON-DOPED CARBON NANOTUBES AND	
NANOFIBERS.....	4-1
4.1 Introduction.....	4-1
4.2 Experimental Procedures.....	4-3
4.2.1 Synthesis of Boron-doped Nanofibers via CVD Process.....	4-3
4.2.2 Scanning Electron Microscopy and Energy Dispersive Spectroscopy	4-5
4.2.3 Thermodynamic Calculations Using FactSage Software.....	4-5
4.3 Results and Discussion.....	4-6
4.3.1 Influence of Catalysts.....	4-6
4.3.1.1 Ferrocene as the Catalyst Precursor	4-7
4.3.1.2 Metal Particles as the Supported Catalyst.....	4-11
4.3.1.3 Properties of Nickel Nanoparticles.....	4-21
4.3.2 Pyrolysis of Benzene.....	4-25
4.3.3 Carrier Gas Selection.....	4-28
4.3.4 Deposition Conditions.....	4-31
4.3.4.1 Deposition Temperature.....	4-31
4.3.4.2 Deposition Duration.....	4-33
4.3.4.3 Reactant Ratio of BCl ₃ /C ₆ H ₆	4-34
4.3.5 Growth Mode of the Boron-doped Nanofibers.....	4-37
4.4 Conclusions.....	4-40
References.....	4-41
5 CHEMISTRY OF BORON-DOPED CARBON NANOTUBES AND	
NANOFIBERS.....	5-1
5.1 Introduction.....	5-1
5.2 Background.....	5-5
5.2.1 XPS Studies on Boron-carbon Materials.....	5-5
5.2.2 AES Studies on Boron-carbon Materials.....	5-7
5.3 Experimental Procedures.....	5-9

5.3.1	Synthesis of Carbon and Boron-doped Carbon Nanofibers.....	5-9
5.3.2	XPS and AES.....	5-9
5.4	Results and Discussion.....	5-11
5.4.1	Chemical Compositions of Boron-doped Carbon Nanofibers.....	5-11
5.4.2	Chemical State of B and C in Boron-doped Carbon Nanofibers.....	5-19
5.5	Conclusions.....	5-25
	References.....	5-26
6	STRUCTURE AND STRUCTURE-RELATED CHEMISTRY OF BORON-DOPED CARBON NANOTUBES AND NANOFIBERS.....	6-1
6.1	Introduction.....	6-1
6.2	Experimental Procedures.....	6-3
6.2.1	X-Ray Diffraction.....	6-3
6.2.2	Raman Spectroscopy.....	6-4
6.2.3	High-resolution Transmission Electron Microscopy.....	6-4
6.2.4	Electron Energy-Loss Spectroscopy.....	6-4
6.3	Results and Discussion.....	6-6
6.3.1	Structure Analysis of Boron-doped Carbon Nanofibers.....	6-6
6.3.1.1	X-ray Diffraction Study.....	6-6
6.3.1.2	Raman Spectroscopy.....	6-9
6.3.1.3	Transmission Electron Microscopy.....	6-17
6.3.2	Structure-related Chemistry Analysis of Boron-doped Carbon Nanofibers.....	6-33
6.3.2.1	A Background of the EELS Combined with Z-contrast Imaging.....	6-33
6.3.2.2	EELS Analysis of Boron-doped Carbon Nanofibers.....	6-35
6.3.2.2.1	Nanofibers of Sample I-1.....	6-35
6.3.2.2.2	Nanofibers of Sample II-750C.....	6-45
6.3.2.3	Structure-related Chemistry in Boron-doped Carbon Nanofibers.....	6-49
6.3.3	Growth Mechanism of Boron-doped Carbon Nanofibers.....	6-53
6.4	Conclusions.....	6-56

References.....	6-58
7 CONCLUSIONS.....	7-1
APPENDIX.....	A-1

LIST OF TABLES

	Page
Table 2.1 Exact Peak Positions for Si SMR 640b and Graphite SP-1 Peaks.....	2-4
Table 2.2 Lattice Parameter and Crystallite Size Results for SP-1 and Irradiated Nuclear Graphites.....	2-7
Table 3.1 Total Energy and Linear Strains Associated with a Circumcorene Host Molecule Containing 11 at.% Boron.....	3-9
Table 4.1 Physico-chemical Properties of Selected Transition Metals.....	4-12
Table 4.2 Thermodynamic Calculations of Equilibrium Reactions at 800°C and 101.3kPa.....	4-14
Table 5.1 Summary of the Literature Assignments for the Components of the B _{1s} and C _{1s} XPS Spectra.....	5-6
Table 5.2 Chemical Compositions of Boron-doped Carbon Nanofibers by XPS and AES Analysis.....	5-12
Table 5.3 Atom Ratios of Boron-doped Nanofibers by AES Analysis and TEM/EDS Analysis.....	5-17
Table 6.1 XRD Analysis of Boron-doped Carbon Nanofibers.....	6-8
Table 6.2 Raman Analyses on Boron-doped Carbon Nanofibers.....	6-15
Table 6.3 TEM Observations on Boron-doped Carbon Deposits.....	6-20

LIST OF FIGURES

Figure 2.1.	X-ray powder diffraction patterns of SP-1 and unirradiated nuclear graphite samples along with the silicon standard.....	2-6
Figure 3.1.	The influence of 11% boron symmetrically distributed with a circumcoronene (C ₅₄ H ₁₈) host molecule on the out-of-plane distortion, δ	3-8
Figure 3.2.	The influence of 11% boron asymmetrically distributed within a circumcoronene (C ₅₄ H ₁₈) host molecule.....	3-9
Figure 3.3.	Influence of boron concentration on the distortion of the 17% boron-doped graphite layer plane.....	3-11
Figure 3.4.	17% boron symmetrically distributed modifies the dimensions of a (9,0) nanotube.....	3-12
Figure 3.5.	Bright-field TEM image and the electron diffraction pattern of a boron-doped filament deposited at 800°C for 30min.....	3-13
Figure 4.1.	Schematic of the CVD reactor for the boron-doped carbon nanofibers....	4-4
Figure 4.2.	The microstructure of diamond microcrystals deposited at 800°C for 15min using ferrocene as the catalyst.....	4-9
Figure 4.3.	The microstructure of diamond microcrystals and nanofibers deposited at 800°C for 30min using ferrocene as the catalyst.....	4-10
Figure 4.4.	Change of the microstructure of a single diamond microcrystal with the CVD deposition time.....	4-10
Figure 4.5.	The SEM image and EDS spectrum of the deposit using Cu film as the catalyst.....	4-14
Figure 4.6.	The SEM images of the deposit using chromium film as the catalyst....	4-15
Figure 4.7.	The SEM image and EDS spectra of the deposit using iron film (~4nm thick) as the catalyst.....	4-16
Figure 4.8.	The SEM images of the deposit using nickel film (~5 nm thick) as the catalyst.....	4-17

Figure 4.9. The SEM images of the deposit using nickel powder as the catalyst....	4-20
Figure 4.10. Melting point of nickel as a function of particle diameter.....	4-22
Figure 4.11. Solubility of carbon in nickel at 101.3kPa as a function of temperature	4-23
Figure 4.12. Carbon solubility in nickel at melting point as a function of particle size.....	4-23
Figure 4.13. Thermodynamic calculations of ΔG for benzene decomposition.....	4-27
Figure 4.14. Thermodynamic calculations of ΔG for isothermal equilibrium systems at an atmospheric pressure starting with the reactant of (a) 1mol C_6H_6 , and (b) 1mol C_6H_6 with 1 mol BCl_3	4-28
Figure 4.15. The microstructures of boron-doped carbon film deposited using (a) He and (b) H_2 as carrier gas.....	4-30
Figure 4.16. Change of the microstructure of boron-doped carbon nanofibers with the increase in deposition temperature.....	4-32
Figure 4.17. Microstructure of boron-doped carbon fibers deposited at (a) $800^\circ C$ for 60min and (b) $850^\circ C$ for 60min.....	4-33
Figure 4.18. Change of the microstructure of boron-doped carbon nanofibers with the change in reactant ratio BCl_3/C_6H_6	4-35
Figure 4.19. Change of the microstructure of boron-doped carbon nanofibers with the change in reactant ratio BCl_3/C_6H_6	4-36
Figure 4.20. Two growth modes of carbon nanotubes or nanofibers, namely tip or base growth, resulting from different catalyst-support interaction...	4-39
Figure 4.19. SEM images of boron-doped carbon nanofibers deposited at $800^\circ C$ for 30 min using Ni film as the catalyst.....	4-39
Figure 5.1. Fine structures of the carbon Auger spectra from diamond, graphite, and amorphous carbon.....	5-8
Figure 5.2. Boron concentration of nanofibers of Group I as a function of the deposition temperature.....	5-13
Figure 5.3. High-resolution TEM images of platelet and herringbone or tubular nanofibers.....	5-14

Figure 5.4.	The C1s and B1s XPS spectra of boron-doped carbon nanofibers deposited at reactant ratios of $\text{BCl}_3/\text{C}_6\text{H}_6$ between 0.5 and 2.....	5-19
Figure 5.5.	The C1s and B1s XPS spectra of boron-doped carbon nanofibers deposited at temperatures between 750°C and 900°C	5-20
Figure 5.6.	The C (<i>KVV</i>) and B (<i>KVV</i>) Auger peaks of boron-doped carbon nanofibers deposited at reactant ratios, $\text{BCl}_3/\text{C}_6\text{H}_6$, between 0.5 and 2.....	5-23
Figure 5.7.	The C (<i>KVV</i>) and B (<i>KVV</i>) Auger peaks of boron-doped carbon nanofibers deposited at temperature between 750 and 900°C	5-24
Figure 6.1.	Three structural types of carbon filaments, classified by the angle of graphene layers with respect to the filament axis.....	6-2
Figure 6.2.	XRD patterns of boron-doped carbon nanofibers deposited with the reactant ratios $\text{BCl}_3/\text{C}_6\text{H}_6 = 0.5, 1, \text{ and } 2$	6-7
Figure 6.3.	XRD patterns of boron-doped carbon nanofibers deposited at temperatures of 750°C , 800°C and 850°C	6-7
Figure 6.4.	Raman Spectra of boron-doped carbon nanofibers deposited with the reactant ratios $\text{BCl}_3/\text{C}_6\text{H}_6 = 0.5, 1, \text{ and } 2$ at 800°C for 30 min.....	6-13
Figure 6.5.	Raman Spectra of boron-doped carbon nanofibers deposited at temperatures from $750\text{-}900^\circ\text{C}$ with a reactant ratios $\text{BCl}_3/\text{C}_6\text{H}_6 = 1$	6-14
Figure 6.6.	Planar crystallite size L_a as a function of deposition temperatures.....	6-15
Figure 6.7.	TEM images of Sample I-0.5.....	6-21
Figure 6.8.	TEM images of Sample I-1.....	6-22
Figure 6.9.	TEM images of Sample I-2.....	6-24
Figure 6.10.	TEM images of a nanofiber with a broken tip in Sample II-750.....	6-25
Figure 6.11.	TEM images of a boron-doped carbon nanofiber with a closed tip in Sample II-750C.....	6-26
Figure 6.12.	TEM images of Sample II-800C.....	6-27
Figure 6.13.	TEM images of a boron-doped carbon fiber of Sample II-850C.....	6-28
Figure 6.14.	TEM images of the fragments of Sample II-900C.....	6-29

Figure 6.15. Schematic diagram of the Z-contrast imaging using high-angle scattering and EELS in STEM.....	6-34
Figure 6.16. A Z-contrast image of a nanofiber with a diameter of 60 nm in Sample I-1.....	6-36
Figure 6.17. The integration intensity profiles of B, C and O K-edges of Scan A and Scan B perpendicular across a nanofiber in Sample I-1.....	6-37
Figure 6.18. The profiles of average atom ratios of B/C and O/C of Scan A and Scan B.....	6-39
Figure 6.19. Nanofiber cross-section models built up based on the carbon profiles for Scan A and (b) Scan B of a nanofiber in Sample I-1.....	6-41
Figure 6.20. The profiles of calculated B/C atom ratios based on the nanofiber models of (a) Scan A and (b) Scan B.....	6-43
Figure 6.21. Models of boron distribution in the nanofiber of Sample I-1.....	6-44
Figure 6.22. A Z-contrast image of a nanofiber with a diameter of 80 nm in Sample II-750C.....	6-46
Figure 6.23. The integration intensity profiles of B and C K-edges of Scan C across a nanofiber in Sample II-750C.....	6-46
Figure 6.24. The profile of average B/C atom ratio of Scan C on a nanofiber in Sample II-750C.....	6-47
Figure 6.25. The nanofiber model and calculated radial boron distribution in a nanofiber of Sample II-750C.....	6-48
Figure 6.26. The relationship between the structure and the boron distribution in a nanofiber of Sample I-1.....	6-51
Figure 6.27. The relationship between the structure and the boron distribution in a nanofiber of Sample II-750.....	6-52
Figure 6.28. Schematic representation of the mechanism of boron-doped carbon nanofiber formation.....	6-54

ABSTRACT

The objective of this project is to synthesize novel boron-rich carbon in the form of nanotubes and nanofibers and to determine the influence of high concentrations of boron on the sp^2 carbon structure. Research efforts on the influence of high concentrations of boron on the sp^2 carbon structure have been undertaken through a combination of computational prediction and experimental investigation.

A theoretical prediction regarding the boron influence on carbon nanotube structure is carried out using molecular and quantum mechanical simulations. The influence of substitutional boron on strain, tube diameter, tube length and tube stability is discussed. A high boron doping (10-17 at.%) introduces disorder into the host sp^2 carbon structure.

Boron-doped carbon nanotubes and nanofibers have been synthesized by a catalytic CVD at 750-900°C from C_6H_6 and BCl_3 . The deposition temperature and reactant ratio (BCl_3/C_6H_6) influence the microstructure and compositions of the resulting deposits significantly. The boron concentrations of the boron-doped carbon nanotubes and nanofibers are in the range of 5-18 at.% as measured by AES. The optimum temperature to obtain a high boron content sample is around 800°C. XPS and Auger analyses suggest that the C-B bonding is sp^2 hybridized and includes B-BC₂ and B-C₃. Small clusters of boron atoms may be present in the nanofibers deposited at high temperatures that may contribute to disorder/strain within the nanotube and nanofiber structure.

The crystal structures and microstructures of boron-doped carbon nanotubes and nanofibers are inhomogeneous. There are mixed crystallite sizes of both L_a and L_c . Strains occur in the samples synthesized at low temperature (750°C), and lead to a small lattice parameter, d_{002} . Submicron fibers and nanofibers coexist in each sample. The texture of filamentous carbon changes with the change in boron concentrations or deposition temperatures.

The boron doping into the carbon nanotubes and nanofibers is structure-related. The platelet stacked structure is always very well-ordered with very low boron concentration (< 2% B/C). Herringbone structures are ordered with relatively low boron concentration (2-8% B/C). The tubular structure is either ordered with a B/C ratio of 3-8% B/C, or turbostratic with a B/C ratio of > 8%. A disordered transition area between herringbone and tubular structure in a nanofiber of Sample I-1 is observed where the boron concentration is 16%, i.e., consistent with a composition of C_6B .

Mechanisms of boron-doped nanofiber growth are proposed that involve both surface diffusion and bulk diffusion process. Temperature is the governing factor that determines the process by which either surface diffusion or bulk diffusion dominates. Boron doping also influences the ordering of the carbon layer plane stacking.

1 Introduction

A new direction in the science of carbon nanotube chemistry is the synthesis of structures that are doped with high levels of boron. The incorporation of boron into bulk carbon (e.g. bulk graphites, carbon fiber, carbon-carbon composites, etc.) has been found to significantly enhance the oxidation resistance of the host material, as well as to modify mechanical and electronic properties. If the nanotubes (or nanofibers) are doped with boron, the electronic properties will be different from a doped bulk carbon material. The quantum confinement, and curvature of the cylinder, will result in novel electronic, mechanical, and chemical properties. In particular, substitutional boron doping will introduce strongly localized electronic features in the valence band, and enhance the number of the electronic states at the Fermi level, depending on the location and concentration of boron.

Several potential applications of boron-doped carbon nanotubes and nanofibers are currently being researched: (1) field-emission source materials, owing to enhanced electron mobility as compared to pure carbon nanotubes, (2) boron-doped carbon nanofibers for superior anode material performance in Li^+ ion batteries, (3) efficient sensors for the detection of hazardous gaseous species due to the presence of increased reactive sites on their surface, and (4) nanotube (or nanofiber) composites that exhibit stable tube surface-polymer interfaces.

The objective of the present study is to synthesize novel boron-rich carbon in the form of nanotubes and nanofibers and to determine the influence of high concentrations of boron on the sp^2 carbon structure.

This thesis is prepared in a publication format, including five independent papers. Each paper contains its own literature review/background, experimental procedures, results and discussion, conclusions and list of references. Chapter 2 is the first paper, presenting our initial work on the crystal structure of sp^2 carbon using X-ray diffraction (XRD). XRD has been well established as the most available and powerful technique to measure the crystal structure of sp^2 carbon (graphite). Chapter 2 addresses how to accurately analyze the XRD data and how to correctly report the graphite crystal structure.

In Chapter 3 (Paper 2), a theoretical prediction regarding the boron influence on carbon nanotube structure is carried out before the experimental investigation. Molecular and quantum mechanical simulations are applied to explore the influence of substitutional boron on strain, tube diameter, tube length and tube stability.

Chapter 4 (Paper 3) details the synthesis of boron-doped carbon nanotubes and nanofibers using chemical vapor deposition (CVD) processes. It includes an extensive investigation of the experimental parameters associated with CVD process. The advantage of the CVD process is that it enables high concentrations of boron to be placed in the solid throughout its growth process. The investigated experimental parameters include the influence of catalysts, the pyrolysis of benzene, the influence of the carrier gas, and the deposition conditions (deposition temperature, duration, and reactant ratio). An optimum reaction

condition is identified with regard to the boron concentration and resultant microstructure/morphology. The growth mode of boron-doped carbon nanofiber is discussed on the basis of microstructural observations.

Chapter 5 (Paper 4) presents an analysis of the chemistry of these deposited nanofibers undertaken by both X-ray photoelectron spectroscopy (XPS) and Auger electron spectroscopy (AES). The compositions and chemical state of boron and carbon atoms in these novel nanofibers are reported and discussed in detail. The boron concentrations of the nanofibers range from 5-18 at.%, as determined jointly by both XPS and AES, which further supports that this particular CVD process is an effective method to synthesize highly boron-rich carbon nano-structures, as compared to what may be achieved by other solid-state methods.

Chapter 6 (Paper 5) addresses the crystal and nano-scaled structure of the deposited nanofibers. We have had the opportunity to use the HTML User facility in Oak Ridge National Laboratory (HTML User Proposal # 2006-012). Detailed examination of the nano-structure of boron-doped carbon nanofibers is carried out using high-resolution transmission electron microscopy (TEM). In this paper, we argue that the structure of deposited nanofibers is inhomogeneous. The doping of boron atoms influences not only the ordering of the carbon layer stacking, but also the structural type (i.e., texture) as well. The local structure is intimately correlated with the boron distribution in the nanofibers. Therefore, a chemical analysis by electron energy-loss spectroscopy (EELS) combined with Z-contrast imaging is undertaken, which provides chemical analysis at the atomic level. These results reveal the structure-related chemistry in boron-doped carbon

nanofibers. Finally, growth mechanisms are proposed that potentially provide effective control on the structure and chemistry of boron-doped carbon nanofibers.

2 X-Ray Diffraction from Unirradiated Nuclear Graphites

2.1 Introduction

Graphite is used in large concentrations for the production of many safety critical and lifetime limiting components in nuclear reactors because of low absorption of neutrons, high thermal conductivity and high-temperature strength and stability. Graphite is used as a moderator, which sustains the nuclear fission chain reaction. The moderator's role is so critical that its operating life essentially governs the working life of the power plant. Graphite used in nuclear reactors is high purity synthetic graphite known as electrographite, having a polycrystalline structure with crystals held together by a binder phase. This graphite is simply referred to as "nuclear graphite" in the industry. During operation, many of the graphite's physical properties are significantly changed due to the irradiation-induced damage. These changes are complex and not fully understood; however, we can improve the component performance by specifying properties of the nuclear graphite. There are several general requirements for nuclear graphite, including density ($\sim 1.8 \text{ g/cm}^3$), crystallinity, coefficient of thermal expansion, CTE, ($2.0\text{-}5.5 \times 10^{-6} \text{ K}^{-1}$), and strength ($\sim 20 \text{ MPa}$). Additionally, high chemical purity, low reactivity in moisture (0.2 to 0.01 mg/g-h), and low absorption cross-section (4-5 mbarns) are desired.¹ Among these properties, crystallinity is of great importance. Crystallinity influences thermal conductivity, irradiation-induced modifications, dimension stability, and machinability. Crystal structure can be connected to impurity content. For this reason, measurement of the crystal structure of nuclear graphite is essential to characterize the working potential of this material. X-ray powder diffraction has been well established as the most available and powerful technique to measure the crystal structure of graphite, such as interlayer spacing (d_{002}), lattice parameters (a and c), and crystallite sizes (L_a and L_c).

The graphite crystal is hexagonal. Covalent C-C bonds exist within the basal sheet structure, while the basal planes are held together in parallel by relatively weak van der Waals forces. The space group is $P6_3/mmc$, and the lattice parameters are $a=2.461 \text{ \AA}$ and $c=6.707 \text{ \AA}$ for a perfect graphite crystal.² It is well accepted that the interlayer spacing of graphite (d_{002}) decreases as the degree of crystallinity increases.^{3,4} Graphite SP-1 is a commercially available well-crystallized graphite with a crystal size of more than 1000 \AA .⁵ According to Howe, Rawn, and Jones, SP-1 has an interlayer spacing of 3.355 \AA and a lattice parameter of $a=2.4617(2) \text{ \AA}$ and $c=6.7106(4) \text{ \AA}$.⁶ SP-1 has been frequently referenced as a standard for well-crystallized graphite. The select area electron diffraction study indicates that, in most case, each flake of SP-1 is single crystal graphite.⁴ Generally, a structure with crystallite size of L_a and L_c between 400 and 800 \AA is considered well graphitized.⁷

It is difficult to obtain high quality data for graphite using X-ray powder diffraction. Carbon has a very low mass absorption coefficient for X-rays, which results in errors associated with peak displacement and peak broadening. The systematic broadening in the forward reflection region due to sample transparency will be asymmetric on the left (low 2θ) side of the peak.⁸ Additionally, preferred orientation effects due to the basal sheet structure of graphite crystal will cause the diffraction intensity distortion. In order to correct these problems, a silicon standard is used to correct the peak position and graphite SP-1 is used to correct systematic line broadening, respectively.

In 2004, Iwashita, Park, Fujimoto, Shiraishi and Inagaki specified a standard approach for X-ray diffraction measurements on carbon materials.⁹ This specification is recognized and there is a need to adopt a standard approach worldwide. Comparing Iwashita's work against an approach used in our lab, we discuss the differences.

2.2 Materials, Experimental, and Data Analysis

2.2.1 Materials

Samples are unirradiated nuclear graphite powder as received from GrafTech International Ltd. The three samples are Graphite SS (isotropic, $\text{CTE}=4.4\times 10^{-6} \text{ K}^{-1}$), Graphite PCEA (semi-isotropic, $\text{CTE}=3.5\times 10^{-6} \text{ K}^{-1}$), and Graphite SE (anisotropic, $\text{CTE} = 0.9\times 10^{-6} \text{ K}^{-1}$), respectively. All samples have a mean diameter of 65-80 μm .

The silicon standard used is NIST SRM 640b silicon.¹⁰ As-received SP-1 graphite is used for the peak broadening correction. SP-1 is a flaky material processed from purified nature graphite flake by Union Carbide Corporation, with a mean diameter less than 75 μm .

2.2.2 X-Ray Diffraction

A 5-10 wt% Si standard was added to the SP-1 and samples as an internal standard. The graphite and silicon powder were ground and classified using a 200 mesh nylon sieve. The 1mm thick sample was loaded on a glass side-drift holder. X-ray powder diffraction data were collected using a Siemens/Bruker D500 diffractometer equipped with a 1° divergence slit, a 0.05° receiving slit, a graphite monochromator, and a scintillation detector. The $\text{Cu } K_\alpha$ X-ray source ($\text{Cu } K_\alpha, \lambda=1.54056\text{\AA}$) was used at 40 kV and 30 mA. Diffraction patterns were collected as a step scan from 10 - 90° 2θ , with a step size of 0.02° 2θ and a dwell time of 5 sec/step at room temperature.

2.2.3 Data Analysis

The original patterns were analyzed using Jade 7 software (Materials Data Inc, 2004). Profile fitting using Pearson-VII function was applied to find the peak value and the full-

width half-maximum (FWHM), for both carbon and silicon peaks. The credibility of profile fitting can be examined with the residual error, R%, defined as:

$$R\% = \sqrt{\frac{\sum(I_{obs} - I_{calc})^2 / I_{obs}}{\sum I_{obs}}} \times 100 \quad (2.1)$$

where, I_{obs} is the observed intensity, I_{calc} is the calculated intensity, and the summation is undertaken over all data points in the refined region. The value of R% should be as low as possible, desirably below 10%. The peak identifications for the Silicon SRM 640b and SP-1 are given in Table 2.1.

Table 2.1.
Exact Peak Positions for Si SMR 640b and Graphite SP-1 Peaks ($\lambda=1.54056\text{\AA}$, T = 298K)

Silicon SMR 640b ¹⁰		Graphite SP-1 ⁶	
<u>hkl</u>	<u>2θ</u>	<u>hkl</u>	<u>2θ</u>
111	28.442°	002	26.71°
220	47.303°	100	42.64°
311	56.122°	101	44.85°
400	69.130°	004	55.03°
331	76.376°	110	78.05°

The interplanar spacings of d_{002} , d_{004} and d_{110} were calculated using Bragg's law. The lattice parameters were determined by the cell refinement program of Jade7 using a least-square analysis. This program is used to calculate the powder pattern on the basis of a structural model as well as the characteristics of the instrument used, and minimize the differences between the intensities observed and the intensities calculated. The results of a cell refinement can be gauged by the value of Smith/Synder figure-of-merit, F(N), which indicates the completeness and accuracy of measured interplanar spacings.⁸ The figure-of-merit is defined as:

$$F(N) = \frac{1}{|\overline{\Delta 2\theta}|} \cdot \frac{N}{N_{poss}} \quad (2.2)$$

where N is the number of refined peaks, N_{poss} is the number of reflections in the refined region, and $|\overline{\Delta 2\theta}|$ is the average absolute $\Delta 2\theta$ error. Figure-of-merits more than 50 are considered high quality.¹¹

Crystallite sizes L_c and L_a were calculated using the Scherrer equation:¹²

$$L = k\lambda / \beta \cos \theta \quad (2.3)$$

where k is the Scherrer constant taken as 0.9, and β is the corrected FWHM value in radians.¹³ The corrected FWHM value is the true FWHM without instrumental broadening. SP-1 is used as the standard to obtain the systematic line broadening. The corrected FWHM value, β , is determined by the following:

$$\beta = \sqrt{\beta_{obs}^2 - \beta_{std}^2} \quad (2.4)$$

where β_{obs} is the observed FWHM value in radians, and β_{std} is the value of SP-1 in radians. The 002 reflection is used to obtain an average crystallite height, L_c , and 110 is used to obtain an average crystallite width, L_a .

2.3 Results and discussion

2.3.1 Crystal Structure of Unirradiated Nuclear Graphites

The powder diffraction patterns of SP-1 and nuclear graphite samples along with the silicon standard are given in Figure 2.1. The lattice parameters and crystallite sizes are given in Table 2.2. For graphite SP-1, the measured interlayer d-spacing and calculated lattice parameters are $d_{002}=3.3547 \text{ \AA}$, $a=2.4617(6) \text{ \AA}$ and $c=6.7076(15) \text{ \AA}$, in good agreement with Howe's calculation.⁶

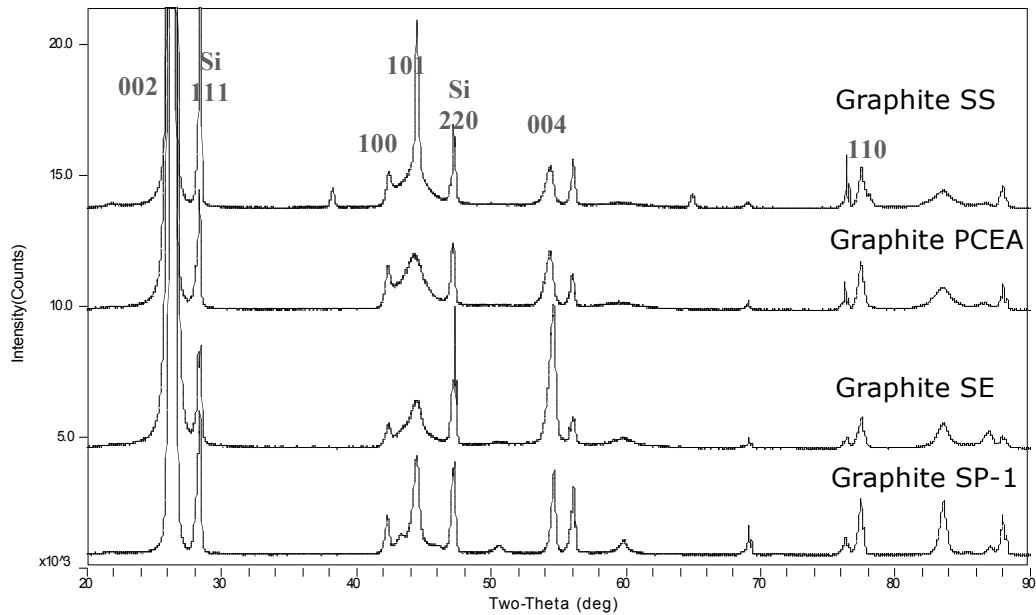


Figure 2.1. X-ray powder diffraction patterns of SP-1 and unirradiated nuclear graphite samples along with the silicon standard. Wavelength $\lambda = 1.54056 \text{ \AA}$.

Table 2.2
Lattice Parameter and Crystallite Size Results for SP-1 and Irradiated Nuclear Graphites

Sample	Graphite SP-1	Graphite SE	Graphite PCEA	Graphite SS
Quality	Anisotropic	Anisotropic	Semi-isotropic	Isotropic
Volumetric CTE $\times 10^6$ (K ⁻¹)	~0	0.09	3.5	4.4
d_{002} (Å)	3.3547(25)	3.3533(25)	3.3732(25)	3.3745(25)
d_{004} (Å)	1.6771(6)	1.6783(6)	1.6837(6)	1.6840(6)
d_{110} (Å)	1.2308(3)	1.2306(3)	1.2309(3)	1.2308(3)
Cell Refinement	a (Å)	2.4617(6)	2.4611(6)	2.4626(7)
	c (Å)	6.7076(15)	6.7119(19)	6.7331(23)
F(N)	F(9)=55.7	F(6)=57.7	F(6)=42.1	F(6)=35.9
$L_c(002)$ (Å)	>1000 ^a	360±20	300±20	350±20
$L_a(110)$ (Å)	>1000 ^a	300±20	400±30	300±30

^a From Reference 5. Broadening of peaks is due to systematic line broadening.

The d-spacing results of unirradiated nuclear graphite correlate with the thermal expansion data. The specimens having a larger interlayer spacing (d_{002} and d_{004}) also exhibit larger coefficients of thermal expansion. The spacing on the basal sheet (d_{110}) changes very little. The d_{002} decreases as the degree of crystallinity increases. For this reason, these data support the fact that the Graphite SS is indeed an isotropic sample having low crystallinity. The highest CTE value (4.4×10^{-6} K⁻¹) exists for this isotropic Graphite SS and is the result of a randomly oriented crystallite structure throughout the volume of the sample. These CTE values are volumetric expansion data, so on average the randomization in structure results in higher expansion values. It has been found that the isotropic or semi-isotropic quality of the specimens ensures dimension stability for a nuclear reactor; the higher the coefficient of thermal expansion, the lower the

dimensional change rate.¹⁴ Therefore, in order to select a graphite for a nuclear graphite application, one must consider the crystal structure as well as the thermal expansion behavior. This is a balance between dimensional stability and chemical stability associated with a well-organized crystal. Among these three samples, Graphite SS and Graphite PCEA would appear to be reasonable carbons for nuclear application.

Unit cell dimensions for each sample are calculated using a least-squares analysis. The Smith/Snyder figure-of-merits are in the range of 35-60, which decrease with the crystallinity. Crystallite size results for the L_c (002) and L_a (110) of all the samples are in the range of 300-400 Å. These crystallites do not vary much in size between each other. And for this reason, the crystallite size itself is not a parameter for materials selection.

2.3.2 X-Ray Diffraction Approach on Carbon

There are four points we wish to make regarding the use of X-ray powder diffraction to evaluate the carbon materials used in our lab. First, using a thin sample enables the reduction of the peak shift and asymmetric broadening caused by sample transparency, however, at the expense of the intensity and peak-to-background ratio. When a sample is not well crystallized, the low intensity and peak-to-background ratio will introduce big error in determining the crystallite sizes. The powder sample of ~1mm thick yields a statistically reasonable value of FWHM in order to calculate the crystallite size.

Second, graphite SP-1 is applied to correct the systematic line broadening associated with carbon materials. The Si SRM 640b standard gives significantly broadened peaks, which

is not suggested to correct instrumental line broadening.¹⁵ Since SP-1 documents to be a highly ordered graphite crystal, using SP-1 simplifies the correction for instrument-sensitive factors affecting the diffraction in line intensity, as well as minimizing the effects caused by carbon structure-sensitive factors such as transparency effects.

Third, further improvements in the data analysis can be achieved using least-squares analysis to calculate the lattice constants a and c . This method is based on the space group $P6_3/mmc$ and the experimentally determined 2θ values. The statistical approach to examine the lattice constants leads to more reliable results than using only one peak to convert to lattice constant a and c , such as $a=2d_{110}$, and $c=2d_{002}$ or $c=4d_{004}$. The figure-of-merit values given in Table 2.2 are the result of using at least 6 peaks to calculate the lattice constant.

Finally, the experimental accuracy used in reporting these data must be noted. The deviation of d_{002} is calculated by differentiating Bragg's law:

$$\Delta d_{002} = \frac{\lambda}{2} \cdot \frac{\cos \theta}{\sin^2 \theta} \cdot \Delta \theta \quad (2.5)$$

For example, taking the value of θ_{002} as approximately $26.50/2 \cong 13.25^\circ$ and using a step size of 0.02° 2θ , the accuracy of the θ_{002} can be no better than 0.01° . This is 0.00017 radians. The accuracy therefore in reporting d_{002} can be no better than 0.0025 Å. Similarly, the accuracies in reporting d_{004} and d_{110} are 0.0006 Å and 0.0003 Å, respectively.

We also calculate the accuracy of L_c and L_a by differentiating the Scherrer equation:

$$\Delta L = 0.9\lambda \times \left(\frac{\Delta\beta}{\beta^2 \cos \theta} + \frac{\sin \theta \cdot \Delta\theta}{\beta \cos^2 \theta} \right) \quad (2.6)$$

where β is the corrected FWHM value in radians, $\Delta\beta$ is FWHM error in radians and $\Delta\theta=0.00017$ in radians as previously described. On this basis the accuracy in both L_c (002) and L_a (110) can be no better than 20 Å. It is important to recognize that these values represent unique dimensions through the crystallite, the body diagonal and the true crystallite width, respectively. It is therefore clear that one must be careful to report both the crystallite sizes and their accuracy.

2.4 Conclusion

The lattice d-spacings and crystallite sizes of three unirradiated nuclear graphite samples are measured using x-ray powder diffraction. Silicon standard and SP-1 are used to correct the peak position and systematic line broadening. The results indicate that an increase in the coefficient of thermal expansion (CTE) is associated with an expansion in the interlayer spacing, d_{002} . For graphite used in nuclear reactors, an optimization between crystallinity and CTE must be made.

References

1. B.J. Marsden, "Nuclear Graphite for High Temperature Reactors," pp. 174-89 in *IAEA Technical Committee Meeting on "Gas Turbine Power Conversion Systems for Modular HTGRs"*. International Atomic Energy Agency, Vienna, 2000. Also available at http://www.iaea.org/inis/aws/htgr/fulltext/gtpcs_13.pdf
2. W. Ruland, "X-Ray Studies on the Structure of Graphitic Carbons," *Acta Crystallogr.*, **18** [6] 992-96 (1965).
3. R.E. Franklin, "The Structure of Graphitic Carbons," *Acta Crystallogr.*, **4** [3] 253-61 (1951).
4. A. Oberlin, "High-Resolution TEM Studies of Carbonization and Graphitization," pp. 1-143 in *Chemistry and Physics of Carbon*, Vol. 22. Edited by P. A. Thrower. Dekker, New York, 1989.
5. P.L. Walker, L. Austin, and J. Tietjen, "Oxygen Chemisorption Effects on Graphite Thermoelectric Power," pp. 327-65 in *Chemistry and Physics of Carbon*, Vol. 1. Edited by P. L. Walker. Dekker, New York, 1966.
6. J.Y. Howe, C.J. Rawn, L.E. Jones, and H. Ow, "Improved Crystallographic Data for Graphite," *Powder Diffr.*, **18** [2] 150-54 (2002).
7. W.N. Reynolds, *Physical Properties of Graphite*; p. 33. Elsevier, Amsterdam, 1968.
8. G.S. Smith and R.L. Snyder, " F_N : A Criterion for Rating Powder Diffraction Patterns and Evaluating the Reliability of Powder-Pattern Indexing," *J. Appl. Crystallogr.*, **12** 60-65 (1979).
9. N. Iwashita, C.R. Park, H. Fujimoto, M. Shiraishi, and M. Inagaki, "Specification for a Standard Procedure of X-Ray Diffraction Measurements on Carbon Materials," *Carbon*, **42** [4] 701-14 (2004).
10. L. Kieffer, R. McKenzie, C.R. Hubbard, C. Robbins, and W. Wong-Ng, "National Bureau of Standards Certificate: Standard Reference Material 640b," National Bureau of Standards, Gaithersburg, MD, 1987.
11. R. Jenkins and R. Snyder, *Introduction to X-Ray Powder Diffraction*; pp. 310-17. Wiley, New York, 1996.
12. P. Scherrer, "Estimation of the Size and Internal Structure of Colloidal Particles by Means of Röntgen Rays," *Nachr. Ges. Wiss. Göttingen, Math.-Phys. Kl.*, **2** [1] 98-100 (1918). As cited in R. Jenkins and R. Snyder, *Introduction to X-Ray Powder Diffraction*; p.90. Wiley, New York, 1996.

13. P.A. Thrower, D.C. Nagle, and W.S. Horton, "The Anisotropy of Pyrolytic Graphite," *J. Appl. Crystallogr.*, **6** [5] 347-51 (1973).
14. J.H. Simmons, *Radiation Damage in Graphite*; pp. 136-62. Pergamon, Oxford, 1965.
15. L.B. McCusker, R.B. Von Dreele, D.E. Cox, D. Louër, and P. Scardi, "Rietveld Refinement Guidelines," *J. Appl. Crystallogr.*, **32** [1] 36-50 (1999).

3 Computer Simulation:

Influence of Boron on Carbon Nanotube Structure

3.1 Introduction

Carbon materials have numerous potential applications because of their lightweight, mechanical and electrical performance. However, many potential applications are not realized due to poor oxidation resistance. It is well established that the substitution of boron in graphite inhibits oxidation as well as enhances mechanical and electronic behavior.^{1,4} This observation has been made for a wide array of carbon materials that include bulk graphites, carbon fibers and C-C composites. Yet, the concentration of boron as a solid solution impurity is understood to be capped at 2.3 at.%.⁵ Therefore, there is a limit to the extent to which properties can be modified. There is a great interest in increasing the substitutional boron concentrations in graphite solids to further enhance the oxidation resistance and modify the electrical behavior of these materials. In the mid-1980s, at the University of California-Berkeley, a boron rich carbon solid was synthesized via a chemical vapor deposition (CVD) reaction using C_6H_6 and BCl_3 at $800^\circ C$.⁶ This boron-rich carbon material, BC_x , is argued to have 25 at.% substitutional boron. The CVD process to synthesize boron-rich carbon solids continues to be widely studied.⁷⁻¹⁰ The reported stoichiometries of these boron-rich carbons vary between C_3B and C_6B (15 – 25 at. %B) as a function of the fabrication routes employed. For the purposes of this paper we refer to this material as C_xB where X is understood to vary between 3 and 6. The concentrations of boron in these novel carbons and the influence of large boron concentrations on structure and resulting properties continue to be of

interest because of the potential for synthesizing nanoscaled carbons with tunable electronic properties and oxidation resistance. Of particular interest in this work is the influence of large concentrations of boron on the nanotube structure in the form of bond strain and angular distortions as well as tube morphology.

3.2 Background

Due to the deficient electron octet of boron in sp^2 hybridized carbon, boron exists as a p-type substitutional impurity. Soule's work establishes that the presence of substitutional boron at relatively low concentrations (~ 1 ppm to 0.5 at.%) significantly modifies the electronic structure of graphite.¹¹ At a concentration of 0.2 at.% boron, the Fermi level is suppressed to 0.14 eV which is well into the valence band. Delhaes and Marchand's results on the electronic properties of boron-doped polycrystalline graphite are consistent with Soule's.¹² Preil *et al.* using reflectivity measurements determined that the Fermi level shifts downward 0.2 eV at 0.5 at.% boron loading.¹³ These findings support the fact that the electronic properties, such as diamagnetic susceptibility, Hall coefficient, and conduction may all be modified via the presence of substitutional boron. The ability to modify electronic behavior due to the presence of boron at concentrations as low as the ppm range and as high as 25 at.% boron is particularly attractive. Additionally, it is recognized that the modification of electronic behavior in graphite solids does suppress oxidation.

The presence of substitutional boron modifies the crystal structure. Boron is considered a catalyst of the graphitization process.¹⁴ Using X-ray measurements, Lowell showed

that an increasing boron concentration yields a larger a lattice parameter and a smaller c lattice parameter.⁵ Recently, Hishiyama and Inagaki identified the changes in a and c via a set of linear relationships:¹⁵

$$a \text{ (nm)} = 0.2461 + 0.03 X_B$$

$$c \text{ (nm)} = 0.6708 - 0.17 X_B,$$

where the atomic fraction of boron $X_B \leq 0.0235$. The increase in the lattice parameter a contributes to a longer C-B bond length over that of C-C. The contraction of the c -axis is the result of a Poisson contraction associated with the lengthening of the a -axis balanced against the decrease in the π electron density brought on by the increased substitutional boron concentration.¹⁶ Work is needed to address the decreasing van der Waals forces and the coupled modification of the elastic compliance of the graphite structure. Yet, we do know that there is a direct relationship between the lattice structure and the boron concentration. What remains to be understood is how structure changes as a result of the presence of boron play out on the nanoscale.

Boron rich carbon nanotubes will have crystal and electronic structure that are different from bulk doped-graphite due to the quantum confinement and curvature of the cylinders. There are two methods to achieve boron-doped carbon nanotubes, substitution reactions or direct synthesis. The substitution reactions undertaken to date involve either solid-state diffusion, using either single-walled or multi-walled carbon nanotube host materials and boron-containing compounds, such as B_2O_3 as the source of the dopant impurity. The boron concentrations achieved are reported to be ~ 10 at.% by Golberg *et al.*¹⁷ and 10-15 at.% by Borowiak-Palen *et al.*,^{18,19} respectively. These boron concentrations are

much larger than that of the boron-doped graphite via solid-state diffusion and close to the boron concentration levels reported in the BC_x thin films of Hach *et al.*¹⁰ The direct synthesis methods include arc-discharge/laser ablation via changing the chemical composition of starting electrodes or targets, and chemical vapor deposition. Boron-doped single wall carbon nanotubes (SWCNT) and multi-wall carbon nanotubes (MWCNTs) have been produced via direct synthesis routes. Redlich *et al.*²⁰ measured the boron content as 1-5 at.% using arc-discharge synthesis and Satishkumar *et al.*²¹ obtained boron-doped carbon nanotubes having 2.78 at.% boron via the pyrolysis of acetylene-diborane mixtures in which the boron content did not vary with tube depth.

Boron doping is found to improve graphitization of MWCNTs.²⁰ These tubes have an interlayer spacing, d_{002} , of 0.3352(2) nm. The interlayer spacing of undoped tubes is 0.3422(2) nm. In addition, boron enhances the longitudinal growth of nanotubes by increasing length by as much as more than 10 times as well as increasing tube diameter. Golberg *et al.* investigated boron doping SWCNTs via substitution reaction, and frequently observed that the diameters of the isolated SWCNTs increased to ~2.1-3.2 nm, as compared to that of the uniform starting carbon SWCNT diameter of ~1.4nm.¹⁷ These authors noted that the reactions leading to boron inclusion in the tubes introduces defects, curling and breaking of the tube shell. Two or more open shells often coalesce to form a new shell of larger diameter eliminating the dangling bonds created during the synthesis.

In our experimental investigations, we use a catalytic CVD method reacting benzene and BCl_3 to produce boron-doped carbon nanotubes containing boron concentrations between

10-15 at%. The high boron content creates an increase in the point defect density. We have noted that our synthesized boron-doped nanotubes and filaments have tube diameters that are larger than the undoped carbons. In this paper, we present the molecular mechanics and quantum mechanics computer modeling that is used to explore the influence of large substitutional boron concentrations on nanotube structure at the atomic, crystal and nano-structural level. Additionally, we offer some experimental evidence of the impact of boron on carbon nanotubes and filaments.

3.3 Experimental

3.3.1 Computer Modeling of Structure

Modeling of the structure is undertaken using Cerius software and an SGI Octane workstation. Both molecular mechanics and quantum mechanics methods are applied. The molecular mechanical simulation is carried out using the Minimizer module of Cerius²® (a modeling and simulation environment developed by Accelrys, San Diego, CA) based on the Universal Force Field (UFF).²² The quantum mechanical simulation is carried out using the CASTEP module of Cerius²®. CASTEP®, an acronym for Cambridge Serial Total Energy Package, is a commercial software package of the *ab initio* calculation for the electronic ground state energy.²³ Both Minimizer and CASTEP module calculate the optimized geometry and ground state energy of the structure. Minimizer calculations are used for big molecule and lattice having more than 50 atoms. CASTEP is used on periodically repeated cells or boxes having less than 50 atoms.

3.3.2 Synthesis of Boron-Doped Carbon Nanotubes

A CVD reaction furnace is used for the synthesis. The reaction furnace includes a Thermolyne 21100 tube furnace, Aera Inc. D980C Mass Flow Controller, Matheson Inc. FM-1050 flowmeters, a standard roughing pump, a mineral oil hydrocarbon trap and a sodium hydroxide trap. The reactant gases are MG Industries, CP grade 99.9% pure BCl_3 and Alfa Aesar, spectrophotometric grade 99.5+% C_6H_6 . The carrier gas used is Mills Welding & Specialty Gases UHP H_2 .

The total volumetric flow rate of gas entering the reactor is 65 ml/min. The absolute system pressure is 93.5 kPa. Benzene at 10 ml/min is introduced via the H_2 carrier gas. BCl_3 of 10 ml/min is mixed with the benzene prior to introduction. A nickel coated (~5 nm thick) fused silica slide is used as the substrate. The reaction is undertaken at 800 °C for 30 minutes. After deposition, samples are annealed at 900 °C for 20 hours under 93.5 kPa UHP He.

3.3.3 Transmission Electron Microscopy

Transmission electron microscopy is performed with a JEOL 2000-FX Electron Microscope. The accelerating potential is 200 kV, and no coating is used.

3.4 Results and Discussion

3.4.1 Modeling of Boron-Doped Carbon Lattice

The boron-doped carbon (or C_xB) structure is graphite-like, having weak interaction between the layer planes.⁸ We modeled the single C_xB planes as finite clusters having edge sites saturated with hydrogen. For this reason, circumcoronene ($C_{54}H_{18}$) is chosen as the host molecule. The carbon atoms are sp^2 hybridized within the lattice. The influence of boron on the structure is investigated using molecular mechanics by substituting boron for carbon symmetrically and asymmetrically within the host molecule. Figure 3.1 is a circumcoronene host molecule and a host molecule containing 11 at.% boron (Molecule I) at selected lattice sites. Presented in Figure 3.1 are the in-plane (a -dimension) and the out of plane on-edge view of the distortion on the z -axis (c -dimension). Carbon and boron covalent radii are 0.732 and 0.828 Å, respectively. A distortion in the structure by substituting boron for carbon is expected. The bonding length of C-C within the innermost ring (highlighted in blue) changes from 1.410 Å in the host molecule to 1.394 Å in the 11% boron-doped molecule. Boron symmetrically positioned imposes a large compressive strain on this innermost ring. Additionally, the molecule experiences an angular distortion that produces an out-of-plane buckling, having a deflection of $\delta = 0.7$ Å. In the case of Molecule I, boron atoms are intentionally positioned next to the innermost ring, and a maximum out-of-plan deflection is obtained. When boron atoms are moved out, the deflection obtained is less. When boron is symmetrically substituted between 2% to 20%, the observed distortion maximum is also $\delta = 0.7$ Å.

The images of other two molecules containing 11% boron asymmetrically distributed are given in Figure 3.2. Asymmetrical distribution of boron at these concentration levels produces no distortion of the plane; no buckling ($\delta = 0$) takes place within these structures. The on-edge view (z-axis) is as flat as the host lattice. Table 3.1 lists the ground state total energy and linear strains on x and y dimensions of the three molecules containing 11 at.% boron substituted.

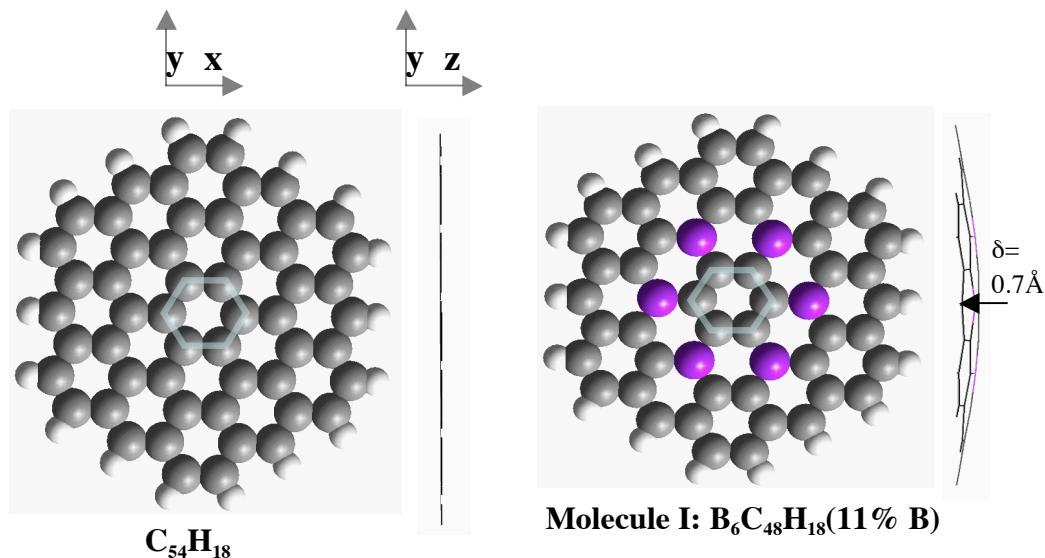


Figure 3.1. The influence of 11% boron symmetrically distributed with a circumcoronene ($C_{54}H_{18}$) host molecule on the out-of-plane distortion, δ . Molecule I is the structure having 11% boron symmetrically distributed and boron loading is clustered. A distortion maximum of 0.7\AA occurs on Molecule I.

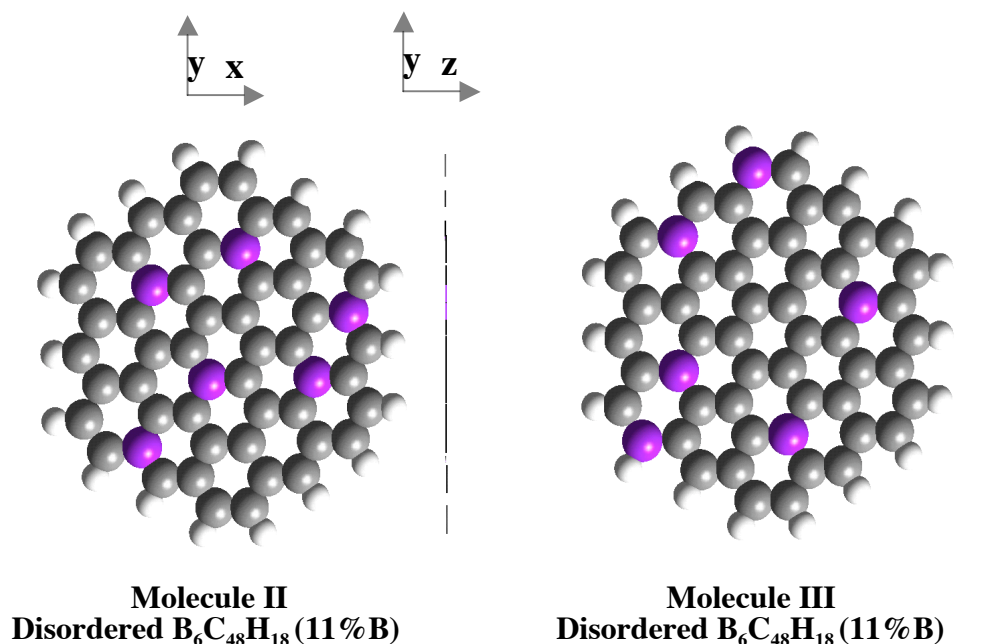


Figure 3.2. The influence of 11% boron asymmetrically distributed within a circumcoronene (C₅₄H₁₈) host molecule. Molecule II and III are two structures having 11% boron asymmetrically distributed. No in-plane strain is noted.

Table 3.1

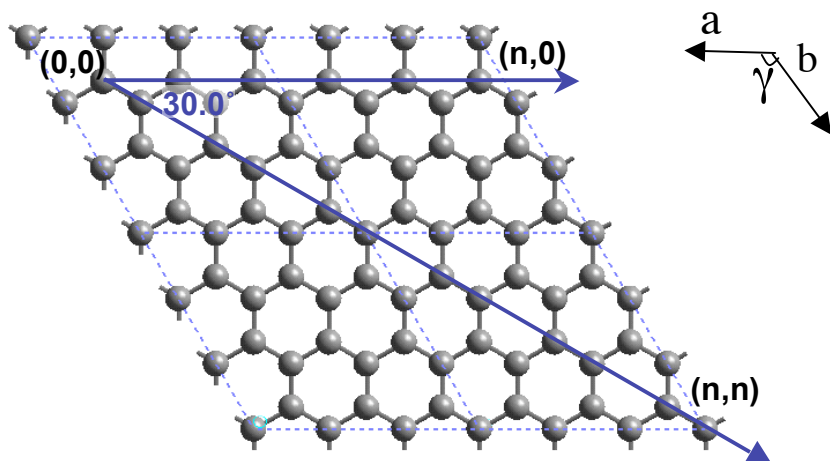
Total Energy and Linear Strains Associated With a Circumcorene Host Molecule Containing 11 at.% Boron

	Total Energy (kJ/mol)	Strain on x axis, ϵ_x	Strain on y axis, ϵ_y
Molecule I	631.8	4%	7.0%
Molecule II	754.9	4%	2.2%
Molecule III	751.1	3%	3.4%

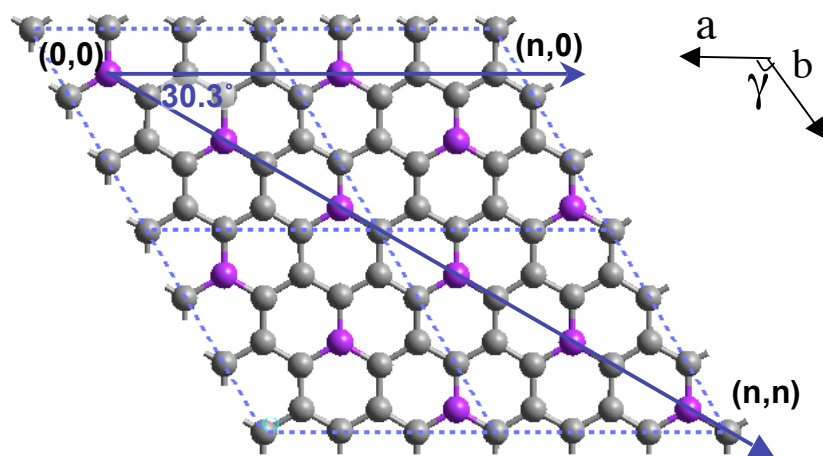
Molecule I has the lowest total energy and highest strains both on x and y dimensions, while molecule II and III have the similar energy level and strains of 2-4%. An important issue associated with the ground state energy of boron substitution within the carbon structure is the location of boron in the lattice. Hach et al.¹⁰ undertook a similar calculation and found that boron distribution in the layer plane as short range clusters is a

favorable (low energy) positioning. The structure of Molecule I satisfies the arrangement of this low energy structure, which is arguably the most stable among these three molecules. These calculations support the notion that it is less energy intensive to fabricate tubes or novel carbons with clusters of boron symmetrically distributed. The net result is that these structures will contain a significant amount of strain introduced by the boron atom and as a result the tube structure will be distorted.

To investigate the influence of boron on nanotube structure, a 2D lattice is constructed representing a C_5B stoichiometry. Figure 3.3 is a schematic of an undoped graphite layer plane and C_5B (17 at.%) layer plane. Both the orientation of the zig-zag (n,0) edge and arm-chair (n,n) edge are noted in the schematic. A unit cell of 18 carbon atoms is used to facilitate the construction of C_5B lattice in CASTEP. The calculated lattice parameters of the undoped graphite layer plane are $a = b = 7.38 \text{ \AA}$, and $\gamma = 120^\circ$. The C_5B lattice is constructed by uniformly (symmetrically) substituting boron atoms along the diagonal of the unit cell. The calculated lattice parameters of this unit cell are $a = 7.50 \text{ \AA}$, $b = 7.51 \text{ \AA}$, and $\gamma = 119.5^\circ$. With the substitution of 17% boron into the graphite layer, the bond lengths are increased and bond angle is decreased. The area of the unit cell is expanded by 4% and the angle decreased by 0.5° . With the addition of boron, the angle between the nanotube vector (n,0) and (n,n) is distorted by 0.3° . This distortion or tube strain will introduce chirality or modify the existing chirality of the nanotube.



(a) Unit Cells of graphite layer



(b) Unit Cells of C_5B layer

Figure 3.3. Influence of boron concentration on the distortion of the 17% boron-doped graphite layer plane. (a) An undoped graphite layer plane, having a 2D lattice of 18 carbon atoms. The calculated lattice parameters are $a=b=7.38 \text{ \AA}$ and $\gamma = 120^\circ$. (b) An 17% boron-doped graphite layer plane, having a 2D C_5B lattice. The lattice parameters are $a = 7.50 \text{ \AA}$, $b = 7.51 \text{ \AA}$ and $\gamma = 119.5^\circ$, and the chiral vector is $(n,0)$.

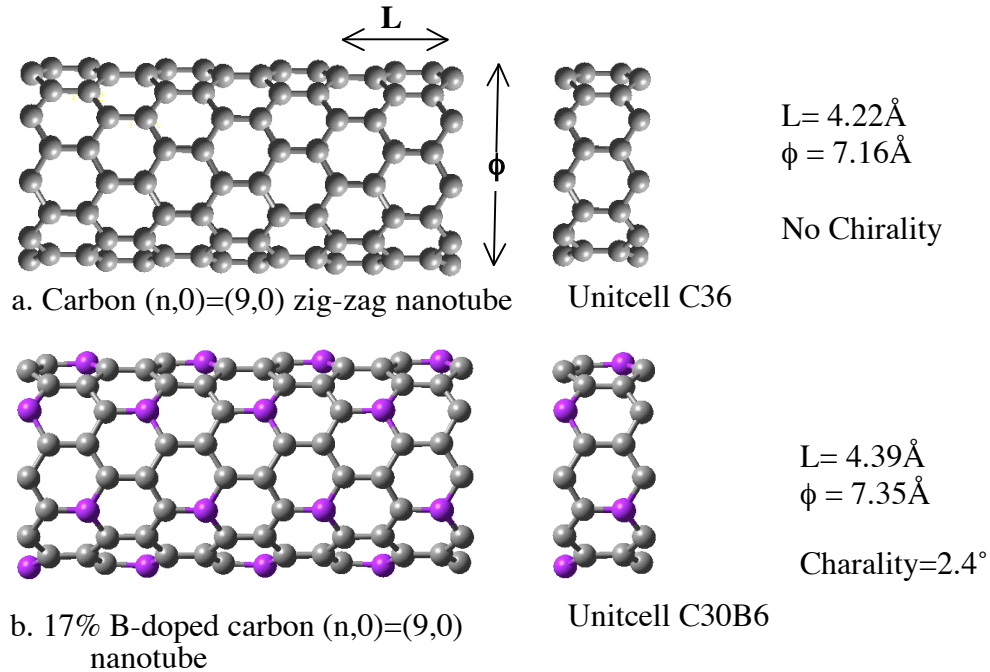


Figure 3.4. 17% boron symmetrically distributed modifies the dimensions of a (9,0) nanotube. Chirality of 2.4° is present. (a) A carbon (9,0) zig-zag nanotube, and (b) 17% boron symmetrically doped carbon (9,0) nanotubes.

Using the 2D lattice given in Figure 3.3 a SWCNT is constructed in Figure 3.4 using CASTEP. The introduction of boron into a zig-zag (9,0) nanotube increases the tube length (L) from 4.22 Å to 4.39 Å, and the tube diameter (ϕ) from 7.16 Å to 7.35 Å. There is 4% strain along the length and 3% strain around the diameter of the unit cell with the substitution of 17% boron positioned symmetrically throughout the tube. As a result of the twisted 2D lattice, a chirality of 2.4° is present in this C₅B (9,0) nanotube.

3.4.2 Boron-doped Carbon Nanotubes via CVD Process

A transmission electron micrograph of boron-doped carbon filaments deposited at 800°C for 30min is given in Figure 3.5. These filaments have a diameter of ~80 nm. Recent

XPS work indicates that the boron concentration is 11 at.%. There are two distinct microstructures along the tube axis. The first is a herringbone stacked core oriented 10-20° along the tube axis. The second is a helical outer diameter that has a 30° orientation along the tube axis. A spot diffraction pattern of this filament indicates the broad diffraction consistent with (002) of graphite ($d = 0.34$ nm). However, there are two sets of (002) scattering about the axis of the tube that is indicative of a helical patterning of the sp^2 carbon structure. At this point, it is clear that boron substitution in the filaments creates strains within the host structure. This strain may result in the modification of microstructure observed within the filaments deposited to date.

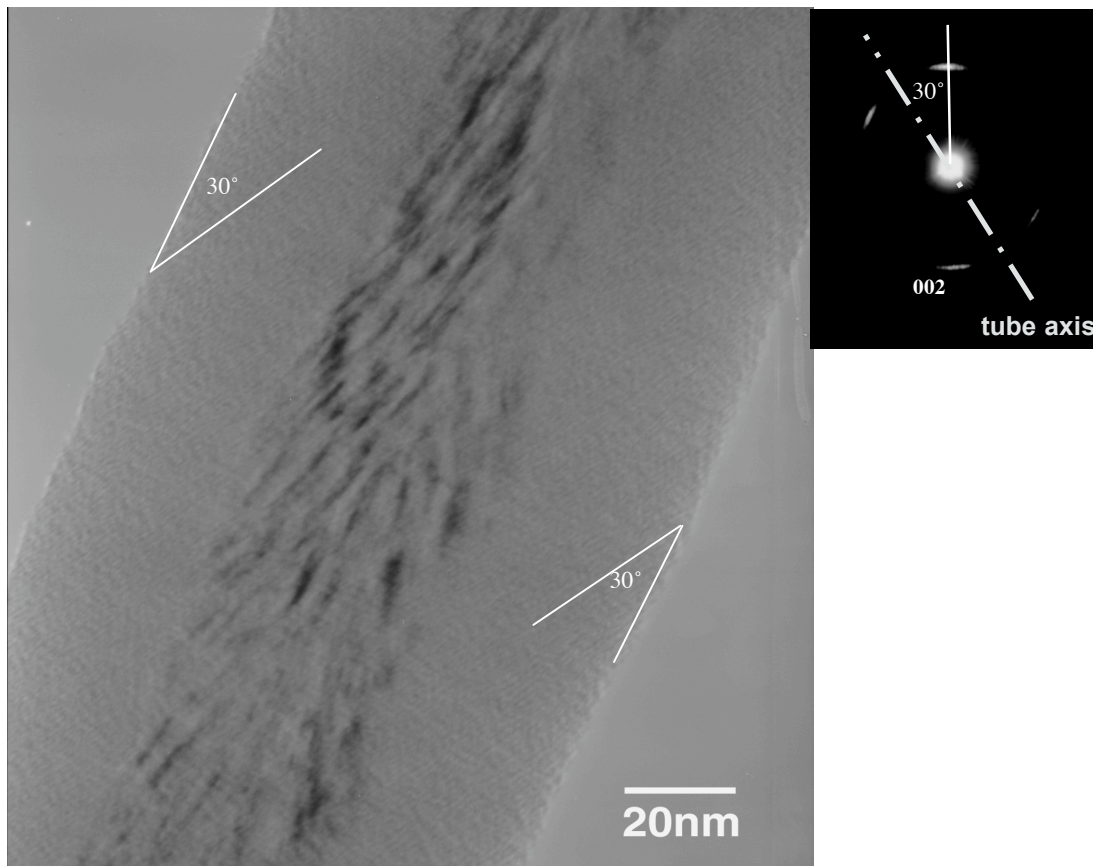


Figure 3.5. Bright-field TEM image and the electron diffraction pattern of a boron-doped filament deposited at 800°C for 30min.

3.5 Conclusions

The influence of substitutional boron on carbon nano-structures is investigated using molecular and quantum mechanics computer modeling. A circumcoronene ($C_{54}H_{18}$) molecule, 2D graphite layer and (9,0) carbon nanotubes are chosen as the host carbon lattices for this investigation. With the substitution of 2-20 at.% boron into the circumcoronene molecule, an angular distortion is created that produces an out-of-plane buckling, having a maximum deflection of $\delta = 0.7 \text{ \AA}$ at 11 at.% boron. With the substitution of 17% boron into the graphite layer, the dimensions and angle of the unit cell are both modified: the area of the unit cell is expanded by 4% and the angle is twisted by 0.5° . There is 4% strain on length and 3% strain on diameter of (9,0) nanotubes with the substitution of 17% boron symmetrically distributed. As a result of the twisted 2D lattice, a chirality of 2.4° is present in the C_5B (9,0) nanotube. Irregular buckling happens on the wall of randomly boron-doped nanotubes. According to the ground state energy calculation, it is expected that B-doped nanotubes grown in the vapor phase are likely to have random boron distribution. Additionally, B-doped carbon filaments have been catalytically synthesized via a CVD reaction using benzene and BCl_3 . With the addition of approximate 11% boron, the microstructure of the CVD nano-fiber exhibits two distinct carbon phases. There is also a reproducible angularity to these microstructures along the axis of the fiber that is argued to be the result of the distortions created on the crystal structure level.

References

1. D.J. Allardice and J.P.L. Walker, "The Effect of Substitutional Boron on the Kinetics of the Carbon-Oxygen Reaction," *Carbon*, **8** [3] 375-85 (1970).
2. L.E. Jones and P.A. Thrower, "Influence of Boron on Carbon Fiber Microstructure, Physical Properties, and Oxidation Behavior," *Carbon*, **29** [2] 251-69 (1991).
3. R.E. Taylor and D.E. Kline, "Dynamic Mechanical Behavior of Stress-Graphitized and Boron-Doped Pyrolytic Carbon," *Carbon*, **6** [6] 749-64 (1968).
4. A. Marchand and E. Dupart, "Proprietes Electroniques D'un Pyrocarbone Dope Avec Du Bore: Evolution En Fonction Du Taux De Bore," *Carbon*, **5** [5] 453-69 (1967).
5. C.E. Lowell, "Solid Solution of Boron in Graphite," *J. Am. Ceram. Soc.*, **50** [3] 142-44 (1967).
6. J. Kouvetakis, R.B. Kaner, M.L. Sattler, and N. Bartlett, "A Novel Graphite-Like Material of Composition BC_3 , and Nitrogen-Carbon Graphites," *J. Chem. Soc., Chem. Commun.*, **1986** 1578-79 (1986).
7. B.M. Way, J.R. Dahn, T. Tiedje, K. Myrtle, and M. Kasrai, "Preparation and Characterization of B_xC_{1-x} Thin Films with the Graphite Structure," *Phys. Rev. B: Condens. Matter Mater. Phys.*, **46** [3] 1697-702 (1992).
8. D.L. Fecko, L.E. Jones, and P.A. Thrower, "The Formation and Oxidation of BC_3 , a New Graphitelike Material," *Carbon*, **31** [4] 637-44 (1993).
9. W. Cermignani, T.E. Paulson, C. Onneby, and C.G. Pantano, "Synthesis and Characterization of Boron-Doped Carbons," *Carbon*, **33** [4] 367-74 (1995).
10. C.T. Hach, L. E. Jones, C. Crossland, and P.A. Thrower, "An Investigation of Vapor Deposited Boron Rich Carbon - A Novel Graphite-Like Material - Part I: The Structure of BC_x (C_6B) Thin Films," *Carbon*, **37** [2] 221-30 (1999).
11. D.E. Soule, "The Effect of Boron on the Electronic Properties of Graphite," pp. 12-21 in *The 5th Conference on Carbon*, Vol. 1. Pergamon Press, New York, 1962.
12. P. Delhaes and A. Marchand, "Proprietes Electroniques D'un Graphite Polycristallin Dope Au Bore," *Carbon*, **3** [2] 125-40 (1965).

13. M.E. Preil, R.C. Tatar, D.P. DiVincenzo, and J.E. Fischer, "Dielectric Function and Critical-Point Transitions in Boron-Doped Graphite," *Phys. Rev. B: Condens. Matter Mater. Phys.*, **26** [8] 4674-9 (1982).
14. S. Marinkovic, "Substitutional Solid Solubility in Carbon and Graphite," pp. 1-64 in *Chemistry and Physics of Carbon*, Vol. 19. Edited by P. A. Thrower. Dekker, New York, 1989.
15. Y. Hishiyama and M. Inagaki, "Lattice Parameter Changes in Graphite with Boron Doping," *Carbon*, **39** [1] 150-52 (2001).
16. J.A. Turnbull, M.S. Stagg, and W.T. Eeles, "Annealing Studies of Boron-Doped Graphite by Electron Microscopy and X-Ray Diffraction," *Carbon*, **3** [4] 387-88 (1966).
17. D. Golberg, Y. Bando, L. Bourgeois, K. Kurashima, and T. Sato, "Large-Scale Synthesis and HRTEM Analysis of Single-Walled B- and N-Doped Carbon Nanotube Bundles," *Carbon*, **38** [14] 2017-27 (2000).
18. E. Borowiak-Palen, T. Pichler, G.G. Fuentes, A. Graff, R.J. Kalenczuk, M. Knupfer, and J. Fink, "Efficient Production of B-Substituted Single-Wall Carbon Nanotubes," *Chem. Phys. Lett.*, **378** [5-6] 516-20 (2003).
19. E. Borowiak-Palen, T. Pichler, A. Graff, R.J. Kalenczuk, M. Knupfer, and J. Fink, "Synthesis and Electronic Properties of B-Doped Single Wall Carbon Nanotubes," *Carbon*, **42** [5-6] 1123-26 (2004).
20. P. Redlich, J. Loeffler, P.M. Ajayan, J. Bill, F. Aldinger, and M. Ruhle, "B-C-N Nanotubes and Boron Doping of Carbon Nanotubes," *Chem. Phys. Lett.*, **260** [3-4] 465-70 (1996).
21. B.C. Satishkumar, A. Govindaraj, K.R. Harikumar, J.-P. Zhang, A.K. Cheetham, and C.N.R. Rao, "Boron-Carbon Nanotubes from the Pyrolysis of C₂H₂-B₂H₆ Mixtures," *Chem. Phys. Lett.*, **300** [3] 473-77 (1999).
22. A.K. Rappé, C.J. Casewit, K.S. Colwell, W.A. Goddard, and W.M. Skiff, "UFF, a Full Periodic Table Force Field for Molecular Mechanics and Molecular Dynamics Simulations," *J. Am. Chem. Soc.*, **114** 10024-35 (1992).
23. M.D. Segall, P. Lindan, M.J. Probert, C.J. Pickard, P.J. Hasnip, S.J. Clark, and M.D. Payne, "First-Principles Simulation: Ideas, Illustrations and the CASTEP Code," *J. Phys.: Condens. Matter*, **14** [11] 2717-44 (2002).

4 Synthesis of Boron-doped Carbon Nanotubes and Nanofibers

4.1 Introduction

Carbon filaments, including nanotubes and nanofibers, have been synthesized by catalytic chemical vapor deposition (CVD) since the 1960s.¹⁻⁴ Carbon nanotubes have been a focus in materials research since they were first discovered in 1991.⁵ This important discovery led to the realization that nanotubes would inherit several important properties associated with the organization of the graphene layers along the filament axis. For example, a nanotube exhibits high electrical conductivity, thermal conductivity, and mechanical strength along its axis. Nanotubes are also very inert as there are very few open edges and dangling bonds in the structure. These properties make carbon nanotubes an important material for various electronic and mechanical applications. The applications of carbon nanotubes and nanofibers are being investigated in many areas, such as field emission tips,⁶⁻¹⁰ transistors or logic elements,¹¹⁻¹³ electrodes in electrochemical supercapacitors,^{14,15} and potential filling materials in polymer composites.¹⁶⁻¹⁸

Since the late 1990s, substantial and rapid progress has been made in the development of CVD as a highly controlled technology for the production of carbon nanotubes and nanofibers. Today, using CVD methods, it is possible to fabricate high quality single-walled carbon nanotubes (SWCNTs),^{19,20} or multiwalled carbon nanotubes (MWCNTs),²¹ horizontally aligned tubes^{22,23} or vertically aligned tubes,²³⁻²⁵ tubes with controlled

diameter,^{8,26} tubes with controlled length,^{27,28} tubes with tubular stacking or platelet stacking,^{4,29} and tubes deposited directly onto substrates or tubes in bulk form.³⁰ Compared to the other methods of making nanotubes and nanofibers, the major advantages of CVD are: (1) the carbon nanotubes and nanofibers can be used directly without further purification,³¹ and (2) the production can be easily scaled up to an industrial level.

In our research, a catalytic CVD process is used to grow boron-doped carbon nanotubes and nanofibers. Generally speaking, catalyst nanoparticles, carbon and boron feedstocks, carrier gases, and heat are required for this synthesis method. The following discusses the influence of different catalysts, the chemical reaction in the reactor, the selection of the carrier gas, and the influence of deposition conditions (i.e., reactant ratio, deposition temperature and time). The growth mode of carbon nanofibers is also discussed. Finally, the optimum conditions to obtain boron-doped carbon nanofibers via catalytic CVD are presented.

4.2 Experimental Procedures

4.2.1 Synthesis of Boron-doped Nanofibers via CVD Process

A horizontal CVD reaction furnace is used for the synthesis. A schematic of the reaction furnace is given in Figure 4.1. The reaction furnace includes a Thermolyne 21100 tube furnace, Aera Inc. D980C Mass Flow Controller, Matheson Inc. FM-1050 flowmeters, a standard roughing pump, a mineral oil hydrocarbon trap, and a sodium hydroxide trap. The reactant gases are BCl_3 (MG Industries, CP grade 99.9% pure) and C_6H_6 (Alfa Aesar, spectrophotometric grade 99.5+%). The carrier gas used is either UHP H_2 (Mills Welding & Specialty Gases) or UHP He (Rodger Welding Supply). Fused quartz slides ($1\text{cm} \times 1\text{cm}$, 1mm thick) are positioned in the central hot zone (3" long) of the reactor as the deposition substrates.

Ferrocene (Alfa Aesar, 99%), thin metal films, and nickel powder (Alfa Aesar, 99.8% pure, average particle size of 80-150nm) are used separately as the catalyst to grow filamentous carbon. Ferrocene is dissolved in benzene (2 wt% in benzene), and then introduced into the reactor with the benzene vapor by the carrier gas flow. Thin metal films (Fe, Ni, Cu and Cr) are deposited on the fused quartz slides by thermal evaporation using a Denton thermal evaporator at 10^{-8} torr. The thickness of the film is determined by a film resistance measurement. Nickel powder (~0.1 mg) is directly distributed on the substrates.

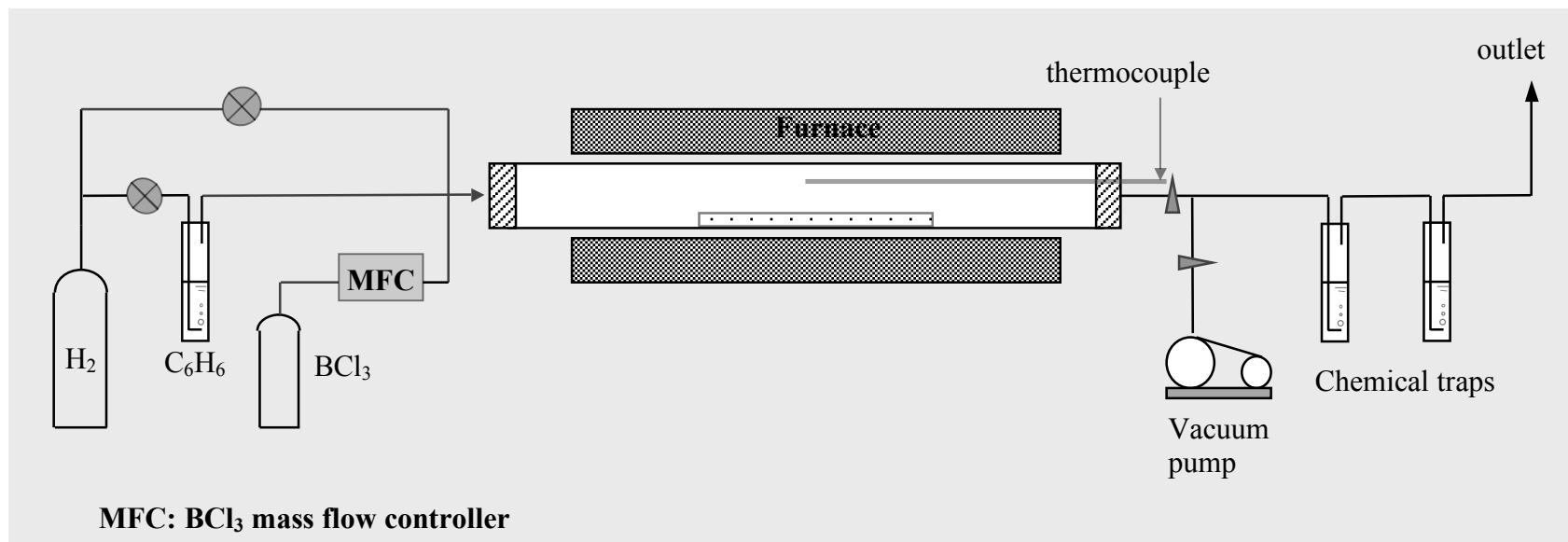


Figure 4.1. Schematic of the CVD reactor for the boron-doped carbon nanotubes and nanofibers.

The reaction parameters of temperature and reactant ratio ($\text{BCl}_3/\text{C}_6\text{H}_6$) are varied. In a typical run, the total volumetric flow rate of gas entering the reactor is 65 ml/min. The absolute system pressure is 93.5 kPa. Benzene, at a flow rate of 10 ml/min, is introduced via the H_2 gas. BCl_3 , flowing at 10 ml/min, is mixed with the benzene prior to introduction into the hot zone. The reaction is undertaken at 800 °C for 30 minutes. After deposition, samples are annealed at 900 °C for 20 hours under 93.5 kPa UHP He.

4.2.2 Scanning Electron Microscopy and Energy-dispersive Spectroscopy

Scanning electron microscopy is performed with an FEI Company QUANTA 200 field-emission source scanning electron microscope (FE-SEM). The Quanta is equipped with an EDAX SUTW/PHILIPS NEW XL-30 Energy Dispersive X-ray microanalysis (EDS) system. The EDS detection unit has a Super Ultra-Thin Window (SUTW) that is 1.3 μm thick, so elements down to, and including boron ($Z=5$), can be detected. The window material X-ray transmission for boron and carbon is 23% and 48%, respectively. The accelerating potential is 20kV, and no coating is used.

4.2.3 Thermodynamic Calculations Using FactSage Software

Thermodynamic calculations are undertaken using a commercial code, FactSage 5.3.1, developed by Pelton, Bale, *et al.* at the Ecole Polytechnique de Montreal.³² A calculation of a reaction using the Reaction Module predicts the reaction possibility (ΔG). The chemical equilibria using the Equilib Module are calculated by minimizing the Gibbs free energy of the species to predict the possible products.

4.3 Results and discussion

4.3.1 Influence of Catalysts

Two major routes to produce catalysts for carbon nanofibers growth by CVD are unsupported and supported methods. The first involves growing the nanofibers in the vapor phase, also known as the floating catalyst method,^{33,34} while the other involves catalysts deposited on supports.^{4,35} Both methods use nano-sized transition metal particles as catalysts, and the distribution of the nanofiber diameter is correlated with the size distribution of the catalyst particles.³⁶ The floating catalyst method is commonly used for the bulk production of nanotubes and nanofibers by CVD. In this method the catalyst precursors, typically metallocenes such as ferrocene and nickelocene, are sublimed and thermally decomposed in the heated reactor and subsequently form the catalyst nanoparticles through nucleation, condensation and coagulation processes. One of the main differences between the supported and unsupported methods is that the residence time of the floating catalyst method is on the order of seconds, so the formation of metal nanoparticles is very quick. It is thus difficult to control particles sizes of the metal catalyst by the floating catalyst approach. On the other hand, the supported catalyst method is more selective, and the size of the catalyst particles is easily controlled. Typically, the supported method is carried out in a step-like style. The first step is to introduce the catalyst or catalyst precursor onto the support that is placed at a fixed position in the furnace, and then to thermally treat it in order to obtain catalyst nanoparticles on the substrate surface. Subsequently, the nanofibers are grown from the nanoparticles in the presence of the carbon source under heat.

We have investigated the synthesis of boron-doped carbon nanofibers both by the floating catalyst method using ferrocene as the catalytic precursor, and by the supported catalyst

method using evaporated metal film as the catalyst. In this paper, we discuss the characteristics of the carbon filaments as a function of the metal particles employed as catalysts.

4.3.1.1 Ferrocene as the Catalyst Precursor

Ferrocene has been used extensively as a catalyst in the floating catalyst method to produce carbon nanotubes and nanofibers. Ferrocene, with a formula $\text{Fe}(\text{C}_5\text{H}_5)_2$, has a melting point of 175°C , and is readily sublimed over 100°C . During the CVD reaction, ferrocene is thermally decomposed in the vapor phase and forms iron nanoparticles by collision and agglomeration. The iron in the nanotubes is found in the form of $\alpha\text{-Fe}$ surrounded by a small portion of Fe_3C as the minor phase.^{37,38}

Figure 4.2 shows the SEM micrographs of the products deposited at 800°C for 15 min using ferrocene as the catalyst. The total flow rate of this run is 35 ml/min at atmospheric pressure, with a partial pressure ratio $\text{C}_6\text{H}_6: \text{BCl}_3: \text{He} = 4:4:27$. The micrographs reveal that the products are diamond microcrystals having a size of 10-15 μm . No filamentous carbon grows under this condition. The isolated microcrystals exhibit primarily (111) and (100) facets, but are randomly oriented and occasionally twinned. Figure 4.3 shows the SEM images of the products deposited at 800°C for 30 min using ferrocene as the catalyst under the same flow rate. Both diamond microcrystals and carbon filaments exist in the resulting deposit. The size of the diamond microcrystals is also 10-15 μm , but the facet surfaces are less sharp as compared to those deposited at a time of 15 min. The carbon filaments grow when deposited at longer time (30-60 min). The diameter of the filaments ranges from 40-200 nm. The wide distribution of diameters is the result of

the poor control of the particle size of the metal catalyst from the thermal decomposition of ferrocene in a gas phase reaction.

It is noted that under the same deposition conditions (catalyst, temperature and flow rates), deposition time has a significant influence on the growth of diamond microcrystals and filamentous carbon in the CVD system. The diamond microstructure changes with the time, and this is evidenced by SEM micrographs, given in Figure 4.4. Diamond grows very quickly (<15 min) and the size changes little with time. However, the facet surface gets less sharp, and shows signs of etching. The growth of filamentous carbon requires a longer reaction time (> 15 min), and ranges between 30-120 min. It is deduced that the production of diamond is the consequence of ferrocene pyrolysis. There is a competition between the nucleation of diamonds and filaments once the iron nanoparticles (or seeds) form by ferrocene pyrolysis. Studies of diamond growth on carbide-forming refractory metals reveal that diamond nucleation occurs only after the formation of a thin carbide layer (Fe_3C).^{39,40} Lux and Haubner⁴¹ postulated such a model, and suggested that carbon dissolves into the metal particles, resulting in the formation of a stable carbide. Diamond nucleation occurs on the carbide layer when the carbon concentration on the surface reaches its saturation value. The incubation period for nucleation is shortest for the metal that most rapidly achieves a supersaturation of carbon on its surface. In our system, the high surface energy of the nano-sized iron particles helps to achieve a carbide layer and, consequently, the nucleation of diamonds. The increase in size of the isolated crystals at the beginning stage (<15 min) is due to abundant carbon surface diffusion from the relatively large diamond-free area

surrounding the nucleated crystals. After diamond-layer formation, the increase in thickness is proportional to the incoming carbon flux, but with a low carbon yield.⁴² Therefore, diamond microcrystals are observed to grow rapidly at the early stages of the CVD process, but the size changes little after 15 min, and the facet surface becomes etched over time by the corrosive vapors associated with BCl_3 in the system.

According to the observations by SEM, there are two reasons why ferrocene, as floating catalyst, might behave poorly (does not yield nanofibers) in a thermal CVD system containing C_6H_6 , BCl_3 and He. The first reason is the inability to control the size of the metal catalyst, which leads to a wide distribution of filament diameters. The second reason is the rapid nucleation of diamonds at the beginning stage, resulting in a low yield of carbon for nanofiber synthesis.

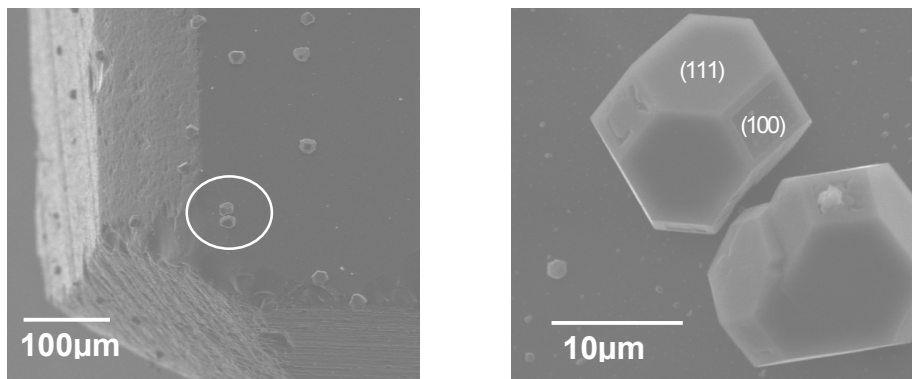


Figure 4.2. The microstructure of diamond microcrystals deposited at 800°C for 15min using ferrocene as the catalyst. Reactants are C_6H_6 and BCl_3 , and He as the carrier gas. Images are secondary electron micrographs taken at 200x and 3kx, respectively.

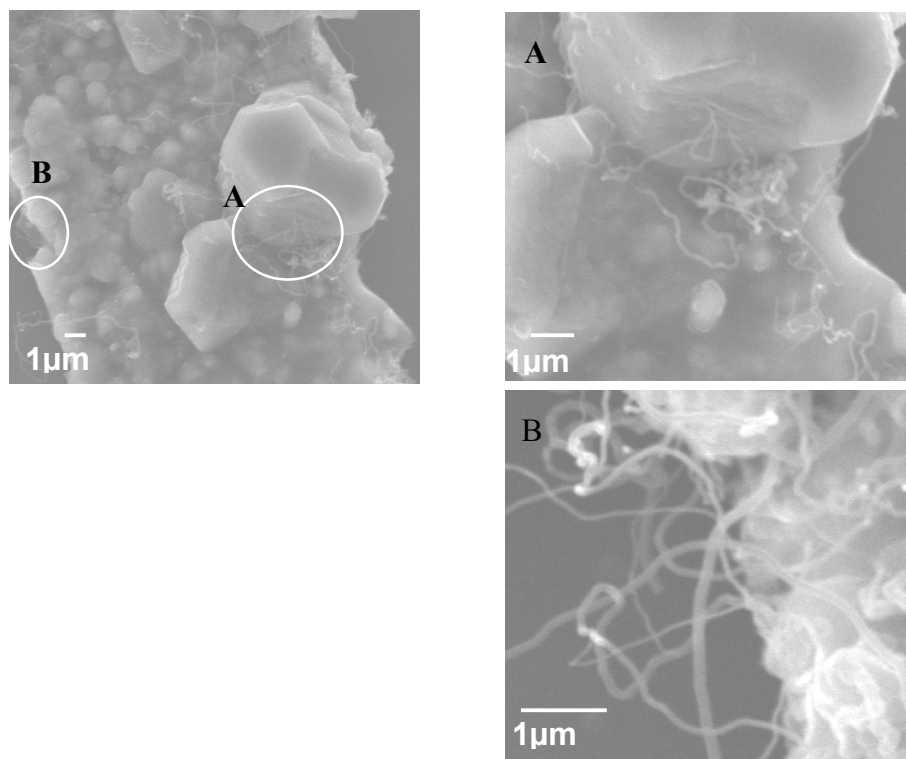


Figure 4.3. The microstructure of diamond microcrystals and nanofibers deposited at 800°C for 30min using ferrocene as the catalyst. Reactants are C_6H_6 and BCl_3 , and He as the carrier gas. Images are secondary electron micrographs taken at 5kx, 10kx and 20kx, respectively.

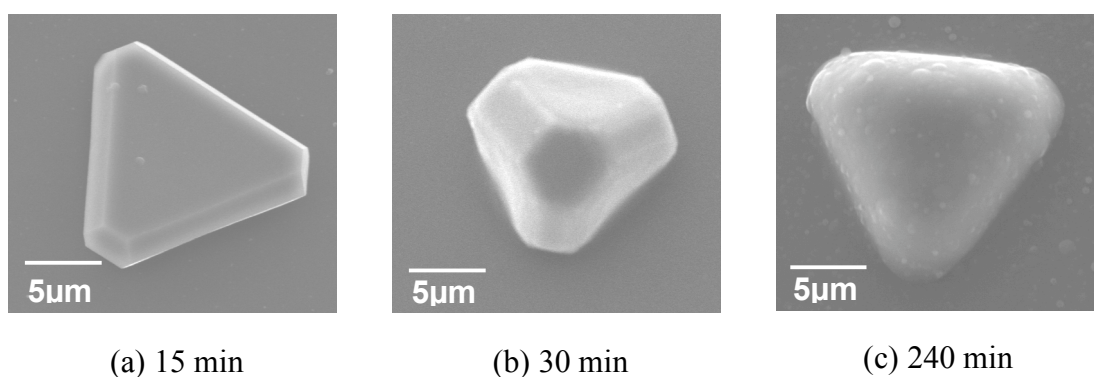


Figure 4.4. Change of the microstructure of a single diamond microcrystal with the CVD deposition time. Microcrystals are deposited at 800°C using ferrocene as the catalyst. Reactants are C_6H_6 and BCl_3 , and He is the carrier gas. Images are secondary electron micrographs taken at 4kx.

4.3.1.2 Metal Particles as the Supported Catalyst

Nanosized transition metal particles supported on the substrates have been widely used in the CVD process to synthesize carbon nanotubes and nanofibers, either in oxide or metallic forms, or as mixtures. The most important property of the metals, with regard to formation of filamentous carbon, is the ability to catalytically decompose vaporized carbon-containing molecules, i.e., carbon sources. The suitability of transition metals as catalysts is due to their various physical and chemical properties, including melting point, equilibrium vapor pressure, carbon solubility and carbon diffusion rate in the metal.

In order to select an effective catalyst, we explored the ability of a few catalysts to form boron-doped carbon nanofibers, including Ni powder and thin metal films of Cu, Cr, Fe and Ni. Values of selected physico-chemical properties for the four transition metals in their bulk form are listed in Table 4.1. Iron and nickel, known as catalysts for pure carbon nanotube production, have similar properties, while copper has a low carbon solubility, and chromium has a relatively high melting point. Nanosized metal particles are not commercially available, however, thin metal film is commonly used to create metal nanoparticles. Thermal evaporation is applied to deposit the thin metal film on the fused quartz substrates. The film thickness is on the order of a few nanometers. Under the high temperature of heat treatment (usually the deposition temperature), the thin film breaks up mechanically and subsequently coalesces to form nanoclusters because of the increased surface mobility and strong cohesive forces of the metal atoms.^{43,44} The nanoclusters then catalyze the growth of nanotubes and nanofibers through the carbon dissolution, saturation, and precipitation processes.

Table 4.1. Physico-chemical Properties of Selected Transition Metals ⁴⁵

Macroscopic properties	Iron	Nickel	Chromium	Copper	
Density, at 20°C (g·cm ⁻³)	7.87	8.9	7.1	8.96	
Melting point (°C)	1536	1455	1860	1085	
Coefficient of expansion, 0-100°C (10 ⁻⁶ K ⁻¹)	12.1	13.3	6.5	17.0	
Surface tension (N·m ⁻¹)	at 20°C	2.48	2.22	2.21	1.39
	at T _{melt}	1.87	1.78	1.70	1.29
Equilibrium vapor pressure, at 1000°C (Pa)	6.48×10 ⁻⁵	1.17×10 ⁻⁵	2.36×10 ⁻³	6.0×10 ⁻³	
Carbon solubility, at T _{melt} (at.%)	20.2	13.9	~40	2×10 ⁻⁴	
Carbon diffusion coefficient in metal, at 1000°C (m ² ·s ⁻¹)	1.5×10 ⁻¹¹	2×10 ⁻¹¹	NA	NA	

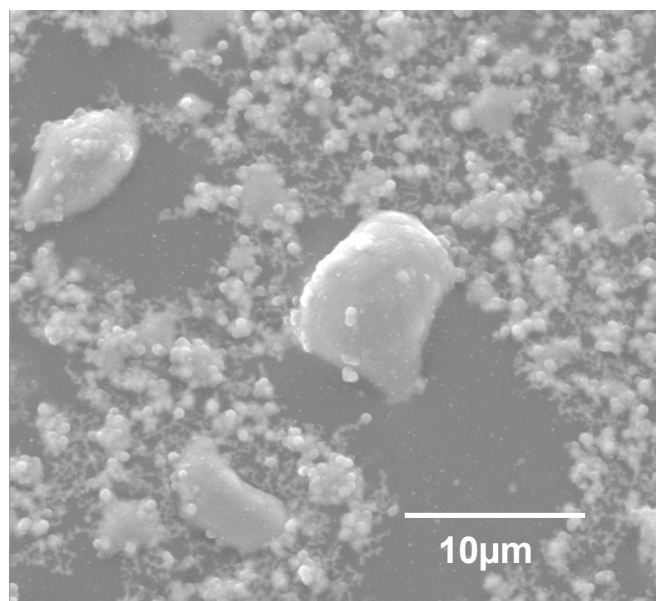
The size of the nanoclusters can be controlled by the thickness of the metal film or by the temperature.^{44,46} Usually, thicker films and higher temperatures lead to the formation of larger metal clusters due to the increased surface migration of the metal atoms. In addition, in the boron doping CVD system, the reaction between metal and the corrosive BCl₃ has to be considered, which would change the composition and catalytic behavior of metal particles.

Figure 4.5a shows the microstructures of the deposits using a thin film of Cu as the catalyst. There is no filamentous carbon produced when using copper as the catalyst. Figure 4.5b is the EDS spectrum, showing the elements detected in the area of Figure 4.5a. Carbon solubility in copper is very low, 2×10⁻⁴ at.% at its melting point.⁴⁵ The high carbon solubility in transition metals has been regarded as one of the most important

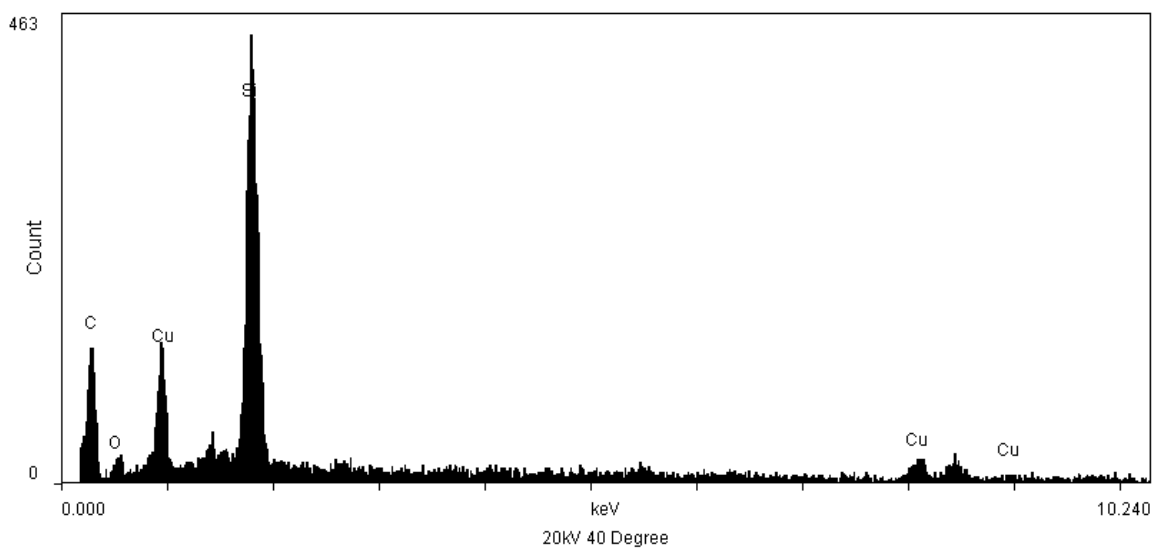
factors enabling their use as catalysts in the production of filamentous carbon.⁴⁷ Thus, Cu itself is not suitable as a catalyst to synthesize carbon nanotubes and nanofibers.

Figure 4.6-4.8 show the microstructures of the deposits using thin film of Cr, Fe and Ni as the catalyst. Although Cr and Fe metals have high carbon solubility, there are not many carbon filaments produced. Using Cr film, cubic microcrystals ($\sim 2\mu\text{m}$) and whiskers are deposited, Figure 4.6. Using Fe film, amorphous carbon particles ($< 3\mu\text{m}$) are observed, Figure 4.7. The EDS spectra reveal the presence of the elements: B, C, Fe, O and Si, where the latter three are from the coated substrate. Carbon filaments are successfully deposited using Ni film, and have a diameter of about 50 nm, and a length exceeding $10\mu\text{m}$, Figure 4.8. Fe has been known as a catalyst for pure carbon nanotubes, thus its inability to be a catalyst in the boron doping system is correlated with an apparent reactivity with BCl_3 gas.

In order to understand the deposition product when using Cr, Fe or Ni film with the presence of BCl_3 in the reaction system, thermodynamic calculations of equilibrium systems of metal (Cr, Fe or Ni), BCl_3 and H_2 are undertaken using FactSage database and software.³² Equilibriums occur at 800°C and 101.3 kPa. The reactants (initial state) and products (final state) and the calculated Gibbs free energy changes (ΔG) are listed in Table 4.2. The negative ΔG s indicate that all the final states of the equilibriums are stable and likely to exist. According to the calculation, Cr with BCl_3 and H_2 generates CrCl_2 and CrB solid, where CrCl_2 is a needle-like crystal and hygroscopic.⁴⁸ The grass-like whiskers produced via the CVD reaction, shown in Figure 4.6, are soluble in water



(a) SEM image



(b) EDS spectrum

Figure 4.5. (a) The SEM image and (b) EDS spectrum of the deposit using Cu film as the catalyst. Reactants are C_6H_6 and BCl_3 , and H_2 is the carrier gas, deposited at $800^\circ C$ for 45 min. Image is secondary electron signals taken at 2kx, and EDS spectrum is frame scan on the whole area.

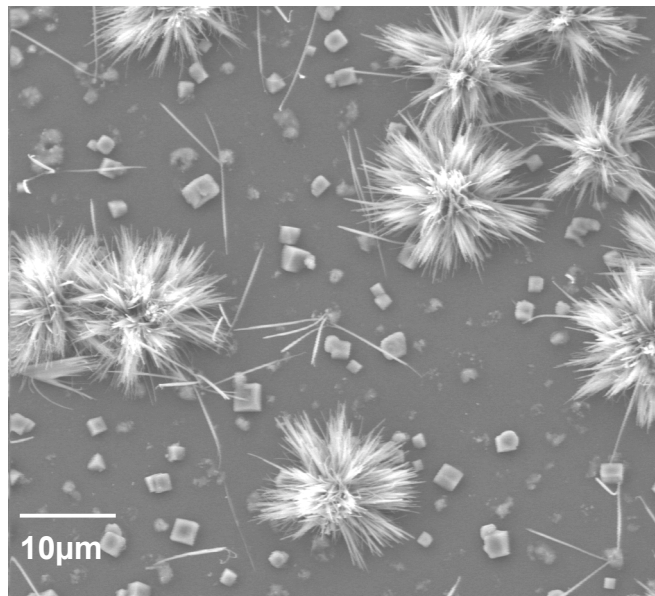
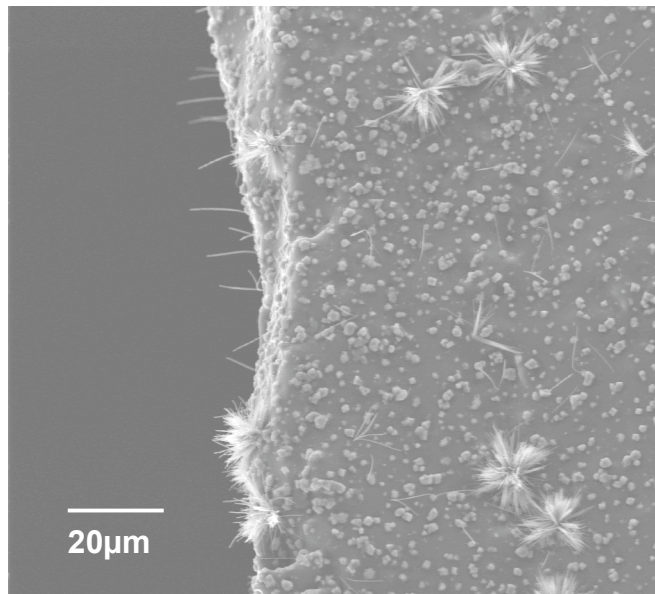
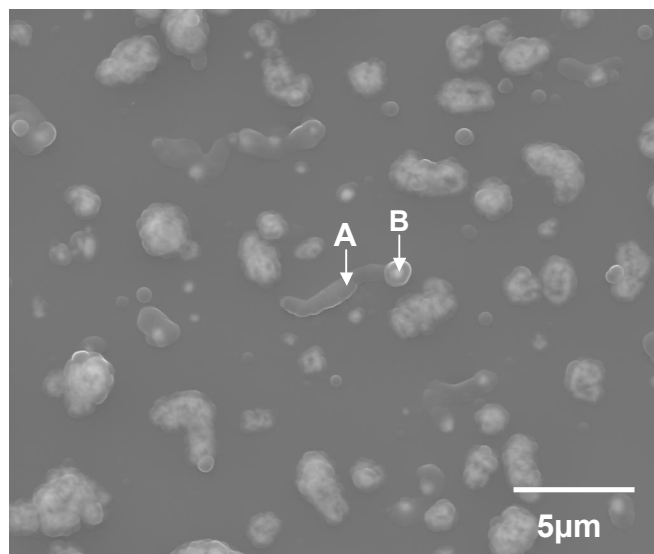
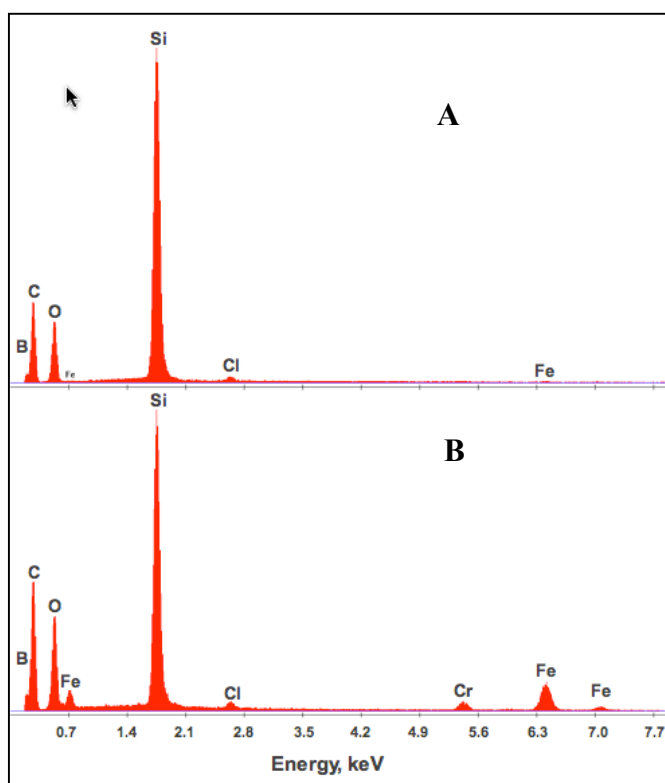


Figure 4.6. The SEM images of the deposit using chromium film as the catalyst. Reactants are C_6H_6 and BCl_3 , and H_2 is the carrier gas, deposited at $800^\circ C$ for 45min. Images are secondary electron signals taken at 500x and 1kx, respectively.



(a) the SEM image



(b) EDS spectra on selected area A and B

Figure 4.7. (a) The SEM image and (b) EDS spectra of the deposit using iron film (~4nm thick) as the catalyst. Reactants are C_6H_6 and BCl_3 , and H_2 is the carrier gas, deposited at $800^\circ C$ for 30 min. Image is 50% secondary electron signals and 50% backscattering electron signals taken at 5kx, and EDS spectra is spot scan on the selected area A and B.

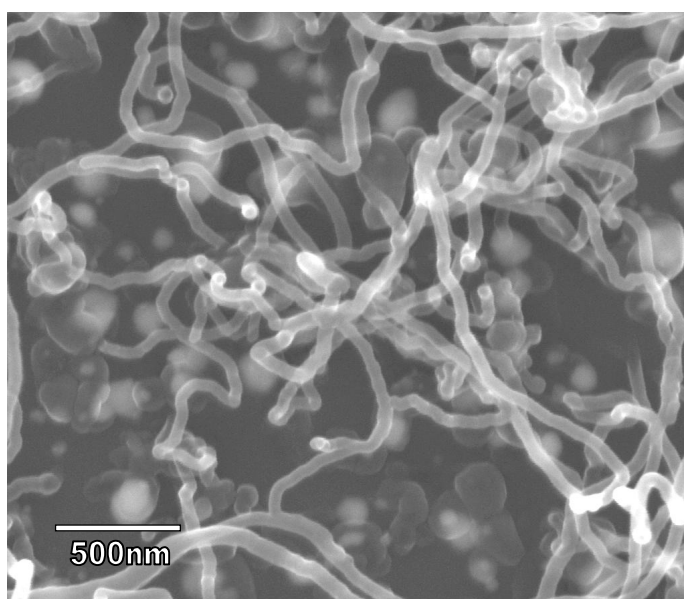
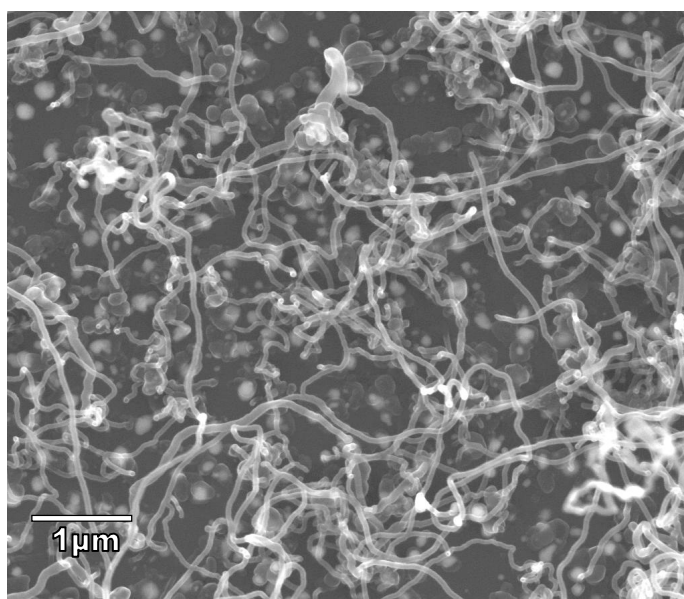


Figure 4.8. The SEM images of the deposit using nickel film (~5 nm thick) as the catalyst. Reactants are C_6H_6 and BCl_3 , and H_2 is the carrier gas, deposited at $750^\circ C$ for 30 min. Images are secondary electron signals taken at 20x and 50kx, respectively.

Table 4.2. Thermodynamic Calculations of Equilibrium Reactions at 800°C and 101.3kPa.

Substances at initial state	Substances at final state	ΔG (kJ)
Solid phase: Cr 1 mol	Solid phase: CrCl ₂ 0.52 mol CrB 0.48 mol	-47.9
Gas phase: BCl ₃ 1 mol H ₂ 1 mol	Gas phase: BCl ₃ 0.50 mol H ₂ 0.78 mol HCl 0.41	
Solid phase: Fe 1 mol	Solid phase: FeB 0.60 mol	-24.1
Gas phase: BCl ₃ 1 mol H ₂ 1 mol	Gas phase: BCl ₃ 0.39 mol H ₂ 0.49 mol HCl 1.02 mol FeCl ₂ 0.23 mol (FeCl ₂) ₂ 0.09 mol	
Solid phase: Ni 1 mol	Solid phase: Ni 0.21 mol Ni ₄ B ₃ 0.20 mol	-30.0
Gas phase: BCl ₃ 1 mol H ₂ 1 mol	Gas phase: BCl ₃ 0.41 mol H ₂ 0.11 mol HCl 1.77 mol	

and the aqueous solution is blue. Therefore, those whiskers are CrCl₂ instead of carbon-based filaments. During the equilibrium reaction at 800°C, Fe with BCl₃ and H₂ generates FeB solid and FeCl₂ and (FeCl₂)₂ vapor. There are 40 mol% Fe transferred into the vapor phase, and no metallic form is left in the final state. Although there might be reactions involving the carbon source in the CVD system, the production of iron compounds in the vapor phase at 800°C leads to a large mass loss of iron in its solid state. Additionally, no evidence indicates that FeB (refractory solid, orthorhombic crystal structure) can be a catalyst for filamentous carbon growth. As a result, in the CVD reaction using a thin film of Fe, no carbon filaments are obtained. As for nickel, the thermodynamic calculation reveals that ~20 mol% metallic nickel survives in the final state and the remainder of the nickel is transferred into solid boride. At this point, one can expect that nickel is the most capable catalyst among the three metals (Cr, Fe and Ni)

for synthesis of boron-doped carbon nanofiber or nanotube with the presence of corrosive BCl_3 as the boron source. The microstructure of the deposit in Figure 4.8 also confirms that nickel can be a catalyst for boron-doped carbon filaments.

Figure 4.9 shows the microstructures of the deposits using Ni powder as the catalyst. The particle size of the nickel powder is 80-150 nm, which is the finest particle size commercially available. Uniform dispersion of this fine nickel powder on the fused quartz slide is difficult due to the high surface energy; therefore, the nickel particles are sitting on the substrate as micro-size clusters. Carbon filaments are obtained, and have an average diameter of ~ 50 nm, similar to the diameter of those obtained using a nickel film as the catalyst. However, the diameter size distribution is large. There are also some short and fat filaments ($\sim 1\ \mu\text{m}$ in length and ~ 150 nm in diameter). This results from the wide size distribution of the particles in the commercial metal powder.

In summary, nickel is a suitable metal to synthesize boron-doped carbon nanofibers when using C_6H_6 and BCl_3 as the reactant, and H_2 as the carrier gas via the thermal CVD process. Both nickel thin film (of several nanometers thick) and nickel powder (in very fine particle size) are able to catalyze nanofibers having an average diameter of ~ 50 nm. Because of the limited availability and wide particle size distribution of nickel powder, a nickel thin film with controlled thickness is a preferable catalyst for the production of boron-doped carbon nanofibers.

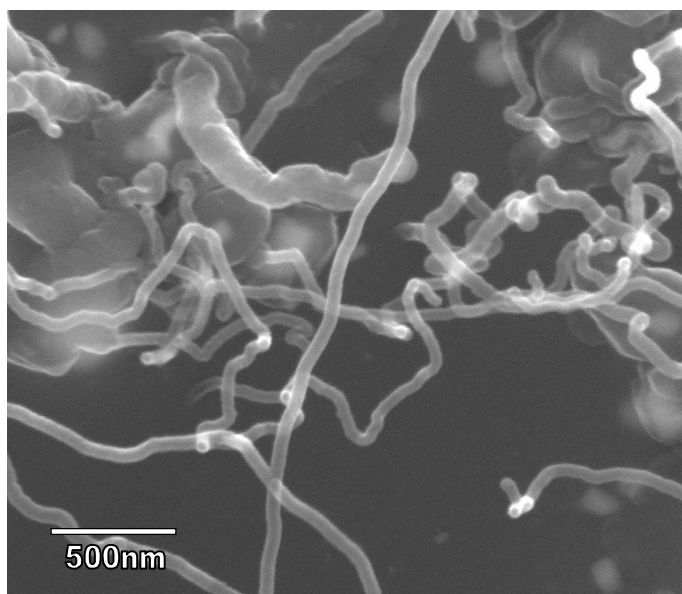
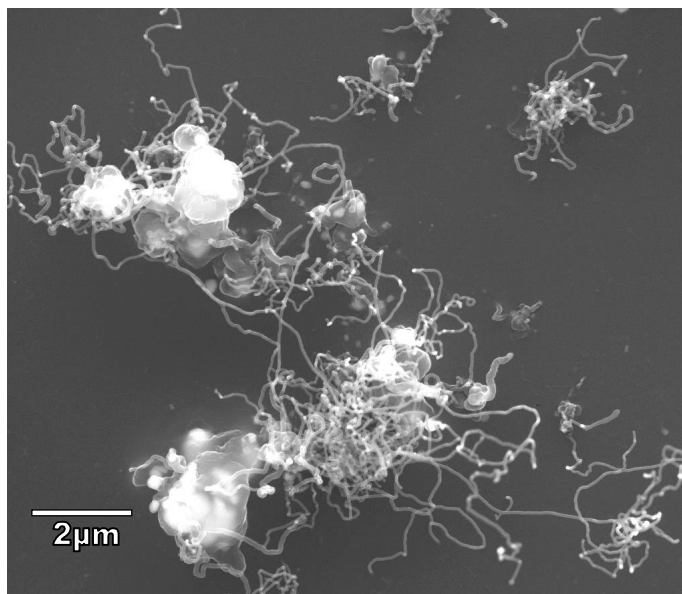


Figure 4.9. The SEM images of the deposit using nickel powder as the catalyst. Reactants are C_6H_6 and BCl_3 , and H_2 is the carrier gas, deposited at $750^\circ C$ for 30 min. Images are secondary electron signals taken at 10x and 50kx, respectively.

4.1.3 Properties of Nickel Nanoparticles

The dependence of the diameter of the carbon nanotubes and nanofibers on the catalyst particle size has been extensively studied experimentally,^{49,50} as well as predicted from the growth mechanisms.^{44,49,51} This finding has been the motivation for decreasing the catalyst particle size to produce the desirable carbon nanotube product, such as single-walled nanotubes. On the other hand, size affects the properties of metal particles. Decreasing the size of the metal particles to the nanometer scale results in a notable increase in the ratio of surface atoms to internal atoms. The atoms located on the surface are in a higher energy state, thus more active and mobile. As a result, various physical and chemical properties of nanoparticles differ from those of the bulk materials. For example, a decrease in melting point and an increase in vapor pressure and carbon solubility have been observed in nano-scaled metal. We use a nickel thin film (<10 nm thick) as the catalyst in this CVD synthesis. Its modified properties, due to the physical form, including a change in the melting point, modified carbon solubility, and carbon diffusion behavior, are discussed below.

One common question asked is whether the catalyst is a liquid or solid during nanofiber or nanotube growth. The melting temperature of metal particles smaller than approximately 100 nm can be decreased significantly by further reducing size.^{52,53} The melting temperature of a particle (T_C) with a radius r can be approximated by

$$T_C = T_0 \left(1 - \frac{2\sigma_{sl} V_m}{\Delta H_{\text{fusion}} r} \right) \quad (4.1)$$

where T_0 , ΔH_{fusion} , V_m , σ_{sl} denote the bulk melting point, the latent heat of fusion, the molar volume and the solid-liquid interfacial energy, respectively.⁵⁴ The melting

temperature of nickel as a function of particle radius is presented in Figure 4.10. As shown, the melting point drops from 1455°C down to 800°C when the particle size is 4-5 nm. It indicates that the catalyst nanoparticles from nickel thin films of ~5nm thick in our CVD reactor at 800°C are likely in the liquid state.

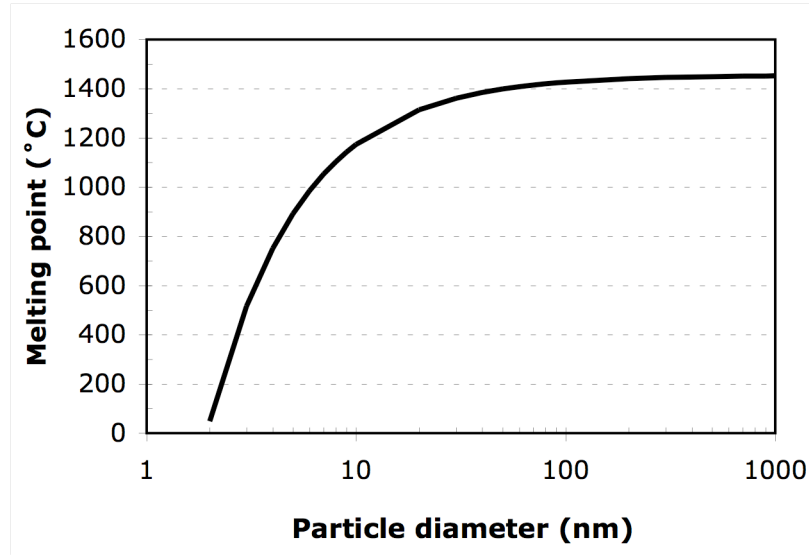


Figure 4.10. Melting point of nickel as a function of particle diameter.

The carbon solubility in metals is a temperature-dependent property, which increases with increasing temperature. The carbon solubility in bulk nickel as a function of temperature is given in Figure 4.11. In addition, the solubility of carbon in metals can be significantly increased due to the small size of the catalyst particles. The size effect on the carbon solubility in metal particles can be estimated as

$$S = S_0 \exp\left(\frac{2\sigma V_m}{RT} \cdot \frac{1}{r}\right), \quad (4.2)$$

where S and S_0 are solubilities in the particle and bulk material, σ , V_m , R , T , r denote the surface energy, the molar volume, the gas constant, the temperature and the particle radius, respectively.⁵⁵ The size effect on the carbon solubility in nickel at the melting

point is presented in Figure 4.12. For 5 nm diameter nickel particles carbon solubility is close to 15%.

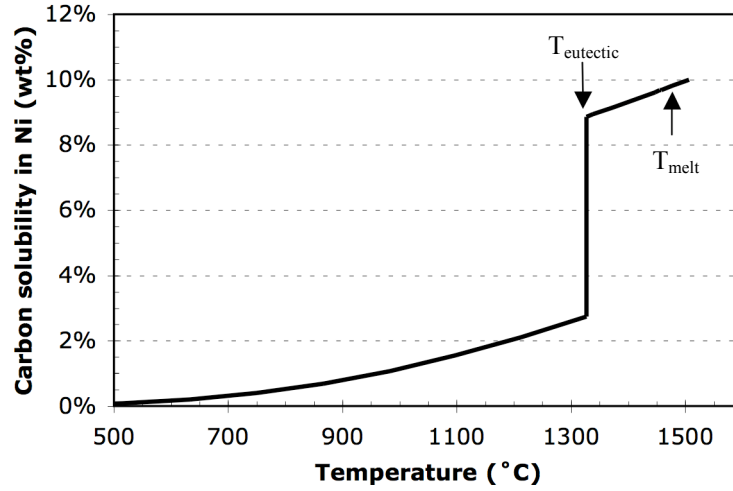


Figure 4.11. Solubility of carbon in nickel at 101.3 kPa as a function of temperature. Derived from Ni-C binary phase diagram using SGTE database.

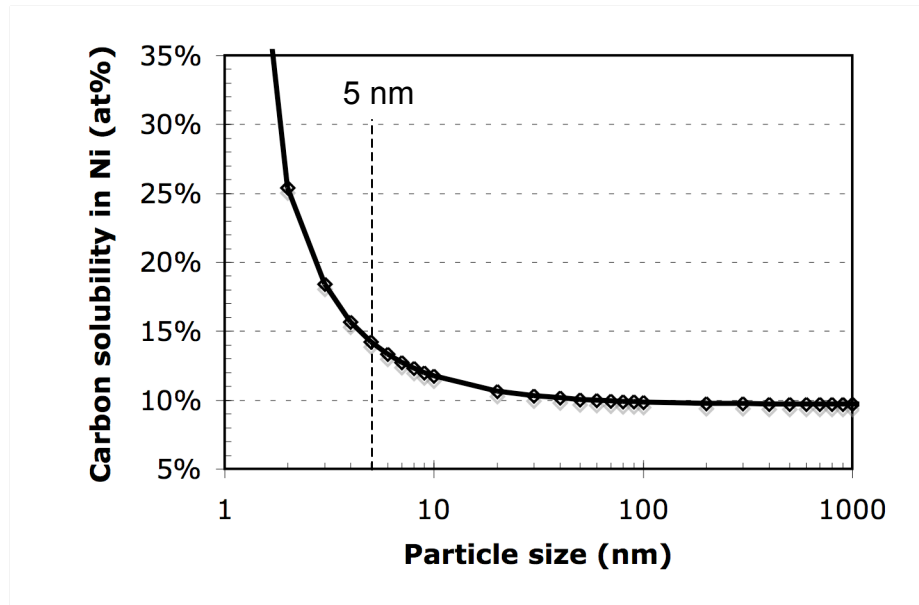


Figure 4.12. Carbon solubility in nickel at melting point as a function of particle size.

Carbon diffusion through the metal particles has been studied with respect to the growth mechanisms of carbon nanotubes and nanofibers. It has been found that the enthalpies for the growth of carbon filaments with iron, nickel or cobalt catalyst were similar to the enthalpy of carbon diffusion through the metal.³ Thus, the rate-determining step in the growth is believed to be the diffusion of carbon through the catalyst. The expression of the diffusion coefficient is

$$D = D_0 \exp (- Q_d / RT) , \quad (4.3)$$

Where D_0 and Q_d are the temperature-independent pre-exponential factor and the activation energy, respectively.⁵⁶

Two diffusion paths, bulk diffusion and surface diffusion, for carbon in metal particles have been discussed. For carbon diffusion in nickel, the Q_d for bulk diffusion is 145-150 kJ/mol,^{57,58} while the Q_d for surface diffusion is much lower, ~ 30 kJ/mol on polycrystalline Ni.⁵⁹ Baker *et al.*⁶⁰ first postulated a bulk diffusion mechanism, and this has been commonly accepted to account for the formation of both nanotubes and nanofibers. Baird *et al.*¹ and Oberlin *et al.*⁶¹ proposed another common growth mechanism involving surface diffusion instead of bulk diffusion. Since the metal particles for nanotube growth are nano-sized, especially 1-3 nm for single walled nanotubes, the ratio of surface atoms to internal atoms is significantly higher. The surface diffusion mechanism has to be involved in the growth process. Temperature is a factor in determining the diffusion path as well. Hofmann *et al.*⁶² investigated the low-temperature growth of carbon nanotubes and nanofibers by plasma-enhanced CVD and found the activation energy for the growth rate is ~ 23 kJ/mol at low temperature (500-

700°C), which is similar to that for surface diffusion. We discuss the carbon diffusion and the growth mechanisms of the boron-doped nanofibers deposited in our system combined with the nano-structure observation in Chapter 6.

4.3.2 Pyrolysis Reaction of Benzene

The term pyrolysis is defined as the conversion of the carbon feedstock to solid carbon as the main product, and to different volatile compounds as by-products.⁶³ The amorphous carbon is deposited from the pyrolysis of carbon feedstock, while the carbon nanotubes and nanofibers are grown from the catalytic decomposition of the carbon feedstock gas. Carbon-containing molecules, ranging from aliphatic and aromatic hydrocarbons to carbon monoxide (CO), alcohols and fullerenes, can be used as sources of carbon.^{20,49,64,65}

Benzene is used as the carbon source in our work. The driving force for the pyrolytic reaction of benzene can be derived from a plot of the Gibbs free energy change (ΔG) of the benzene decomposition versus temperature (generated using FactSage software and database³²) as shown in Figure 4.13. According to the thermodynamic calculation, the forward reaction producing elementary carbon is favored with an increase in temperature. However, the pyrolysis of benzene below 800°C leads to biphenyl as the main by-product, as well as small amount of terphenyls and polyphenyls.⁶³ Complete pyrolysis to the elements carbon and hydrogen takes place at temperatures above 900°C. During the CVD reaction of this study at temperatures between 750°C to 900°C, the formation of a

pale yellow, transparent, flaky crystal is observed on the tubing inner wall at the exhaust outlet. This crystal is identified as biphenyl by measuring the melt point at $\sim 69^\circ\text{C}$.

In order to understand the thermodynamics of benzene decomposition with the presence of BCl_3 gas, the calculations of ΔG for equilibrium systems of 1 mol C_6H_6 and 1 mol C_6H_6 with 1 mol BCl_3 versus temperatures are undertaken using FactSage software at an atmospheric pressure, respectively, as shown in Figure 4.14. In 1 mol C_6H_6 system, at temperatures below 600°C , the ΔG of the equilibrium is lower than that of the complete decomposition as given in Figure 4.13. At temperatures above 700°C , the ΔG values are the same. This is because carbon compound by-products such as biphenyl are readily produced at low temperatures as discussed above. There is not much difference in the ΔG value between systems with and without BCl_3 below 700°C . However, ΔG drops more in the system with BCl_3 at high temperatures. This indicates that the driving force of the pyrolytic reaction (decomposition) of benzene increases with the presence of BCl_3 .

The kinetics of thermal decomposition of benzene in a flow system was studied by Hou and Palmer.⁶⁶ It was found that, in the early stage of reaction, the decomposition kinetics can be treated as mixed first- and second-order reactions. The first-order reaction is a chain, while the second-order reaction is the bimolecular formation of biphenyl and hydrogen. The rate constants for the two reactions are $k_I = 10^{9.15} \exp(-217 \text{ kJ/RT}) \text{ sec}^{-1}$ and $k_{II} = 10^{14.0} \exp(-167,000/\text{RT}) \text{ mol}^{-1} \cdot \text{ml} \cdot \text{sec}^{-1}$, respectively. According to this first-order reaction, the carbon yield in our tube furnace (an effective hot zone is 150 mm length and 46 mm diameter) at a flow rate of 35 ml/min, and a temperature of 850°C , is

calculated as 56%. Experimentally, at the same flow rate and temperature for 5 hours using 2 wt.% ferrocene in benzene as the catalyst, a carbon yield of 40% is obtained by measuring the benzene mass loss and the carbon black gain in the furnace. However, the yield of carbon filaments in our system is very low. The catalyst of thin film on selected substrate limits the yield. For example, using the Ni film (~5 nm thick) coated on the quartz slide as the catalyst, the carbon filament gain is ~1 mg/cm² on the substrate after a reaction at 800°C for 30min and with a flow rate of 65 ml/min.

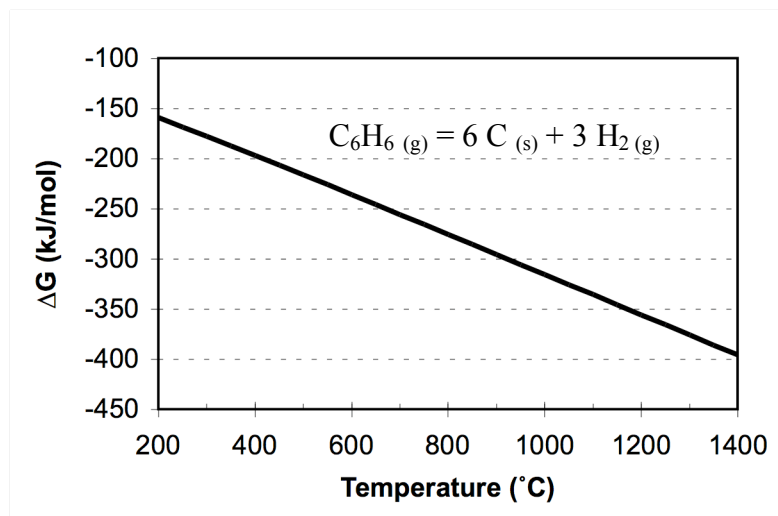


Figure 4.13. Thermodynamic calculations of ΔG for benzene decomposition.

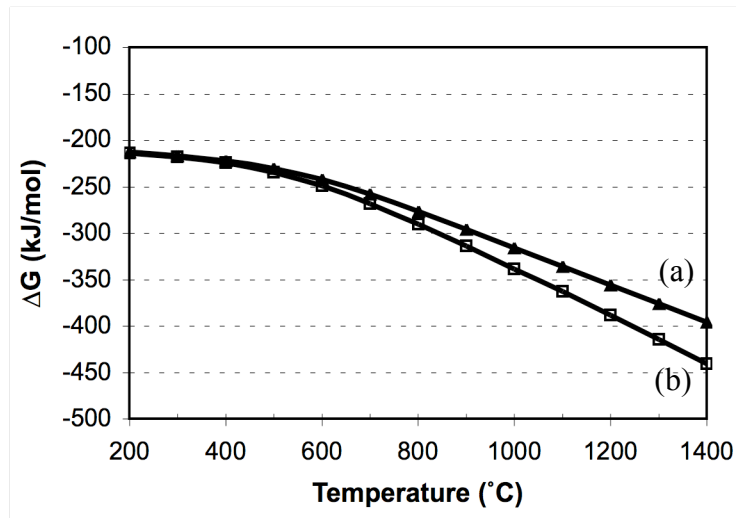
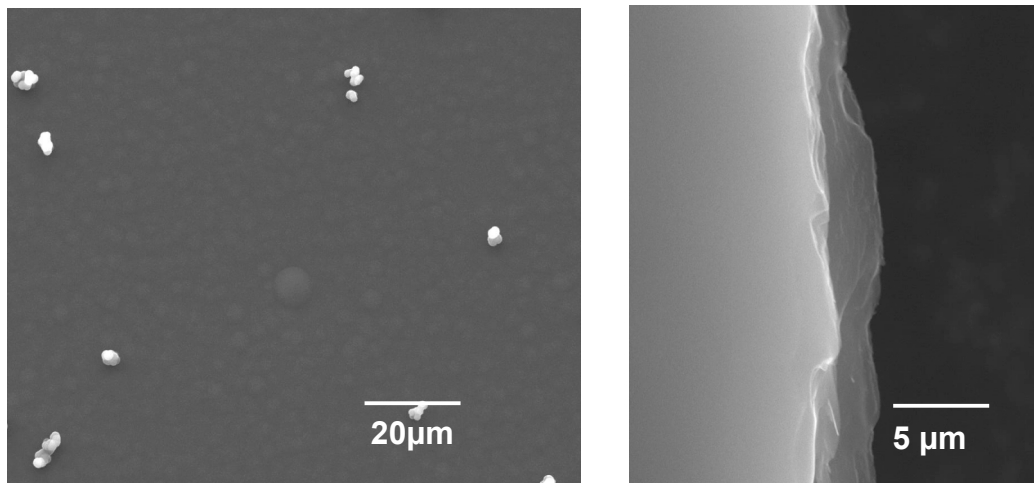


Figure 4.14. Thermodynamic calculations of ΔG for isothermal equilibrium systems at an atmospheric pressure starting with the reactant of (a) 1 mol C_6H_6 , and (b) 1 mol C_6H_6 with 1 mol BCl_3 .

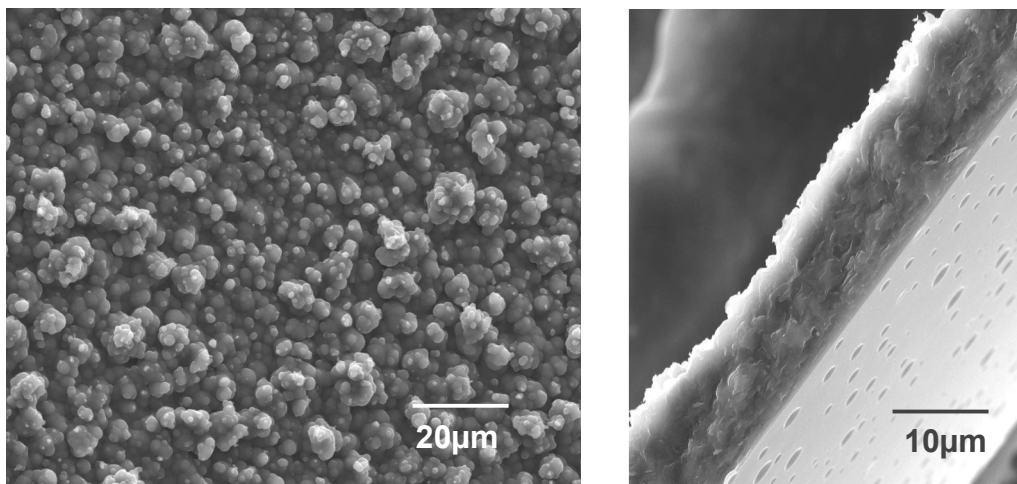
4.3.3 Carrier Gas Selection

Either helium or hydrogen has been used as the carrier gas in our system to synthesize boron-doped carbon nanofibers. Helium is inert and simply dilutes the reactant gases during the reaction. In contrast, H_2 plays an active role during the boron-doped carbon deposition owing to its reducing nature. The microstructures of boron-doped carbon films using helium and H_2 as the carrier gas are given in Figure 4.15. Both films are produced under the same deposition conditions except for the carrier gas. No catalyst is used, so no filamentous carbon grows. The film surface using H_2 is much rougher than that using helium, and the thickness of the film is $\sim 8 \mu m$ compared to $\sim 2 \mu m$. It is obvious that H_2 as a carrier gas enhances the reactivity of the CVD reaction significantly.

Hydrogen has several well-known roles in carbon deposition. First, it is believed to contribute to catalyst particle fragmentation, prevent carbide and oxide formation, and keep the catalyst particle active by reducing it.^{67,68} Second, hydrogen atoms generated as a result of thermal activation undergo H abstraction reactions with stable hydrocarbon molecules, producing highly reactive carbon-containing radical species, such as phenyl radicals ($C_6H_5\cdot$) in our case. These active radicals can diffuse and react, forming C-C bonds, thereby enabling the carbon lattice to propagate quickly.⁶⁹ Third, hydrogen atoms terminate the large number of dangling bonds at the edges of the stacked graphite platelets, thus stabilizing the structure.⁶⁸ Finally, hydrogen also reduces the formation of undesirable carbon deposits from the pyrolysis of carbon feedstock via rehydrogenating the active carbon species in the gas phase.⁷⁰ In our boron doping CVD system, the presence of BCl_3 allows hydrogen atoms to help boron substitute into the aromatic carbon ring by producing HCl, ultimately leading to a boron-doped graphene structure.



(a) Boron-doped carbon film using He as carrier gas



(b) Boron-doped carbon film using H₂ as carrier gas

Figure 4.15. The microstructures of boron-doped carbon film deposited using (a) He and (b) H₂ as carrier gas. Both films are deposited at 800°C for 8 hours, with a reactant ratio $\text{BCl}_3/\text{C}_6\text{H}_6=0.6$. No catalyst is used. Images are secondary electron micrographs.

4.3.4 Influence of the Deposition Conditions

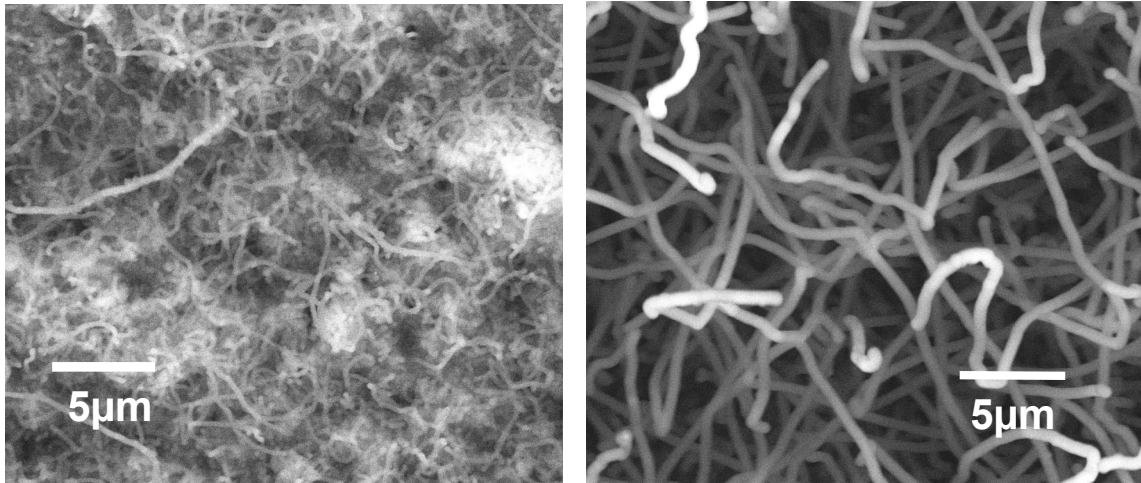
The deposition conditions, including deposition temperatures, durations and reactant ratios ($\text{BCl}_3/\text{C}_6\text{H}_6$), have been investigated. We have found that deposition temperatures and reactant ratios influence the microstructure of the produced boron-doped carbon nanofibers significantly.

4.3.4.1 Deposition Temperature

The deposits have a randomly oriented morphology for all the deposition temperatures (750-900°C), as shown in Figure 4.16. The main characteristics of the fibers, their diameters, increase from $\sim 0.1 \mu\text{m}$ to $\sim 1.5 \mu\text{m}$ with an increase in deposition temperatures. However, the length of the fibers decreases with the temperatures. At a temperature of 900°C, fibers have a diameter exceeding $1.5 \mu\text{m}$, and the length is less than $10 \mu\text{m}$. It is obvious that lower temperatures are conducive to producing nanofibers with a small diameter, and nanofibers cannot be synthesized at a deposition temperature greater than 850°C.

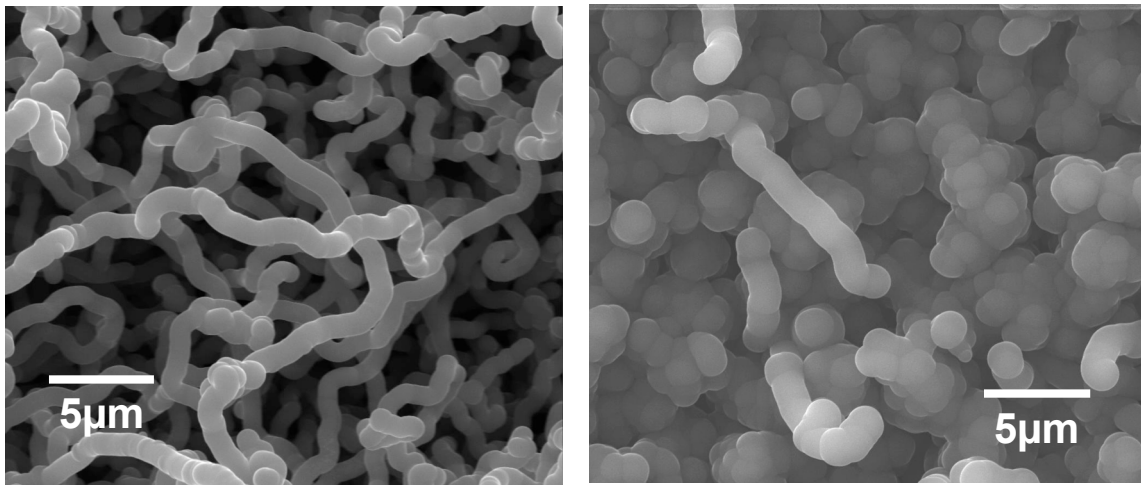
The change in fiber diameter and length as a function of deposition temperature is expected. The size (diameter and length) of the nanofibers is determined by the size of the nuclei (i.e. catalyst particles) and carbon deposition rate. High temperatures lead to the formation of large metal clusters due to increased surface migration of the metal atoms.⁴⁶ The catalyst particle size thus increases with temperature. The carbon deposition rate is dominated by the diffusion path (bulk or surface) and rate. The fiber

length growth rate is proportional to the mass deposition rate, and inversely proportional to the cross-



(a) 750°C

(b) 800°C



(c) 850°C

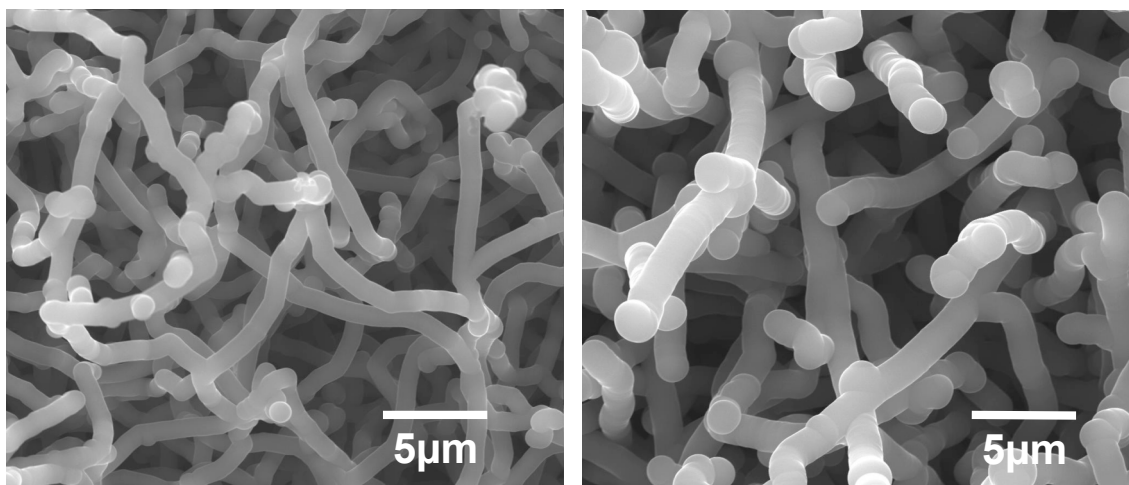
(d) 900°C

Figure 4.16. Change of the microstructure of boron-doped carbon nanofibers with the increase in deposition temperature. The deposition temperatures are (a) 750°C, (b) 800°C, (c) 850°C, and (d) 900°C. All samples are deposited for 30 min and at the reactant ratio $\text{BCl}_3/\text{C}_6\text{H}_6 = 0.6$. Images are secondary electron micrographs taken at the same magnification at 5 kx.

sectional area of the fiber. For the fat fiber, the length growth rate slows down because the mass deposition rate does not match the increase in the fiber cross section. Therefore, by increasing the deposition temperature, we obtain nanofibers having larger diameters and shorter lengths.

4.3.4.2 Deposition Duration

Figure 4.17 shows microstructures of fibers deposited at 800°C and 850°C for 60 min. Compared with the deposition in Figure 4.16 (b) and (c), the deposition time is extended from 30 min to 60 min while keeping the other parameters constant. Although the diameters of the fibers increase with the longer time, the change in length is not obvious. From this point, increasing the time does not enable the synthesis of nanofibers having small diameters.



(a) deposited at 800°C for 60 min

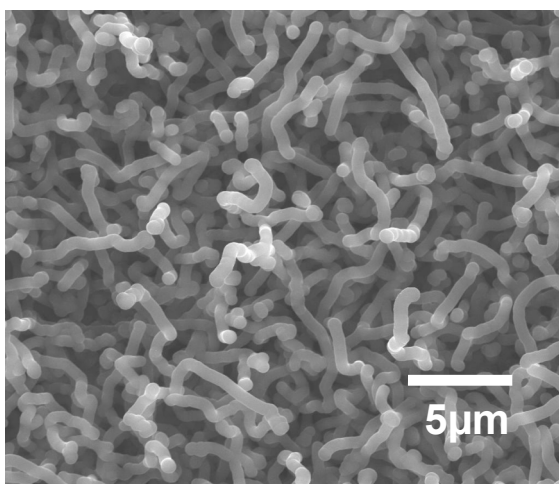
(b) deposited at 850°C for 60 min

Figure 4.17. Microstructure of boron-doped carbon fibers deposited at (a) 800°C for 60min and (b) 850°C for 60min. The reactant ratio is $\text{BCl}_3/\text{C}_6\text{H}_6 = 0.6$. Images are secondary electron micrographs taken at the same magnification at 5 kx.

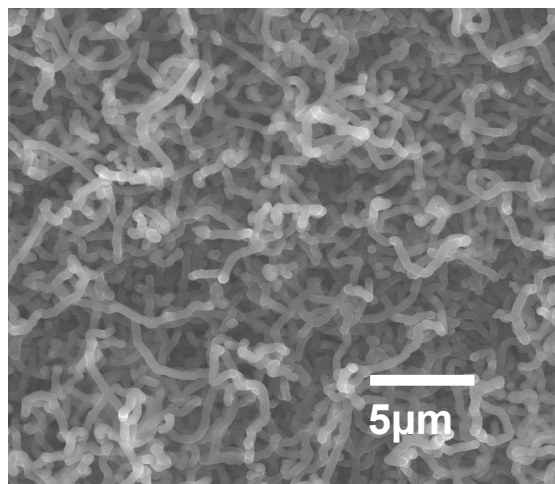
4.3.4.3 Reactant Ratio of $\text{BCl}_3/\text{C}_6\text{H}_6$

Boron-doped nanofibers are grown by using three different reactant ratios ($\text{BCl}_3/\text{C}_6\text{H}_6$) while keeping the other parameters constant. Figure 4.18 (a)-(c) shows the nanofibers grown at 800°C for 30 min with $\text{BCl}_3/\text{C}_6\text{H}_6$ of 0.5, 1 and 2, respectively. For comparative purposes, undoped carbon nanofibers produced under the same condition are shown in Figure 4.18(d). There is a big difference in the morphology of the doped and undoped nanofibers. The fiber diameter is less than 50 nm for the undoped sample, while the doped fiber diameters are more than 100 nm. Interestingly, by increasing the $\text{BCl}_3/\text{C}_6\text{H}_6$ ratio from 0.5 to 2, the fiber diameters decrease and the fiber lengths increase. To confirm the boron influence on the microstructure, we obtained the nanofibers deposited at 800°C for 60 min with $\text{BCl}_3/\text{C}_6\text{H}_6$ of 0.5, 1 and 2, respectively, as given in Figure 4.19. Similarly, the fiber diameters decrease and the fiber lengths increase with increasing the $\text{BCl}_3/\text{C}_6\text{H}_6$ ratio.

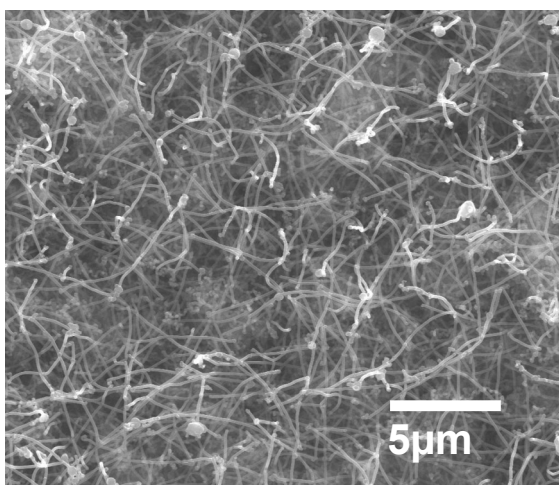
Boron doping (< 5 at.%) is found to improve graphitization of multi-walled carbon nanotubes and increase tube diameter.^{71,72} In our CVD process, the diameter of the nanofibers increases significantly from boron doping using BCl_3 as the boron source. It is likely that BCl_3 modifies the surface properties of the nickel film, and weakens the surface tension of catalyst particles. The size of the catalyst particles decreases with increasing $\text{BCl}_3/\text{C}_6\text{H}_6$ ratios. Therefore, the diameter of nanofibers decreases with increasing $\text{BCl}_3/\text{C}_6\text{H}_6$ ratios.



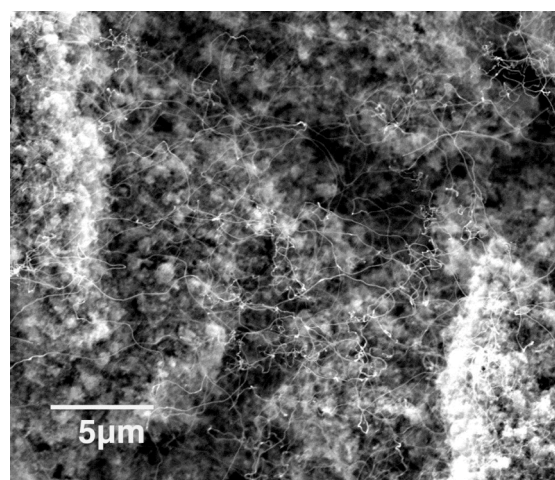
(a) $\text{BCl}_3/\text{C}_6\text{H}_6 = 0.5$



(b) $\text{BCl}_3/\text{C}_6\text{H}_6 = 1$

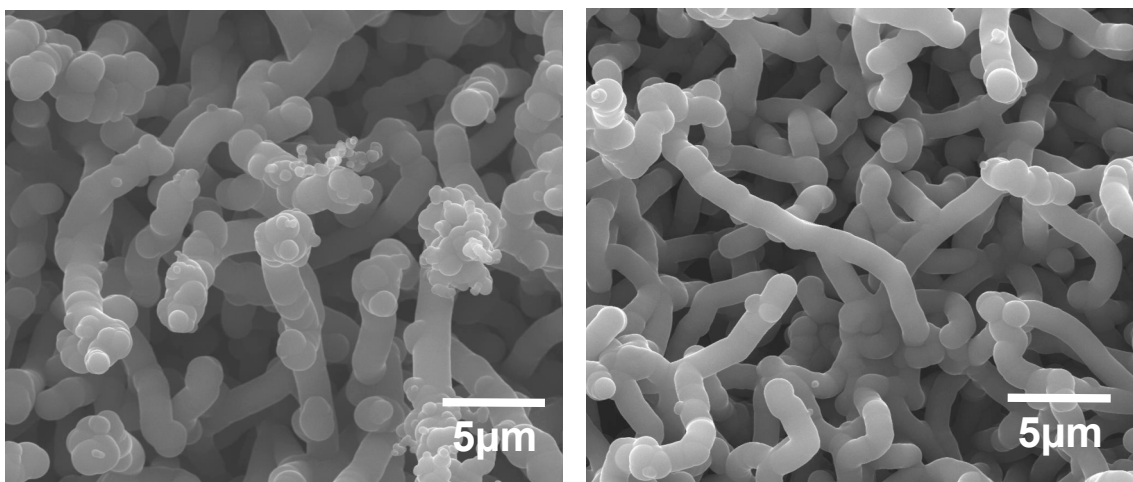


(c) $\text{BCl}_3/\text{C}_6\text{H}_6 = 2$



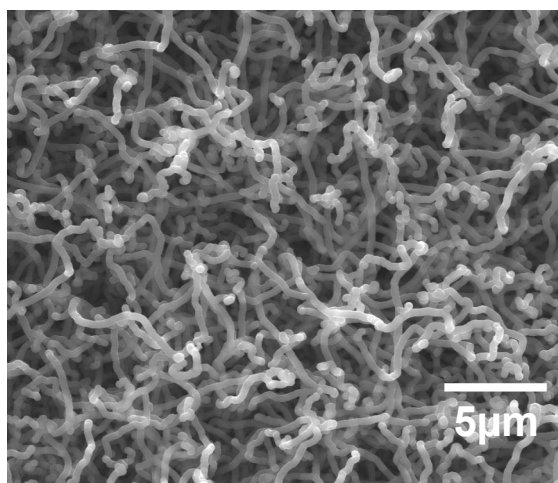
(d) no BCl_3

Figure 4.18. Change of the microstructure of boron-doped carbon nanofibers with the change in reactant ratio $\text{BCl}_3/\text{C}_6\text{H}_6$. The reactant ratios are (a) $\text{BCl}_3/\text{C}_6\text{H}_6 = 0.5$, (b) $\text{BCl}_3/\text{C}_6\text{H}_6 = 1$, (c) $\text{BCl}_3/\text{C}_6\text{H}_6 = 2$ and (d) no BCl_3 . Samples are deposited at 800°C for 30 min, and at a total flow rate of 65 ml/min under 93.5 kPa. Images are secondary electron micrographs taken at the same magnification at 5 kx.



(a) deposited at $\text{BCl}_3/\text{C}_6\text{H}_6 = 0.5$

(b) deposited at $\text{BCl}_3/\text{C}_6\text{H}_6 = 1$



(c) deposited at $\text{BCl}_3/\text{C}_6\text{H}_6 = 2$

Figure 4.19. Change of the microstructure of boron-doped carbon nanofibers with the change in reactant ratio $\text{BCl}_3/\text{C}_6\text{H}_6$. The reactant ratios are (a) $\text{BCl}_3/\text{C}_6\text{H}_6 = 0.5$, (b) $\text{BCl}_3/\text{C}_6\text{H}_6 = 1$, and (c) $\text{BCl}_3/\text{C}_6\text{H}_6 = 2$. Samples are deposited at 800°C for 60 min, and at a total flow rate of 65 ml/min under 93.5 kPa. Images are secondary electron micrographs taken at the same magnification at 5 kx.

4.3.5 Growth Mode of the Boron-doped Carbon Nanofibers

Two different growth modes, tip and base growth (Figure 4.20), have been observed, depending on the strength of the catalyst–substrate interaction.^{2,4} The tip growth takes place when the reaction is weak, and the catalyst particles are lifted from the substrate surface by the growing carbon filaments. On the other hand, this strong interaction favors the base growth and the particle remains pinned at the support surface during the carbon filament growth. The interaction of the catalyst with the substrate surface can be characterized by its contact angle at the growth temperature, such as non-wetting (the contact angle is $> 90^\circ$, weak interaction) and wetting (the contact angle is $< 90^\circ$, strong interaction).⁴ Chhowalla, *et al.*⁴⁶ studied the interaction of Ni film on silica (SiO_2) in detail and found a large contact angle exists at temperatures from 550°C to 900°C , and tip growth is favored in carbon nanotube growth. In our CVD system, a Ni film on a silica substrate was used to grow boron-doped carbon nanofibers, and the deposition temperatures were in the range of 750 – 900°C . Therefore, a tip growth mode was expected to be the growth mode of the boron-doped carbon nanofibers.

Figure 4.21 shows the SEM images of the boron-doped carbon nanofibers deposited at 800°C . The nanofibers have an average diameter of 200 nm and an average length of $5\mu\text{m}$. Note that the SEM images were recorded using 50% secondary electron signals and 50% backscattering electron signals. Thus the intensity (i.e. the brightness) is proportional to the atomic number of the elements that comprise the material. The bright spots in the images are nickel particles, sitting either on the substrate or in the nanofibers. In the magnified image, nickel particles are sitting both on the tip and in the stem of the nanofibers. The nickel particle size in the nanofibers is ~ 50 nm. From the side view of a nanofiber, one can tell that the nanofibers are hollow in the center along the fiber axis and

the inside diameter is the same as the width of the nickel particles, ~50 nm.

The question naturally arises: what is the growth mode of the boron-doped carbon nanofibers? Although nickel particles are observed on the tip of the nanofibers, tip growth mode is unlikely to be the growth mode. There are four reasons: (1) nickel particles are mostly situated on the substrate with a larger size (~100 nm); (2) besides sitting on the tip of the nanofibers, nickel particles also exist in the stem of the nanofibers; (3) the size of nickel particles on the tip of the nanofibers is relatively small compared to the diameter of the nanofibers; (4) nickel particles on the tip of the nanofibers are all covered by the carbon layers that are more than 50 nm thick. The last two reasons indicate that the small nickel particle size of 50 nm is unable to act as the catalyst particle to grow a carbon nanofiber with a diameter of 200 nm by the process of carbon dissolution, saturation and precipitation. Therefore, we propose that the growth mode of the boron-doped carbon nanofibers in the CVD system is base growth instead of tip growth. Since BCl_3 is present in the CVD synthesis system, the surface properties of both nickel particles and silica substrate are modified, and the interaction between the nickel particles and the silica substrate is strengthened. The nanofibers having a hollow channel in the center along the axis nucleate and grow from the nickel particles situated on the substrate. Because of the good wetting between the nickel particle surface and the inner wall of the nanofibers, a small amount of nickel (acting as liquid due to the size effect) is pushed upwards into the central hollow space of the nanofibers by the growth of the nanofibers, similar to capillary action.

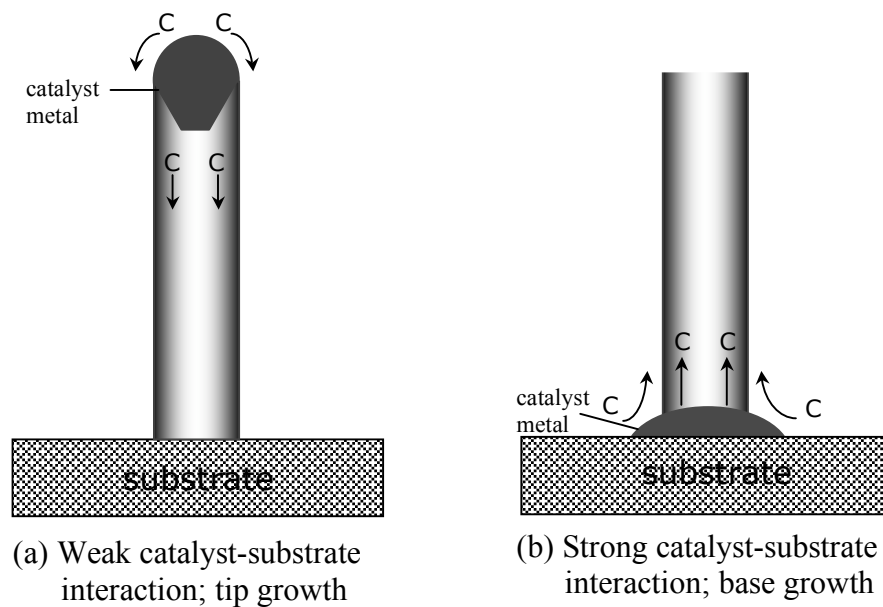
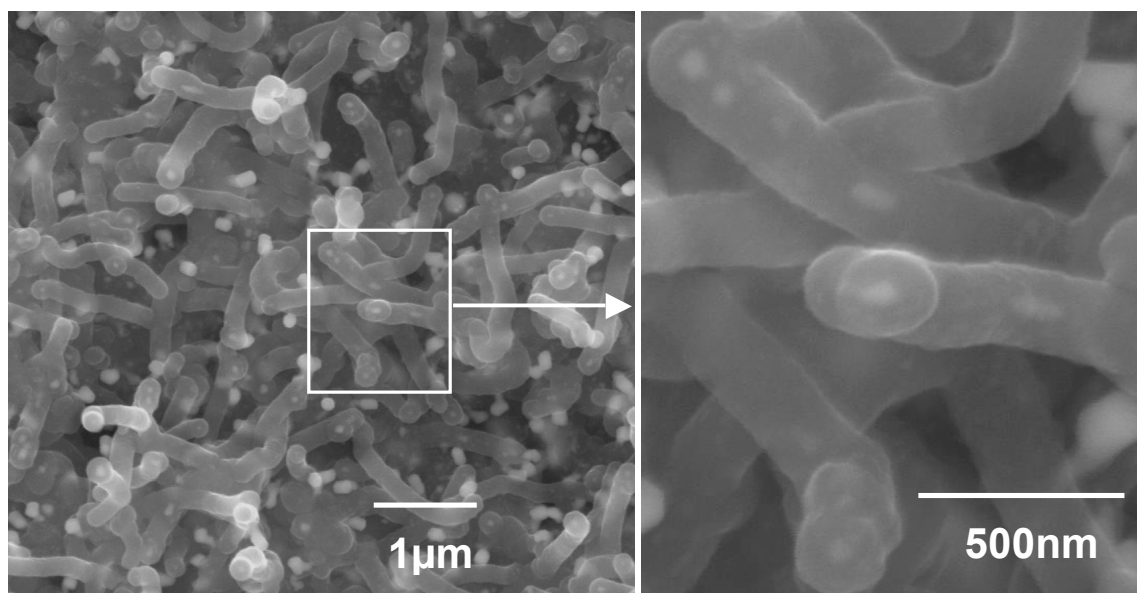


Figure 4.19. Two growth modes of carbon nanotubes or nanofibers, namely tip or base growth, resulting from different catalyst-support interaction. Adapted from Baker.²



Figur 4.20. SEM images of boron-doped carbon nanofibers deposited at 800°C for 30 min using Ni film as the catalyst. Image is 50% secondary electron signals and 50% backscattering electron signals taken at 20kx and 50kx, respectively.

4.4 Conclusions

Boron-doped carbon nanofibers have been synthesized by a catalytic CVD method at 750-900°C from C₆H₆ and BCl₃. A thin nickel film of 4-5 nm was the most preferable as the catalyst. Using hydrogen as a carrier gas enhanced the reactivity of the CVD reaction, and was conducive to boron doping. The deposition temperature and reactant ratio (BCl₃/C₆H₆) have a strong influence on the microstructure of the resulting nanofibers. By increasing the deposition temperatures from 750°C to 900°C, nanofiber diameters increased from 0.1 μm to ~1.5 μm, and lengths decreased from 20 μm to less than 10 μm. By increasing the BCl₃/C₆H₆ ratio from 0.5 to 2 while keeping the other parameters constant, the fiber diameters decreased and the fiber lengths increased. Based on the microstructure observations, a base growth has been proposed as the growth mode of these boron-doped carbon nanofibers.

References

1. T. Baird, J.R. Fryer, and B. Grant, "Carbon Formation on Iron and Nickel Foils by Hydrocarbon Pyrolysis--Reactions at 700°C," *Carbon*, **12** [5] 591-602 (1974).
2. R.T.K. Baker, "Catalytic Growth of Carbon Filaments," *Carbon*, **27** [3] 315-23 (1989).
3. R.T.K. Baker, P.S. Harris, R.B. Thomas, and R.J. Waite, "Formation of Filamentous Carbon from Iron, Cobalt and Chromium Catalyzed Decomposition of Acetylene," *J. Catal.*, **30** [1] 86-95 (1973).
4. N.M. Rodriguez, "A Review of Catalytically Grown Carbon Nanofibers," *J. Mater. Res.*, **8** [12] 3233-50 (1993).
5. S. Iijima, "Helical Microtubules of Graphitic Carbon," *Nature*, **354** [6348] 56-58 (1991).
6. A.G. Rinzler and J.H. Hafner, "Unraveling Nanotubes: Field Emission from an Atomic Wire," *Science*, **269** [5230] 1550-53 (1995).
7. W.B. Choi, D.S. Chung, J.H. Kang, H.Y. Kim, Y.W. Jin, I.T. Han, Y.H. Lee, J.E. Jung, N.S. Lee, G.S. Park, and J.M. Kim, "Fully Sealed, High-Brightness Carbon-Nanotube Field-Emission Display," *Appl. Phys. Lett.*, **75** [20] 3129-31 (1999).
8. H.C. Choi, W. Kim, D. Wang, and H. Dai, "Delivery of Catalytic Metal Species onto Surfaces with Dendrimer Carriers for the Synthesis of Carbon Nanotubes with Narrow Diameter Distribution," *J. Phys. Chem. B*, **106** [48] 12361-65 (2002).
9. D.-S. Chung, S.H. Park, H.W. Lee, J.H. Choi, S.N. Cha, J.W. Kim, J.E. Jang, K.W. Min, S.H. Cho, M.J. Yoon, J.S. Lee, C.K. Lee, J.H. Yoo, J.-M. Kim, J.E. Jung, Y.W. Jin, Y.J. Park, and J.B. You, "Carbon Nanotube Electron Emitters with a Gated Structure Using Backside Exposure Processes," *Appl. Phys. Lett.*, **80** [21] 4045-47 (2002).
10. I.T. Han, H.J. Kim, Y.-J. Park, N. Lee, J.E. Jang, J.W. Kim, J.E. Jung, and J.M. Kim, "Fabrication and Characterization of Gated Field Emitter Arrays with Self-Aligned Carbon Nanotubes Grown by Chemical Vapor Deposition," *Appl. Phys. Lett.*, **81** [11] 2070-72 (2002).
11. S.J. Tans, A.R.M. Verschueren, and C. Dekker, "Room-Temperature Transistor Based on a Single Carbon Nanotube," *Nature*, **393** [6680] 49-52 (1998).
12. A. Bachtold, P. Hadley, T. Nakanishi, and C. Dekker, "Logic Circuits with Carbon Nanotube Transistors," *Science*, **294** [5545] 1317-20 (2001).

13. Z. Chen, J. Appenzeller, Y. Lin, J. Sippel-Oakley, A.G. Rinzler, J. Tang, S.J. Wind, P.M. Solomon, and P. Avouris, "An Integrated Logic Circuit Assembled on a Single Carbon Nanotube," *Science*, **311** [5768] 1735 (2006).
14. C. Niu, E.K. Sichel, R. Hoch, D. Moy, and H. Tennent, "High Power Electrochemical Capacitors Based on Carbon Nanotube Electrodes," *Appl. Phys. Lett.*, **70** [11] 1480-82 (1997).
15. E. Frackowiak, K. Metenier, V. Bertagna, and F. Beguin, "Supercapacitor Electrodes from Multiwalled Carbon Nanotubes," *Appl. Phys. Lett.*, **77** [15] 2421-23 (2000).
16. J. Sandler, P. Werner, M.S.P. Shaffer, V. Demchuk, V. Altstadt, and W. A.H., "Carbon-Nanofibre-Reinforced Poly(Ether Ether Ketone) Composites," *Compos. Pt. A, Appl. Sci. Manuf.*, **33** [8] 1033-39 (2002).
17. D.D.L. Chung, "Electromagnetic Interference Shielding Effectiveness of Carbon Materials," *Carbon*, **39** [2] 279-85 (2001).
18. D.D.L. Chung, "Comparison of Submicron-Diameter Carbon Filaments and Conventional Carbon Fibers as Fillers in Composite Materials," *Carbon*, **39** [8] 1119-25 (2001).
19. J. Kong, A.M. Cassell, and H. Dai, "Chemical Vapor Deposition of Methane for Single-Walled Carbon Nanotubes," *Chem. Phys. Lett.*, **292** [4-6] 567-74 (1998).
20. J.H. Hafner, M.J. Bronikowski, B.R. Azamian, P. Nikolaev, A.G. Rinzler, D.T. Colbert, K.A. Smith, and R.E. Smalley, "Catalytic Growth of Single-Wall Carbon Nanotubes from Metal Particles," *Chem. Phys. Lett.*, **296** [1] 195-202 (1998).
21. S. Fan, M.G. Chapline, N.R. Franklin, T.W. Tombler, A.M. Cassell, and H. Dai, "Self-Oriented Regular Arrays of Carbon Nanotubes and Their Field Emission Properties," *Science* **283** [5401] 512-14 (1999).
22. Y. Zhang, A. Chang, J. Cao, Q. Wang, W. Kim, Y. Li, N. Morris, E. Yenilmez, J. Kong, and H. Dai, "Electric-Field-Directed Growth of Aligned Single-Walled Carbon Nanotubes," *Appl. Phys. Lett.*, **79** [19] 3155-57 (2001).
23. A. Ural, Y. Li, and H. Dai, "Electric-Field-Aligned Growth of Single-Walled Carbon Nanotubes on Surfaces," *Appl. Phys. Lett.*, **81** [18] 3464-66 (2002).
24. M. Terrones, N. Grobert, J. Olivares, J.P. Zhang, H. Terrones, K. Kordatos, W.K. Hsu, J.P. Hare, P.D. Townsend, K. Prassides, A.K. Cheetham, H.W. Kroto, and D.R.M. Walton, "Controlled Production of Aligned-Nanotube Bundles," *Nature*, **388** [6637] 52-54 (1997).

25. Z.F. Ren, Z.P. Huang, J.W. Xu, J.H. Wang, P. Bush, M.P. Siegal, and P.N. Provencio, "Synthesis of Large Arrays of Well-Aligned Carbon Nanotubes on Glass," *Science* **282** [5391] 1105-07 (1998).
26. L. An, J.M. Owens, L.E. McNeil, and J. Liu, "Synthesis of Nearly Uniform Single-Walled Carbon Nanotubes Using Identical Metal-Containing Molecular Nanoclusters as Catalysts," *J. Am. Chem. Soc.*, **124** [46] 13688-89 (2002).
27. Y.C. Choi, Y.M. Shin, Y.H. Lee, B.S. Lee, G.S. Park, W.B. Choi, N.S. Lee, and J.M. Kim, "Controlling the Diameter, Growth Rate, and Density of Vertically Aligned Carbon Nanotubes Synthesized by Microwave Plasma-Enhanced Chemical Vapor Deposition," *Appl. Phys. Lett.*, **76** [17] 2367-69 (2000).
28. H. Dai, J. Kong, C.W. Zhou, N. Franklin, T. Tombler, A. Cassell, S.S. Fan, and M. Chapline, "Controlled Chemical Routes to Nanotube Architectures, Physics and Devices," *J. Phys. Chem. B*, **103** [51] 11246-55 (1999).
29. A. Tanaka, S.-H. Yoon, and I. Mochida, "Preparation of Highly Crystalline Nanofibers on Fe and Fe-Ni Catalysts with a Variety of Graphene Plane Alignments," *Carbon*, **42** [3] 591-97 (2004).
30. M. Endo, "Grow Carbon Fibers in the Vapor Phase," *Chemtech*, **18** [9] 568-76 (1988).
31. A.G. Rinzler, J. Liu, H. Dai, P. Nilolaev, C.B. Huffman, F.J. Rodriguez-Macias, P.J. Boul, A.H. Lu, D. Heymann, D.T. Colbert, R.S. Lee, J.E. Fischer, A.M. Rao, P.C. Eklund, and R.E. Smalley, "Large-Scale Purification of Single-Wall Carbon Nanotubes: Process, Product, and Characterization," *Appl. Phys. A*, **67** [1] 29-37 (1998).
32. C.W. Bale, P. Chartrand, S.A. Degterov, G. Eriksson, K. Hack, R. Ben Mahfoud, J. Melancon, A.D. Pelton, and S. Petersen, "Factsage Thermochemical Software and Databases," *CALPHAD: Comput. Coupling Phase Diagrams Thermochem.*, **26** [2] 189-228 (2002).
33. L. Ci, Y. Li, B. Wei, J. Liang, C. Xu, and D. Wu, "Preparation of Carbon Nanofibers by the Floating Catalyst Method," *Carbon*, **38** [14] 1933-37 (2000).
34. C. Singh, T. Quested, C.B. Boothroyd, P. Thomas, I.A. Kinloch, A.I. Abou-Kandil, and A.H. Windle, "Synthesis and Characterization of Carbon Nanofibers Produced by the Floating Catalyst Method," *J. Phys. Chem. B*, **106** [42] 10915-22 (2002).

35. E. Boellaard, P.K. de Bokx, A.J.H.M. Kock, and J.W. Geus, "The Formation of Filamentous Carbon on Iron and Nickel Catalysts : III. Morphology," *J. Catal.*, **96** [2] 481-90 (1985).
36. A.G. Nasibulin, P.V. Pikhitsa, H. Jiang, and E.I. Kauppinen, "Correlation between Catalyst Particle and Single-Walled Carbon Nanotube Diameters," *Carbon*, **43** [11] 2251-57 (2005).
37. M. Mayne, N. Grobert, M. Terrones, R. Kamalakaran, M. Ruhle, H.W. Kroto, and D.R.M. Walton, "Pyrolytic Production of Aligned Carbon Nanotubes from Homogeneously Dispersed Benzene-Based Aerosols," *Chem. Phys. Lett.*, **338** [2-3] 101-07 (2001).
38. S. Karmakar, S.M. Sharma, P.V. Teredesai, and A.K. Sood, "Pressure-Induced Phase Transitions in Iron-Filled Carbon Nanotubes: X-Ray Diffraction Studies," *Phys. Rev. B: Condens. Matter Mater. Phys.*, **69** [16] 165414.1-14.5 (2004).
39. P.O. Joffreau, R. Haubner, and B. Lux, "Low-Pressure Diamond Growth on Refractory Metals," *Int. J. Refract. Hard Met.*, **7** [4] 186-94 (1988).
40. H. Liu and D.S. Dandy, "Studies on Nucleation Process in Diamond CVD: An Overview of Recent Developments," *Diamond Relat. Mater.*, **4** [10] 1173-88 (1995).
41. B. Lux and R. Haubner, "Nucleation and Growth of Low-Pressure Diamond," pp. 579-609 in *Diamond and Diamond-Like Films and Coatings*. Edited by R. E. Clausing, L. L. Horton, J. C. Augus, and P. Koidl. Plenum Press, New York, 1991.
42. W.F. Banholzer and T.R. Anthony, "Isotope Enrichment During Diamond Growth," *Diamond Relat. Mater.*, **1** [12] 1157-60 (1992).
43. V.I. Merkulov, D.H. Lowndes, Y.Y. Wei, G. Eres, and E. Voelkl, "Patterned Growth of Individual and Multiple Vertically Aligned Carbon Nanotubes," *Appl. Phys. Lett.*, **76** [24] 3555-57 (2000).
44. C. Bower, O. Zhou, W. Zhu, D.J. Werder, and S. Jin, "Nucleation and Growth of Carbon Nanotubes by Microwave Plasma Chemical Vapor Deposition," *Appl. Phys. Lett.*, **77** [17] 2767-69 (2000).
45. E.A. Brandes, Ch. 8,11,13,14 in *Smithells Metals Reference Book*. Butterworths, London, 1983.
46. M. Chhowalla, K.B.K. Teo, C. Ducati, N.L. Rupesinghe, G.A.J. Amaratunga, A.C. Ferrari, D. Roy, J. Robertson, and W.I. Milne, "Growth Process Conditions

- of Vertically Aligned Carbon Nanotubes Using Plasma Enhanced Chemical Vapor Deposition " *J. Appl. Phys.*, **90** [10] 5308-17 (2001).
47. A. Moisala, A.G. Nasibulin, and E.I. Kauppinen, "The Role of Metal Nanoparticles in the Catalytic Production of Single-Walled Carbon Nanotubes—A Review," *J. Phys.: Condens. Matter*, **15** [42] S3011-S35 (2003).
 48. *Handbook of Chemistry and Physics*, 84th ed.; pp. 4-37. Edited by D.R. Lide CRC, New York, 2003.
 49. H. Dai, A.G. Rinzler, P. Nikolaev, A. Thess, D.T. Colbert, and R.E. Smalley, "Single-Wall Nanotubes Produced by Metal-Catalyzed Disproportionation of Carbon Monoxide," *Chem. Phys. Lett.*, **260** [3] 471-75 (1996).
 50. C.L. Cheung, A. Kurtz, H. Park, and C.M. Lieber, "Diameter-Controlled Synthesis of Carbon Nanotubes," *J. Phys. Chem. B*, **106** [10] 2429-33 (2002).
 51. S.B. Sinnott, R. Andrews, D. Qian, A.M. Rao, Z. Mao, E.C. Dickey, and F. Derbyshire, "Model of Carbon Nanotube Growth through Chemical Vapor Deposition," *Chem. Phys. Lett.*, **315** [1] 25-30 (1999).
 52. Q. Jiang, S. Zhang, and M. Zhao, "Size-Dependent Melting Point of Noble Metals," *Mater. Chem. Phys.*, **82** [1] 225-27 (2003).
 53. Y. Qi, T. Cagin, W.L. Johnson, and W.A. Goddard III, "Melting and Crystallization in Ni Nanoclusters: The Mesoscale Regime," *J. Phys. Chem.*, **115** [1] 385-94 (2001).
 54. Y. Xue, Q. Zhao, and C. Luan, "The Thermodynamic Relations between the Melting Point and the Size of Crystals," *J. Colloid Interface Sci.*, **243** [2] 388-90 (2001).
 55. A.W. Adamson, *Physical Chemistry of Surface*; p. 332. Wiley, New York, 1982.
 56. W.D. Callister, *Material Science and Engineering: An Introduction*; pp. 89-107. Wiley, New York, 1997.
 57. S. Diamond and C.A. Wert, "Diffusion of Carbon in Nickel above and Below the Curie Temperature," *Trans. Metall. Soc. AIME*, **239** [5] 705-09 (1967).
 58. J. Cermak and H. Mehrer, "Tracer Diffusion of ¹⁴C in Austenitic Ni-Fe-Cr Alloys," *Acta Metall. Mater.*, **42** [4] 1345-50 (1994).
 59. J.F. Mojica and L.L. Levenson, "Bulk-to-Surface Precipitation and Surface Diffusion of Carbon on Polycrystalline Nickel," *Surf. Sci.*, **59** [2] 447-60 (1976).

60. R.T.K. Baker, M.A. Barber, P.S. Harris, F.S. Feates, and R.J. Waite, "Nucleation and Growth of Carbon Deposits from the Nickel Catalyzed Decomposition of Acetylene," *J. Catal.*, **26** [1] 51-62 (1972).
61. A. Oberlin, M. Endo, and T. Koyama, "Filamentous Growth of Carbon through Benzene Decomposition," *J. Cryst. Growth*, **32** [3] 335-49 (1976).
62. S. Hofmann, C. Ducati, J. Robertson, and B. Kleinsorge, "Low-Temperature Growth of Carbon Nanotubes by Plasma-Enhanced Chemical Vapor Deposition," *Appl. Phys. Lett.*, **83** [1] 135-37 (2003).
63. E. Fitzer, K. Mueller, and W. Schaefer, "The Chemistry of the Pyrolytic Conversion of Organic Compounds to Carbon," pp. 237-383 in *Chemistry and Physics of Carbon*, Vol. 7. Edited by P. L. Walker. Dekker, New York, 1971.
64. H.M. Cheng, F. Li, G. Su, H.Y. Pan, L.L. He, X. Sun, and M.S. Dresselhaus, "Large-Scale and Low-Cost Synthesis of Single-Walled Carbon Nanotubes by the Catalytic Pyrolysis of Hydrocarbons," *Appl. Phys. Lett.*, **72** [25] 3282-84 (1998).
65. S. Maruyama, Y. Miyauchi, T. Edamura, Y. Igarashi, S. Chiashi, and Y. Murakami, "Synthesis of Single-Walled Carbon Nanotubes with Narrow Diameter-Distribution from Fullerene," *Chem. Phys. Lett.*, **375** [5-6] 553-59 (2003).
66. K.C. Hou and H.B. Palmer, "The Kinetics of Thermal Decomposition of Benzene in a Flow System," *J. Phys. Chem.*, **69** [3] 863-68 (1965).
67. P.E. Nolan, M.J. Schabel, D.C. Lynch, and A.H. Cutler, "Hydrogen Control of Carbon Deposit Morphology," *Carbon*, **33** [1] 79-85 (1995).
68. P.E. Nolan, D.C. Lynch, and A.H. Cutler, "Carbon Deposition and Hydrocarbon Formation on Group VIII Metal Catalysts " *J. Phys. Chem. B*, **102** [21] 4165-75 (1998).
69. P.W. May, "CVD Diamond: A New Technology for the Future?," *Endeavor* **19** [3] 101-06 (1995).
70. Y. Li, W. Kim, Y. Zhang, M. Rolandi, D. Wang, and D. H., "Growth of Single-Walled Carbon Nanotubes from Discrete Catalytic Nanoparticles of Various Sizes," *J. Phys. Chem. B*, **105** [46] 11424-31 (2001).
71. S. Marinkovic, "Substitutional Solid Solubility in Carbon and Graphite," pp. 1-64 in *Chemistry and Physics of Carbon*, Vol. 19. Edited by P. A. Thrower. Dekker, New York, 1989.

72. P. Redlich, J. Loeffler, P.M. Ajayan, J. Bill, F. Aldinger, and M. Ruhle, "B-C-N Nanotubes and Boron Doping of Carbon Nanotubes," *Chem. Phys. Lett.*, **260** [3-4] 465-70 (1996).

5 The Chemistry of Boron-doped Carbon Nanotubes and Nanofibers

5.1 Introduction

It is well established that the presence of boron in carbon materials, including bulk graphite, carbon fibers, and carbon/carbon composites, effectively inhibits the oxidation reaction.¹⁻⁵ Allardice and Walker¹ report that substitutional boron in natural graphite decreases the oxidation rate in both dry and moist oxygen at 600°C. Jones and Thrower^{2,3} study the effect of substitutional boron on the oxidation properties of doped carbon fibers. The degree of carbon oxidation inhibition is dependent on the concentration of boron in the fiber. McKee⁵ investigates the oxidation behavior of two-dimensional carbon/carbon composites coated with glassy borate and report a significant reduction in the oxidation rate in dry or moist air at temperatures up to 1000°C. Kowbel *et al.*⁴ study the effect of boron ion implantation on the oxidation behavior of three-dimensional carbon/carbon composites. At least three possible mechanisms for boron inhibition have been proposed:^{1-4,6} (1) catalytic graphitization of the carbon structure, (2) specific site blockage by the formation of boron oxide, and (3) the electron transfer theory in which boron, as an electron acceptor, lowers the Fermi level of the graphite host material.

The influence of boron on carbon materials becomes more profound as the boron content increases. Soule's study shows that substitutional boron (from ~1ppm to 0.5 at.%) decreases the Fermi level of the host single crystal graphite.⁷ Howe and Jones⁶ propose

that 0.1% B is the threshold concentration at which the electronic, chemical, and structural behavior would be modified. Lowell has determined that the possible maximum boron concentration by a solid state diffusion process is 2.35 at.%.⁸ This could be argued to be the limit of the extent to which properties can be modified. There is a great interest in increasing the substitutional boron concentration in carbon to further enhance the oxidation resistance and modify the electronic behavior of carbon materials.

In the mid 1980s at the University of California-Berkeley, a boron-rich carbon material BC_x with 25 at.% boron was first produced via a chemical vapor deposition (CVD) process using C_6H_6 and BCl_3 at 800°C at atmospheric pressure.^{9,10} The chemical composition of the CVD product was established by combustion in fluorine yielding BF_3 and CF_4 . The relative ratio of these gases was determined by IR absorption spectrometry, which indicated a C/B ratio of 1/3.⁹ This ratio of C/B was also supported via electron energy loss spectra (EELS).¹¹ Compared to solid state doping, producing boron-doped graphite structure by the CVD process has two distinct advantages: a much higher substitutional boron content is possible at a lower processing temperature. Since then, the CVD process to synthesize boron-rich carbon film has been widely studied.¹²⁻¹⁶ The stoichiometry of the deposited products reported varies from 5-25 at.% boron, depending on the experimental conditions used.

The possibility of substitutional doping boron into carbon nanotubes has been investigated in order to tailor the electronic structure of the host nanotubes.¹⁷⁻¹⁹ There are two major methods to achieve boron-doped carbon nanotubes: substitution reaction or

direct synthesis. The substitution reactions undertaken to date involve solid-state diffusion, using either single-walled or multi-walled carbon nanotubes along with boron-containing compounds, such as B_2O_3 . The boron concentrations are reported to be ~ 10 at.% by Han *et al.*²⁰ and Golberg *et al.*,²¹ and 10-15 at.% by Borowiak-Palen *et al.*,^{22,23} respectively. This level of boron concentration is much higher than that of the boron-doped graphite obtained via solid-state diffusion and closer to the boron concentration levels reported in the BC_x thin films of Hach *et al.*¹⁴ There are three direct synthesis methods including arc-discharge, laser ablation, and CVD. Both boron-doped single-walled carbon nanotubes (SWCNTs) and multi-walled carbon nanotubes (MWCNTs) have been produced via direct synthesis. McGuire *et al.*¹⁹ synthesized boron-doped SWCNTs containing up to 3 at.% boron via laser ablation. Redlich *et al.*²⁴ produced boron-doped MWCNTs having 1-5 at.% boron using arc-discharge synthesis. Satishkumar *et al.*²⁵ obtained boron-doped MWCNTs having ~ 3 at.% boron via the pyrolysis of C_2H_2 - B_2H_6 mixtures. Chen *et al.*²⁶ prepared boron-doped carbon nanotubes via a microwave plasma CVD using $B(OCH_3)_3$ as the doping source. There was no boron concentration reported from this work.

Among these three direct synthesis methods, CVD is the most straightforward way to scale up production to industry level. Recently, there is growing interest in producing boron-doped carbon nanotubes and nanofibers via CVD. Schouler *et al.*²⁷ attempted to obtain tubular C_xB ($x \geq 3$) filaments via atmospheric pressure CVD using benzene, BCl_3 and H_2 gas with nickel powder as a catalyst. Instead of a tubular structure, the resulting filaments had whisker-like shapes and a composition of 50-70 at.% B as determined by

EELS. Using a similar CVD process, Koh and Nakajima²⁸ obtained boron-substituted carbon filaments, C_xB , having C/B ratios from 4 to 58. These researchers found that the boron composition decreased as the deposition temperature was increased from 800° to 1100°C. All the previous studies show that by CVD method it is possible to produce boron-doped carbon with high boron concentration (≥ 10 at.%) in the form of nanotubes and nanofibers.

Based on the earlier work done on C_xB film in our lab,¹⁴ the catalytic CVD process is used to produce boron-doped carbon nanotubes and nanofibers having high boron concentrations. We obtained the deposits in the form of nanotubes and nanofibers having a boron concentration up to 18 at.%. The objective of the present work is to study the boron content as a function of the synthesis conditions and to identify the chemical environments of boron in carbon. Since the products are nano-scale material, X-ray photoelectron spectroscopy (XPS) and Auger electron spectroscopy (AES) are employed to ascertain the chemical states of boron and carbon in the boron-doped carbon nanofibers.

5.2 Background

5.2.1 XPS Studies on Boron-Carbon Materials

XPS is one of the few techniques that can be used to identify the local chemical environment of boron in carbon. Previous studies investigating boron-carbon materials by means of XPS revealed that both B_{1s} and C_{1s} spectra include several different chemical environments. Table 5.1 is a summary of the literature assignments for the components of the B_{1s} and C_{1s} spectra on boron-carbon materials. The boron-carbon materials include elemental boron, pure graphite, B_4C , and boron-doped sp^2 carbon (up to ~30 at.% B) in both film and filament form.

The survey given in Table 5.1 is summarized below.

1. In the B_{1s} spectra, the oxide-related species are observed above 189.5 eV, and the possible bindings are BC_2O , BCO_2 , and B_2O_3 . Both B-C and B-B peaks are identified in the 186-189 eV binding energy region. B-C peaks have two possible environments: the B_4C state and the graphitic state (a bond where boron atoms substitute for the graphitic carbon atoms).
2. In the C_{1s} spectra, the oxides occur at high binding energies above ~285 eV. C-B bonds, both in the B_4C state and the graphitic state, are identified in the 282-283.5 eV region. C-C bonds are observed in ~284-285 eV. There is a small drop (~0.5 eV) in the C-C binding energy in B-doped carbon material compared to that of undoped graphite because boron doping decreases the Fermi level of the host carbon.

Table 5.1 Summary of the Literature Assignments for the Components of the B_{1s} and C_{1s} XPS Spectra

Materials	Refs.	B _{1s} (eV)			C _{1s} (eV)		
		B-C	B-B	Oxide-related	C-B	C-C	Oxide-related
B ₄ C crystal	29	B ₄ C 188.0		BC ₂ O 189.7 BCO ₂ 191.4 B ₂ O ₃ 192.9	B ₄ C “sp ³ -like hybridized” 283.7 B ₄ C “sp ² -like hybridized” 281.8	Graphite 284.5	
B ₄ C thin film	30	B ₄ C 188.4		192.0 , 193.2	B ₄ C 282.5	Polymeric 284.7	C-O 285.7, 287.1 C=O 288.5
B ₄ C coatings	31	B ₄ C 188.4		191.4	B ₄ C 283.5	Aliphatic 284.5	286-288
B ₄ C thin film	32	B ₄ C 186.5	Elemental B 188		B ₄ C 283	284.5	
B ₄ C thin film	33	B ₄ C 188.4	pure B film 187.9	> 190	B ₄ C 282.5 C bonded to one/two B 284.0	Amorphous C 284.9	
B ₄ C film	34	B ₄ C 188.6			B ₄ C 282.8		oxy-boron carbide 283.8
B _x C _{1-x} films (0-15% B)	16	B ₄ C 187.5 graphitic 188.5		BC ₂ O 190.5 BCO ₂ 192.0 B ₂ O ₃ 193.2			
B-containing pyrocarbon (up to 33%B)	35	B ₄ C 187.8 graphitic 188.8	Elemental B 187.0	BC ₂ O 190.0 BCO ₂ 192.0 B ₂ O ₃ 193.2	B ₄ C 282.6	sp ² graphitic 284.0	
BC compounds (3-19% B)	36	B substitute graphitic C 187.6, 188.7	B-B in-plane 186.5	>189.5		sp ² graphitic 284.2	
B-doped C films (6-23% B)	37	B substitute graphitic C 188.1			C-B 282.6	sp ² graphitic 283.8	
BC _x filaments (up to 20%B)	28	B-B-C ₂ in plane 188.6		BC ₂ O 190.6 BCO ₂ 192.7	C-B 283.0	sp ² graphitic 284.0	285.5, 288.5

5.2.2 AES Studies on Boron-Carbon Materials

AES employs electron irradiation in order to produce Auger emissions with electron beams that can focus to a very small diameter. The spatial resolution for chemical surface analysis of an Auger microprobe may be as small as 2 nm in diameter.³⁸ AES is highly sensitive to light elements ($Z \geq 3$), and can be used to detect concentrations as low as 0.1 at.% of an element. Combined with scanning electronics for imaging, AES is an ideal tool to identify compositional variations and local electronic structures of nano-scale materials.

A change in chemical bonding results in a change in the wavefunction of the valence electron states involved. The shape of the Auger line, when the Auger transition involves valence band electrons, reveals this wavefunction change. Previous AES results have shown that the boron line shapes do not change appreciably when going from elemental B to B_4C .^{39,40} On the other hand, carbon line shapes change appreciably with changes in carbon hybridization.⁴¹ A comparison of the fine structures of the carbon Auger line shapes from diamond, graphite, and amorphous carbon is given in Figure 5.1.⁴² The manifest differences between the carbon Auger spectra for diamond and graphite have been reported to be a consequence of the different valence density states of diamond (sp^3 -hybridized with only σ states) and graphite (sp^2 -hybridized with both σ and π states).⁴³ In the amorphous carbon Auger signal, there is a loss of fine structure at ~ 258 eV, which corresponds to a “smearing-out” of the valence band structure. AES spectra from carbides yield the characteristic triplet of ‘carbide carbon’ line shape; thus differences between graphitic and carbide line shapes can be clearly distinguished.^{38,44}

However, the shapes of both boron and carbon lines are not dependent on the stoichiometry of the boron carbide samples (B_9C to B_4C).⁴⁰

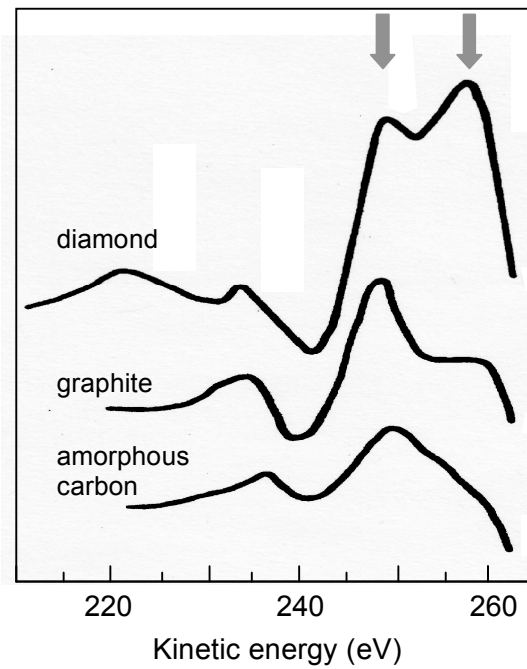


Figure 5.1. Fine structures of the carbon Auger spectra from diamond, graphite, and amorphous carbon.⁴² The main peaks have been aligned with the diamond main peak position at 268 eV. This graph shows evolutions of the two shoulder positions at ~248 eV and ~258 eV for all three carbon materials.

5.3 Experimental Procedures

5.3.1 Synthesis of Carbon and Boron-doped Carbon Nanofibers

The synthesis of carbon and boron-doped carbon samples was carried out in a flow system. The materials were deposited on fused quartz substrates coated with a pure nickel film, 3-5 nm thick. The nickel film was coated using a high vacuum thermal evaporator. The reactor included a fused quartz tube in a horizontal tube furnace. The substrates were placed in the 10 cm long central isothermal zone of the reactor. BCl_3 and C_6H_6 were used as reactants. The BCl_3 flow rate was controlled by a mass flow controller, and C_6H_6 vapor was introduced into the reactor by means of hydrogen gas. The flow rate of C_6H_6 was calculated according to its partial pressure in the saturator maintained in an isothermal water bath at the applied hydrogen flow rate. Results show that the deposition temperature and the partial pressure ratio $\text{BCl}_3/\text{C}_6\text{H}_6$ are two factors that appreciably influence the structure and boron content of the resulting deposits. Therefore, further experiments were carried out under temperatures between 750°C and 900°C and partial pressure ratio $\text{BCl}_3/\text{C}_6\text{H}_6$ of 2, 1, and 0.5. After deposition, all samples were annealed at 900°C for 20 hours under 93.5kPa UHP He.

5.3.2 XPS and AES

XPS was undertaken using a PHI Quantera Scanning X-ray Microprobe with $\text{Al K}\alpha$ (1486.4 eV) X-ray irradiation under high vacuum (10^{-9} Torr). Sputter-cleaning of the sample surface was achieved by a 4-kV Ar^+ beam. Boron powder (Alfa Aesar, 99.99% metals basis), B_4C powder (Alfa Aesar, 99+% metals basis), and HOPG (SPI Supplies,

>99.99%) were used as reference materials for the binding energy of the C1s and B1s peaks. The atomic concentration of element X is given by:

$$\%X = 100\% \times [(I_x / S_x) / \Sigma(I_i / S_i)] \quad (5.1)$$

where I_x is the measured intensity of photoelectron peaks and S_x is the corrected sensitivity factor for the element X peak calculated by MultiPak software from ULVac-PHI Inc.

The Auger analysis was carried out using a Schottky field emission gun PHI 680 Scanning Auger Nanoprobe (SAN), equipped with a cylindrical mirror analyzer (CMA). The accelerating voltage of the incident electron beam was 3 kV with a current of 10 nA. The samples were transferred to the vacuum chamber (3×10^{-10} Torr) and then sputtered using a 3.5-kV Ar^+ beam to remove surface species. The boron and carbon KLL Auger electron intensities were measured, and the samples were further sputtered until Auger signals were independent of sputter time. The bulk B_4C powder (assuming it is stoichiometric) was used as a standard sample, to obtain the related sensitivity factors and thereby determine the compositions of the samples.⁴⁵ The systematic error in the reported compositions is estimated to be less than 10%.

5.4 Results and Discussion

5.4.1 Chemical Compositions of Boron-doped Carbon Nanofibers

The chemical compositions of boron-doped carbon nanofibers determined by XPS and AES analysis, as well as the deposition reaction parameters, are listed in Table 5.2. Group I samples are produced by changing the partial pressure ratio $\text{BCl}_3/\text{C}_6\text{H}_6$ from 0.5 to 2, and samples of Group II are produced by changing the deposition temperature from 750°C to 900°C . All the boron-doped nanofiber samples consist of boron, carbon, and oxygen. Boron to carbon ratios, B/C, are similar in data obtained both by XPS and AES. Table 5.2 shows that boron concentrations in the products strongly depend on applied reaction parameters, i.e., deposition temperature and partial pressure ratios of $\text{BCl}_3/\text{C}_6\text{H}_6$. Boron concentrations of nanofibers increase with an increase in the partial pressure ratio of $\text{BCl}_3/\text{C}_6\text{H}_6$. Nanofibers having the highest boron concentration (18.4 at.%B by AES) are obtained using $\text{BCl}_3/\text{C}_6\text{H}_6=2$ deposited at 800°C for 30min. Boron concentrations of nanofibers as a function of deposition temperature are given in Figure 5.2. Boron concentrations of nanofibers reach a maximum value at 800°C , and then decrease with increasing deposition temperature from 800°C to 900°C . The optimum temperature to obtain a high boron content sample is $\sim 800^\circ\text{C}$.

Nakajima and Koh^{28,46} studied the synthesis of nitrogen-doped and boron-doped carbon systems, C_xN and BC_x , by CVD using a nickel catalyst at $800\text{-}1200^\circ\text{C}$. A relationship between nitrogen concentration and deposition temperature was reported in that nitrogen content reaches its highest level around 900°C , then drops with increasing deposition temperature. In their study of BC_x filaments,²⁸ Nakajima and Koh also found that

Table 5.2 Chemical Compositions of Boron-doped Carbon Nanofibers by XPS and AES Analysis

Sample No.	Material	Deposition Temp. & Time	Flow rate and Partial Pressure		XPS Analysis				AES Analysis				
			Total flow Total pressure	$\text{BCl}_3:\text{C}_6\text{H}_6 : \text{H}_2$	B at. %	C at. %	O at. %	B/C ratio	B at. %	C at. %	O at. %	B/C ratio	B/O ratio
I-1	C_xB nanofibers	800°C 30min	65 cc/min 93.5 kPa	10: 10: 45	10.7	86.1	3.2	0.12	13.3	84.6	2.1	0.16	6.3
I-2	C_xB nanofibers	800°C 30min	65 cc/min 93.5 kPa	10: 5: 50	14.8	80.2	5.0	0.19	18.4	78.5	3.1	0.22	5.9
I-0.5	C_xB nanofibers	800°C 30min	65 cc/min 93.5 kPa	10: 20: 35	10.3	86.8	2.9	0.12	10.1	88.6	1.2	0.11	8.4
II-750C	C_xB nanofibers	750°C 30min	60 cc/min 93.5 kPa	10: 17: 33	3.2	95.7	1.1	0.03	6.3	92.2	1.5	0.07	4.2
II-800C	C_xB nanofibers	800°C 30min	60 cc/min 93.5 kPa	10: 17: 33	7.5	90.9	1.3	0.08	11.3	87.7	1.0	0.13	11.3
II-850C	C_xB nanofibers	850°C 30min	60 cc/min 93.5 kPa	10: 17: 33	6.3	93.0	0.7	0.07	8.4	91.0	0.6	0.09	14
II-900C	C_xB nanofibers	900°C 30min	60 cc/min 93.5 kPa	10: 17: 33	4.8	94.7	0.5	0.05	4.8	94.9	0.3	0.05	16
A*	C_xB film	750°C 8h	35 cc/min 93.5 kPa	4: 4: (He) 27	7.7	91.4	0.9	0.08	11.2	87.0	1.8	0.13	6.2
B*	Carbon nanofibers	800°C 30min	65 cc/min 93.5 kPa	0: 10: 55	--	97.5	2.5	--	--	97.2	2.8	--	--

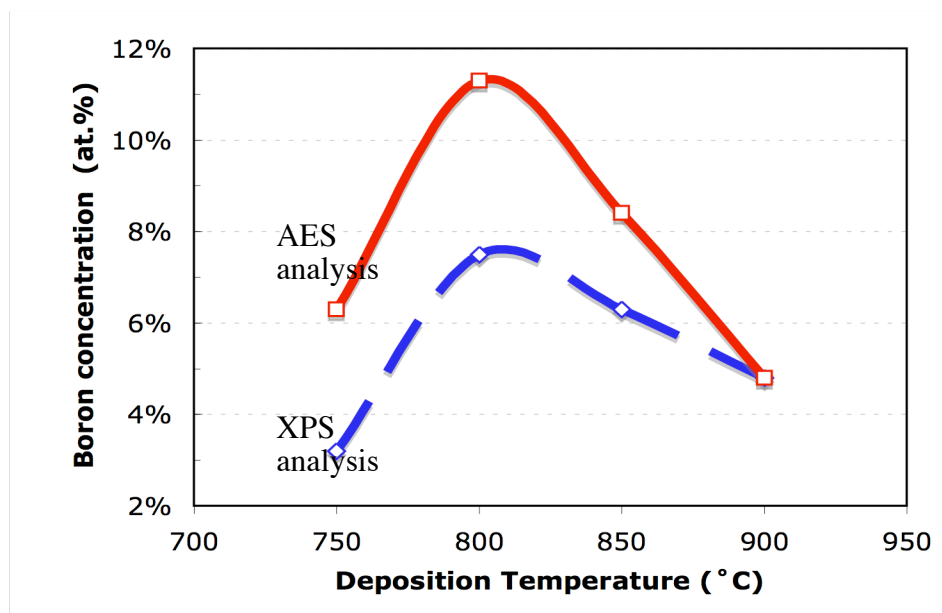


Figure 5.2. Boron concentration of nanofibers of Group II as a function of the deposition temperature.

boron concentration decreased with an increase in the deposition temperature from 800° to 1100°C. The researchers explained that the difference in bonding lengths between C-C and C-B or C-N would cause an in-plane structure strain that would be diminished by temperature rise because of the release of boron or nitrogen atoms. However, the reason that nitrogen concentration increases with increasing deposition temperature from 800-900°C was not revealed in their study.

In the structure study on boron-doped nanofibers, we found that the nano-structure of samples deposited at 750°C is different from the structure of samples deposited at temperatures higher than 800°C. Figure 5.3 shows the structures of samples deposited at 750°C and 800°C. The nanofibers deposited at 750°C have a core of platelet stacking

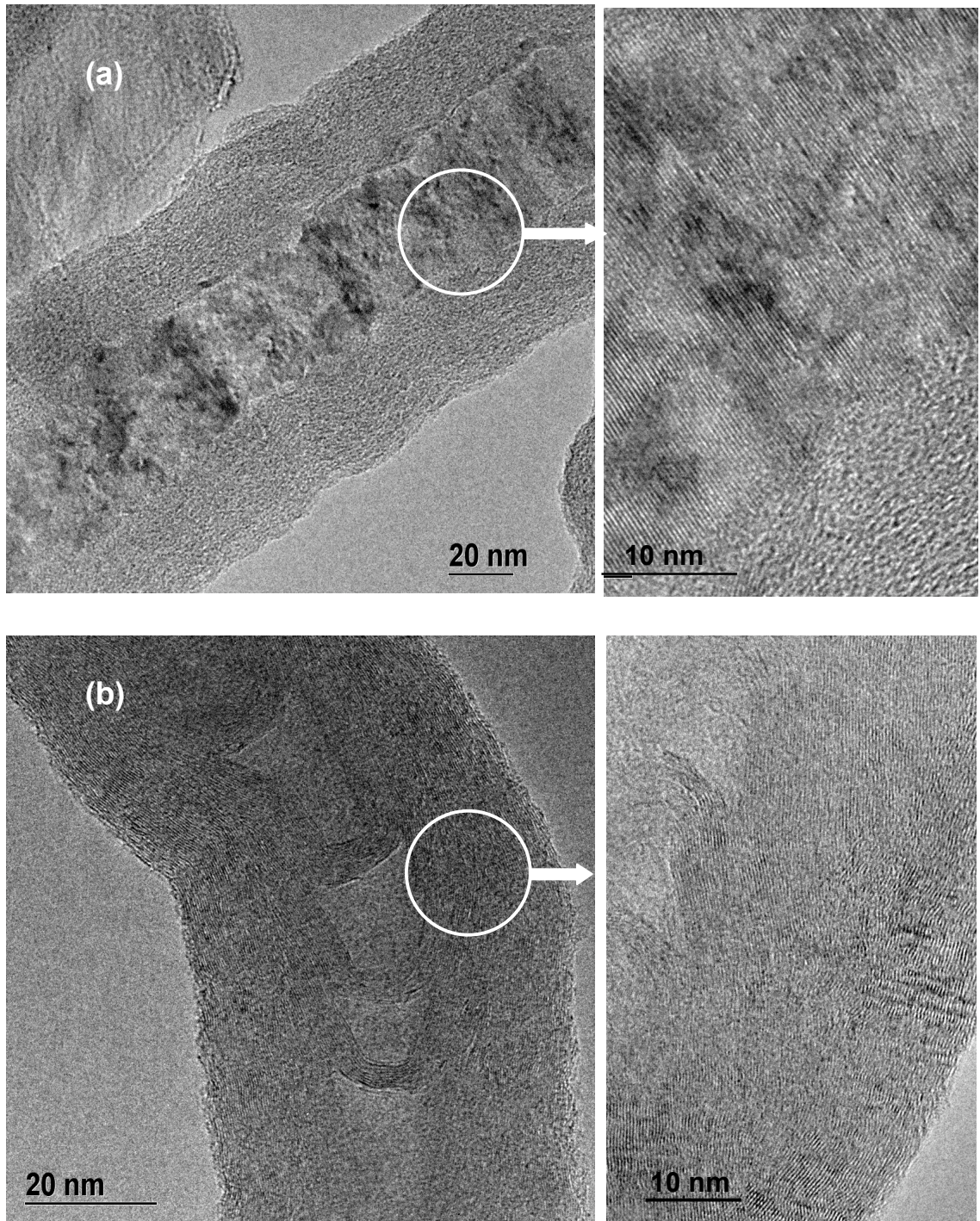


Figure 5.3. High-resolution TEM images of platelet and herringbone or tubular nanofibers. (a) A nanofiber having a platelet stacked core and 6 at.% boron ($\text{BCl}_3/\text{C}_6\text{H}_6$ -10/17, 750°C). (b) A nanofiber having a herringbone core and 10 at.% boron ($\text{BCl}_3/\text{C}_6\text{H}_6$ -10/20, 800°C).

with an interlayer spacing of 3.35 Å, the same as that of perfect graphite structure. The nanofibers deposited at 800°C have a core of herringbone stacking with an interlayer spacing of 3.37 Å. As shown in Figure 5.3 (a), the platelet stacked carbon is of a significantly higher order, similar to perfect graphite stacking. These results show that a high content of any impurity should not be included in the platelet carbon structure via a non-equilibrium reaction growth. Studies of catalytic carbon nanofiber growth reveal that low temperatures favor the growth of platelet stacking while high temperatures favor tubular stacking.⁴⁷ These stacking types are correlated with the nature of the catalyst particles, such as their softening temperature and surface free energy. Further discussion of the growth mechanism of boron-doped nanofibers and the correlation thereon with the stacking type as a function of the nature of the catalyst particles follows in Chapter 6. The change in boron concentration at low temperatures is also related to the stacking structure of the nanofibers.

Our experiments show a slight discrepancy in the data obtained by XPS and AES. The boron concentrations are 2-4 at.% higher and the oxygen concentrations are 1-2 at.% lower as detected by AES than those values detected by XPS. The analytical volume of the two techniques can explain this difference. XPS and AES are both surface chemistry analysis techniques with a sampling depth in the same range of 5-50 Å. The electron beam size of the Auger microprobe can be less than 10 nm, whereas the minimum X-ray beam size of the XPS is 9 μm.⁴⁸ The diameters of the nanofiber samples observed under the microscope are in the range of 50-300 nm. Thus, the Auger microprobe can easily be focused on a single nanofiber, while detection by XPS contains

information from the surface species over a much broader area. A later study on atom distribution suggests that boron concentration on the surface is lower than that in the core. Therefore, we conclude that AES data are the most representative of the actual specimen compositions.

The relative oxygen contents as detected by both XPS and AES are similar, in the range of 0.3-5.0 at.%. In order to clarify the relationship between boron content and oxygen content, B/O atom ratios in the samples as measured by AES are listed in Table 5.3. B/O ratios change little with variations of reactant ratios of $\text{BCl}_3/\text{C}_6\text{H}_6$, but increase significantly with a rise in deposition temperatures between 750°C and 900°C . At high temperatures, boron atoms are free from oxygen, i.e. more than 95% boron atoms would not bond with oxygen atoms. It indicates that oxygen atoms are physisorbed in the samples. Bonding information will be discussed in the following section where the peak positions of carbon and boron XPS peaks and carbon and boron Auger line shapes will be examined.

Oxygen content is introduced into the system in two ways. First, when the samples are exposed to air, oxygen reacts with the boron species existing at the edge of the graphene layer, which explains why oxygen exists mostly on the surfaces of the samples. Second, oxygen may have originated from the fused quartz substrates. No silicon signal is detected by either AES or XPS, but it is detected using high resolution TEM/EDS. Table 5.3 shows the atom ratios determined by high resolution TEM/EDS in boron-doped carbon nanofibers. The samples have a small concentration of silicon, with ratios less

than 0.06 Si/C. The atom ratios are detected in a different morphology, i.e., the tip or the stem on a nanofiber. Si/C ratios are higher at the tip of the nanofibers than the ratios detected at the stem. O/Si ratios are lower than 2 (note that O/Si in quartz is 2) at the tip of the nanofibers, but higher than 2 at the stem. These results enable us to speculate that the quartz substrate (SiO₂) participates in the reaction when the nanofibers originate on the substrate surface; thus, a very small partial pressure of oxygen is evolved around the substrate surface area as a result of the non-equilibrium reaction between BCl₃, H₂ and quartz.

Table 5.3 Atom Ratios of Boron-doped Nanofibers by AES and TEM/EDS Analysis

Sample	AES Analysis		TEM-EDS Analysis	
	B/C ratio	B/O ratio	Si/C ratio	O/Si ratio
I-1	0.16	6.3	tip: .01- .04 stem: < .01	tip: 1.2 - 2.3 stem: 3-10
I-2	0.22	5.9	N/A	N/A
I-0.5	0.11	8.4	N/A	N/A
II-750C	0.07	5.2	.01- .02	tip: 1.8 stem: 3.4-5.7
II-800C	0.13	11.3	tip: .03- .06 stem: ≤ .01	tip: 0.9-2.0 stem: 4.9-8.7
II-850C	0.09	14	tip: .01- .04 stem: < .01	tip: 2.3-3.6 stem: 4.8-6.2
II-900C	0.05	16	tip: .03- .05	tip: 1.0-3.3
Pure C nanofibers	N/A	N/A	< .01	2.9-3.4

5.4.2 Chemical State of B and C in Boron-doped Carbon Nanofibers

The C1s and B1s XPS spectra of boron-doped carbon nanofibers are shown in Figure 5.4 and Figure 5.5. These spectra were taken after sputter-cleaning the sample surface. In the C1s spectra, the binding energies for the boron-doped carbon nanofibers are in the range of 283.2-283.8 eV. Pyrolytic carbon and B₄C are used as references. The C1s binding energies of pyrolytic carbon and B₄C are 284.6 eV and 282.8 eV, respectively. The peak positions and line shapes of the samples are independent of the deposition parameters, i.e., reactant ratios and deposition temperatures. Compared to the reference materials, the peak shapes and the full-width half-maximum (FWHM) of the C1s peaks from the boron-doped carbon nanofibers are similar to the peaks from the pyrolytic carbon. However, the peak positions of all samples are 0.8-1.4 eV lower than the peak position of the graphite. Boron atoms incorporated in graphite would be expected to lower the Fermi level of the host material because of the electron deficiency of the boron atom.⁷ As predicted, a downshift of the carbon binding energies is observed in the C1s spectra.

In the B1s spectra, binding energies from the boron-doped carbon are in the range of 187.7-188.3 eV, and those from amorphous boron and B₄C are 187.5 eV and 188.0 eV, respectively. In addition, the peak positions and line shapes are independent of the deposition parameters. The B1s peaks from the samples have long tails at the high energy side that is correlated with the small amount of oxide-related species either on the surface or in the body ($\leq 3\text{at.}\%$ O by AES). Because of the low signal-to-noise ratio in

the B1s spectra due to the low boron concentration (≤ 18 at.% B), it is difficult to analyze the line shapes and the slight peak shift from the boron-doped nanofibers.

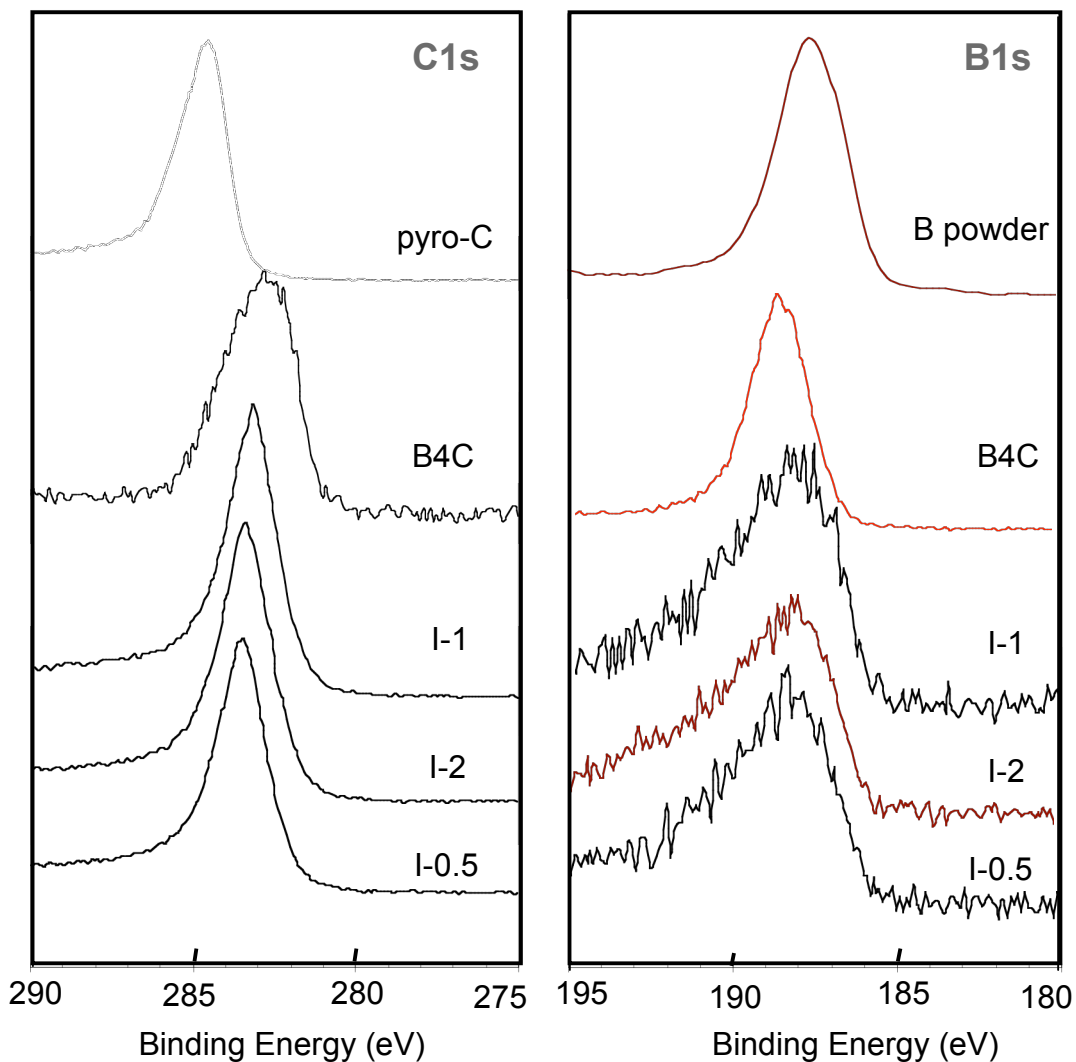


Figure 5.4. The C1s and B1s XPS spectra of boron-doped carbon nanofibers deposited at reactant partial pressure ratios of $\text{BCl}_3/\text{C}_6\text{H}_6$ between 0.5 and 2. Pyrolytic carbon, amorphous boron, and B_4C are used as the reference materials.

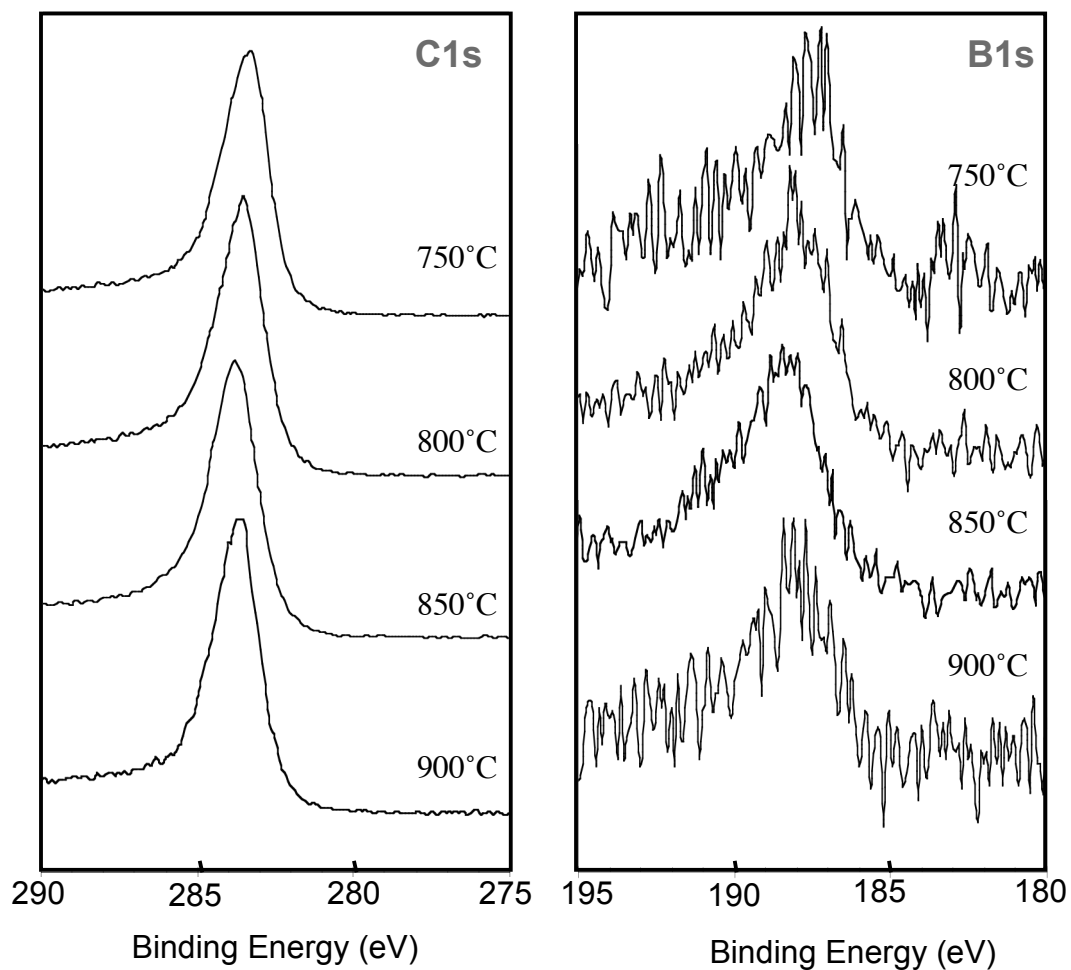


Figure 5.5 The C1s and B1s XPS spectra of boron-doped carbon nanofibers deposited at temperatures between 750°C and 900°C.

The C *KVV* and B *KVV* Auger spectra of boron-doped carbon nanofibers are given in Figure 5.6 and Figure 5.7. Qualitative information about the bonding of the carbon atoms in the samples is achieved by analysis of line shapes of the C *KVV* Auger transition. The carbon spectrum from B₄C has the characteristic triplet of a ‘carbide carbon’ line shape. The carbon atoms in B₄C are sp³ hybridized; thus a high shoulder appears at 264 eV, similar to the C *KVV* Auger spectra from diamond.⁴² The carbon spectrum from pure carbon nanofibers has a low shoulder at 264 eV, corresponding to the graphitic (sp² hybridized) carbon atoms. Comparison of the two shoulder positions at ~253 eV and ~264 eV reveals that the carbon line shapes of boron-doped carbon nanofibers are similar to the line shape of graphitic (sp²) carbon. The line shapes of C *KVV* Auger spectra from all samples are similar with no dependence on the chemical composition. Clearly, carbon atoms in the boron-doped nanofibers are sp² hybridized in both C-C and C-B bonds.

In the B *KVV* spectra, the main peaks from Group I samples deposited at a reactant ratio (BCl₃/C₆H₆) from 0.5 to 2 are at the same position, i.e., ~182 eV, similar to the boron peak position of B₄C. However, the B *KVV* line shapes from Group II samples deposited at temperatures from 750 to 900°C show a dependence on the deposition temperatures. With increasing deposition temperature, the peak around 182 eV of the sample deposited at 750°C splits into two peaks at 180 eV and 186 eV, and the relative intensity between the two peaks also changes. There is very little literature addressing the B *KVV* line shapes, so it is difficult to explain the evolution of the B *KVV* spectra caused by the increase in deposition temperatures.

The bonding of boron atoms in the samples may be deduced by reviewing the bonding information derived from the C1s and B1s XPS spectra and the C *KVV* Auger line shapes. First, B-C bonding in B₄C state can be excluded because there is no characteristic triplet of ‘carbide carbon’ line shape in the C *KVV* Auger spectra; thus, B-C bonding is in an sp² hybridized state. Possible boron sp² hybridized states include B₂-BC, B-BC₂ and BC₃. Among the three structures, B₂-BC bonding is the most unstable because the B-B bonding length is larger than C-C and may easily introduce in-plane strain. The B1s XPS peaks in the range of 187.7-188.3 eV are assigned to the combination of B-BC₂ and BC₃ states. Second, the B-O bonding can be excluded in the boron-doped carbon nanofibers because of the very low oxygen content (≤ 3 at.% O by AES). The B/O atom ratios are given in Table 5.3. For Group II samples, B/O ratios are greater than 10 when the deposition temperature is higher than 800°C. Finally, the third possible state is B-B bonding, indicative of a small boron cluster in the deposit. With an increase in the deposition temperature, boron concentrations in the nanofibers decrease, and the main peak of the B *KVV* Auger spectra (~182 eV) splits into two peaks at 180 eV and 186 eV. Considering that amorphous boron has a B *KVV* peak at the position of 186 eV, as shown in Figure 5.6, we can reasonably assume the peak at 186 eV is a small boron atom cluster, which exists at the edge of the graphene layers or as an interstitial species between the graphene layers. This may contribute to disorder/strain within the nanofiber structure.

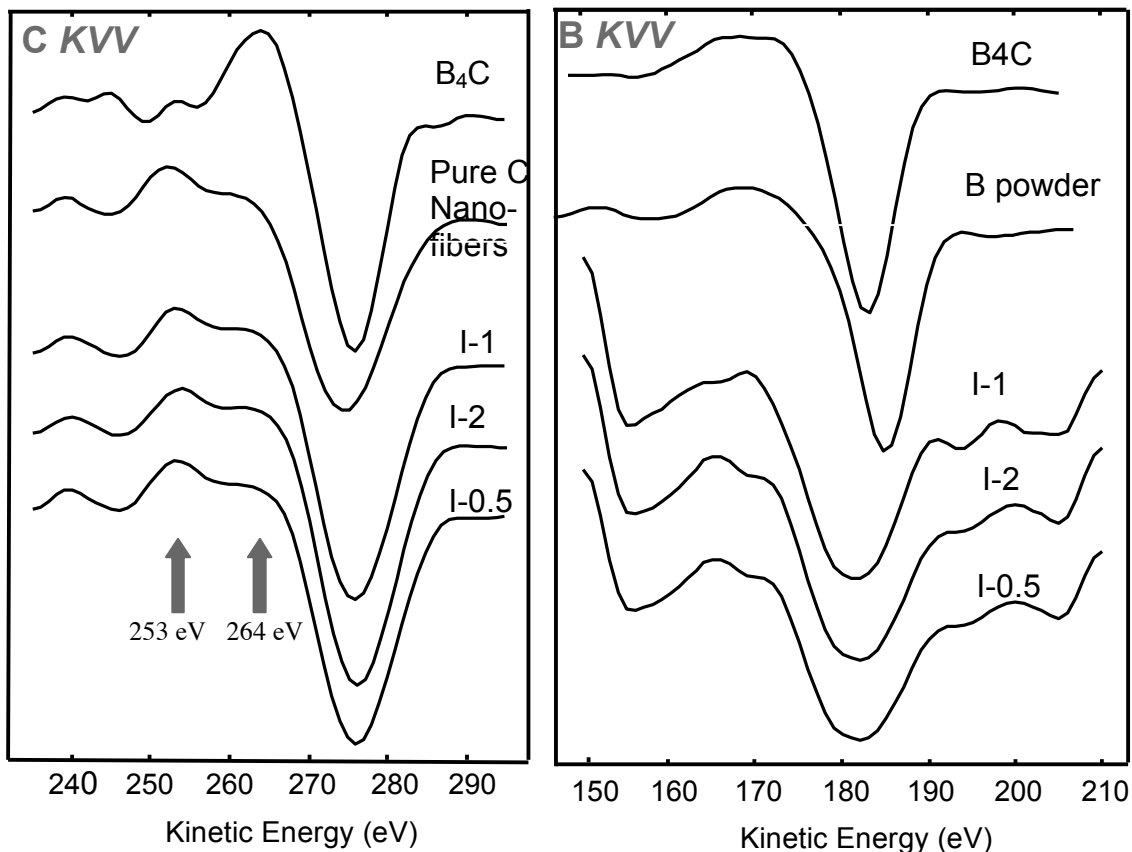


Figure 5.6. The C (KVV) and B (KVV) Auger peaks of boron-doped carbon nanofibers deposited at reactant partial pressure ratio, $\text{BCl}_3/\text{C}_6\text{H}_6$, between 0.5 and 2. Pure carbon nanofibers, amorphous boron, and B_4C are used as the reference materials.

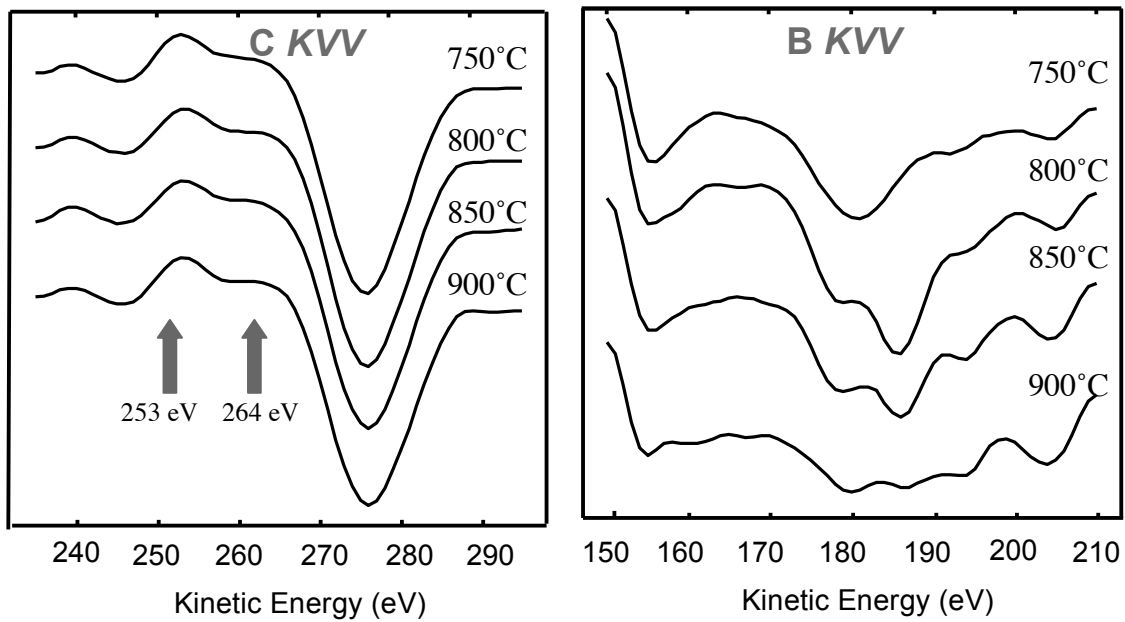


Figure 5.7. The C (KVV) and B (KVV) Auger peaks of boron-doped carbon nanofibers deposited at temperature between 750 and 900°C.

5.5 Conclusions

The boron concentrations of the boron-doped carbon nanotubes and nanofibers are in the range of 5-18 at.%. The boron concentration of the nanofibers deposited at 800°C with reactant ratio $\text{BCl}_3/\text{C}_6\text{H}_6 = 2$ as measured by AES is 18 at.%. Boron content increases with an increase in $\text{BCl}_3/\text{C}_6\text{H}_6$ from 0.5 to 2. Boron content in the deposits reaches a maximum at the deposition temperature of 800°C, and then decreases from 800°C to 900°C. The optimum temperature to obtain a high boron content is around 800°C. XPS and Auger analyses suggest that the C-B bonding is sp^2 hybridized and includes B-BC₂ and B-C₃. The concentration of B-O bonds in the material is very low, and the primary contribution of oxygen arises from physisorbed species. Small clusters of boron atoms may be present in the nanofibers deposited at high temperatures that contribute to disorder/strain within the nanotube and nanofiber structure.

References

1. D.J. Allardice and J.P.L. Walker, "The Effect of Substitutional Boron on the Kinetics of the Carbon-Oxygen Reaction," *Carbon*, **8** [3] 375-85 (1970).
2. L.E. Jones and P.A. Thrower, "The Effect of Boron on Carbon Fiber Microstructure and Reactivity," *J. Chim. Phys.*, **84** [11-12] 1431-38 (1987).
3. L.E. Jones and P.A. Thrower, "Influence of Boron on Carbon Fiber Microstructure, Physical Properties, and Oxidation Behavior," *Carbon*, **29** [2] 251-69 (1991).
4. W. Kowbel, Y. Huang, and H. Tsou, "Effect of Boron Ion Implantation on the Oxidation Behavior of Three-Dimensional Carbon-Carbon Composite," *Carbon*, **31** [2] 355-63 (1993).
5. D.W. McKee, "Oxidation Behavior and Protection of Carbon/Carbon Composites," *Carbon*, **25** [4] 551-57 (1987).
6. J.Y. Howe and L.E. Jones, "Influence of Boron on Structure and Oxidation Behavior of Graphite Fiber, P120," *Carbon*, **42** [3] 461-67 (2004).
7. D.E. Soule, "The Effect of Boron on the Electronic Properties of Graphite," pp. 12-21 in *The 5th Conference on Carbon*, Vol. 1. Pergamon Press, 1962.
8. C.E. Lowell, "Solid Solution of Boron in Graphite," *J. Am. Ceram. Soc.*, **50** [3] 142-44 (1967).
9. J. Kouvetakis, R.B. Kaner, M.L. Sattler, and N. Bartlett, "A Novel Graphite-Like Material of Composition BC_3 , and Nitrogen-Carbon Graphites," *J. Chem. Soc., Chem. Commun.*, **1986** 1758-59 (1986).
10. R.B. Kaner, J. Kouvetakis, C.E. Warble, M.L. Sattler, and N. Bartlett, "Boron-Carbon-Nitrogen Materials of Graphite-Like Structure," *Mater. Res. Bull.*, **22** [3] 399-404 (1987).
11. K.M. Krishnan, "Structure of Newly Synthesized BC_3 Films," *Appl. Phys. Lett.*, **58** [17] 1857-59 (1991).
12. B.M. Way, J.R. Dahn, T. Tiedje, K. Myrtle, and M. Kasrai, "Preparation and Characterization of B_xC_{1-x} Thin Films with the Graphite Structure," *Phys. Rev. B: Condens. Matter Mater. Phys.*, **46** [3] 1697-702 (1992).
13. J. Kouvetakis, M.W. McElfresh, and D.B. Beach, "Chemical Vapor Deposition of Highly Conductive Boron-Doped Graphite from Triphenyl Boron," *Carbon*, **32** [6] 1129-32 (1994).

14. C.T. Hach, L. E. Jones, C. Crossland, and P.A. Throver, "An Investigation of Vapor Deposited Boron Rich Carbon - A Novel Graphite-Like Material - Part I: The Structure of BC_x (C_6B) Thin Films," *Carbon*, **37** [2] 221-30 (1999).
15. D.L. Fecko, L.E. Jones, and P.A. Throver, "The Formation and Oxidation of BC_3 , a New Graphitelike Material," *Carbon*, **31** [4] 637-44 (1993).
16. W. Cermignani, T.E. Paulson, C. Onneby, and C.G. Pantano, "Synthesis and Characterization of Boron-Doped Carbons," *Carbon*, **33** [4] 367-74 (1995).
17. A. Bachtold, P. Hadley, T. Nakanishi, and C. Dekker, "Logic Circuits Based on Carbon Nanotubes," *Phys. E (Amsterdam, Neth.)*, **16** [1] 42-46 (2003).
18. D.L. Carroll, P. Redlich, P.M. Ajayan, S. Curran, S. Roth, and M. Ruhle, "Spatial Variations in the Electronic Structure of Pure and B-Doped Nanotubes," *Carbon*, **36** [5-6] 753-56 (1998).
19. K. McGuire, N. Gothard, P.L. Gai, M.S. Dresselhaus, G. Sumanasekera, and A.M. Rao, "Synthesis and Raman Characterization of Boron-Doped Single-Walled Carbon Nanotubes," *Carbon*, **43** [2] 219-27 (2005).
20. W. Han, Y. Bando, K. Kurashima, and T. Sato, "Boron-Doped Carbon Nanotubes Prepared through a Substitution Reaction," *Chem. Phys. Lett.*, **299** [5] 368-73 (1999).
21. D. Golberg, Y. Bando, L. Bourgeois, K. Kurashima, and T. Sato, "Large-Scale Synthesis and HRTEM Analysis of Single-Walled B- and N-Doped Carbon Nanotube Bundles," *Carbon*, **38** [14] 2017-27 (2000).
22. E. Borowiak-Palen, T. Pichler, G.G. Fuentes, A. Graff, R.J. Kalenczuk, M. Knupfer, and J. Fink, "Efficient Production of B-Substituted Single-Wall Carbon Nanotubes," *Chem. Phys. Lett.*, **378** [5-6] 516-20 (2003).
23. E. Borowiak-Palen, T. Pichler, A. Graff, R.J. Kalenczuk, M. Knupfer, and J. Fink, "Synthesis and Electronic Properties of B-Doped Single Wall Carbon Nanotubes," *Carbon*, **42** [5-6] 1123-26 (2004).
24. P. Redlich, J. Loeffler, P.M. Ajayan, J. Bill, F. Aldinger, and M. Ruhle, "B-C-N Nanotubes and Boron Doping of Carbon Nanotubes," *Chem. Phys. Lett.*, **260** [3-4] 465-70 (1996).
25. B.C. Satishkumar, A. Govindaraj, K.R. Harikumar, J.-P. Zhang, A.K. Cheetham, and C.N.R. Rao, "Boron-Carbon Nanotubes from the Pyrolysis of C_2H_2 - B_2H_6 Mixtures," *Chem. Phys. Lett.*, **300** [3-4] 473-77 (1999).

26. C.F. Chen, C.L. Tsai, and C.L. Lin, "The Characterization of Boron-Doped Carbon Nanotube Arrays," *Diamond Relat. Mater.*, **12** [9] 1500-04 (2003).
27. M.C. Schouler, M.C. Cheynet, K. Sestier, J. Garden, and P. Gadelle, "New Filamentous Deposits in the Boron-Carbon System," *Carbon*, **35** [7] 993-1000 (1997).
28. M. Koh and T. Nakajima, "Synthesis of Well Crystallized Boron-Carbon Filament by Chemical Vapor Deposition Using a Nickel Catalyst," *Carbon*, **36** [7-8] 913-20 (1998).
29. I. Jimenez, D.G.J. Sutherland, T. van Buuren, J.A. Carlisle, L.J. Terminello, and F.J. Himpsel, "Photoemission and X-Ray Absorption Study of Boron Carbide and Its Surface Thermal Stability," *Phys. Rev. B: Condens. Matter Mater. Phys.*, **57** [20] 13167-74 (1998).
30. O. Postel and J. Heberlein, "Deposition of Boron Carbide Thin Film by Supersonic Plasma Jet CVD with Secondary Discharge," *Surf. Coat. Technol.*, **108-109** [1-3] 247-52 (1998).
31. T. Hu, L. Steihl, W. Rafaniello, T. Fawcett, D.D. Hawn, J.G. Mashall, S.J. Rozeveld, C.L. Putzig, J.H. Blackson, W. Cermignani, and M.G. Robinson, "Structures and Properties of Disordered Boron Carbide Coatings Generated by Magnetron Sputtering," *Thin Solid Films*, **332** [1-2] 80-86 (1998).
32. E. Pascual, E. Martinez, J. Esteve, and A. Lousa, "Boron Carbide Thin Films Deposited by Tuned-Substrate RF Magnetron Sputtering," *Diamond Relat. Mater.*, **8** [2-5] 402-05 (1999).
33. C. Ronning, D. Schwen, S. Eyhusen, U. Vetter, and H. Hofsass, "Ion Beam Synthesis of Boron Carbide Thin Films," *Surf. Coat. Technol.*, **158-159** [1] 382-87 (2002).
34. L.G. Jacobsohn, R.K. Schulze, M.E.H. Maia da Costa, and M. Nastasi, "X-Ray Photoelectron Spectroscopy Investigation of Boron Carbide Films Deposited by Sputtering," *Surf. Sci.*, **572** [2-3] 418-24 (2004).
35. S. Jacques, A. Guette, X. Bourrat, F. Langlais, C. Guimon, and C. Labrugere, "LPCVD and Characterization of Boron-Containing Pyrocarbon Materials," *Carbon*, **34** [9] 1135-43 (1996).
36. B. Maquin, A. Derre, C. Labrugere, M. Trinquocoste, P. Chadeyron, and P. Delhaes, "Submicronic Powders Containing Carbon, Boron and Nitrogen: Their Preparation by Chemical Vapour Deposition and Their Characterization," *Carbon*, **38** [1] 145-56 (2000).

37. T. Shirasaki, A. Derre, M. Menetrier, A. Tressaud, and S. Flandrois, "Synthesis and Characterization of Boron-Substituted Carbons," *Carbon*, **38** [10] 1461-67 (2000).
38. I.F. Ferguson, *Auger Microprobe Analysis*; pp. 276-306. Adom Hilger, New York, 1989.
39. G. Hanke and K. Muller, "Low Energy Auger Transition of Boron in Several Boron Compounds," *J. Vac. Sci. Technol., A*, **2** [2] 964-68 (1984).
40. H.H. Madden and G.C. Nelson, "Auger-Electron Spectra from Boron Carbide," *Phys. Rev. B: Condens. Matter Mater. Phys.*, **31** [6] 3667-71 (1985).
41. D.E. Ramaker, "Chemical Effects in the Carbon KVV Auger Line Shapes," *J. Vac. Sci. Technol., A*, **7** [3] 1614-22 (1989).
42. P.G. Lurie and J.M. Wilson, "The Diamond Surface : II. Secondary Electron Emission," *Surf. Sci.*, **65** [2] 476-98 (1977).
43. A.M. Bonnot, "Overview of the Characterization Methods of the Growth Mechanisms of Low Pressure Diamond," *Surf. Coat. Technol.*, **45** [1-3] 343-52 (1991).
44. D.W. Goodman, R.D. Kelley, T.E. Madey, and J.J.T. Yates, "Kinetics of the Hydrogenation of Co over a Single Crystal Nickel Catalyst," *J. Catal.*, **63** [1] 226-34 (1980).
45. K.D. Childs, B.A. Carlson, L.A. LaVanier, J.F. Moulder, D.F. Paul, W.F. Stickle, and D.G. Watson, *Handbook of Auger Electron Spectroscopy*, 3rd ed.; pp. 12-17. Physical Electronics, Eden Prairie, MN, 1995.
46. T. Nakajima and M. Koh, "Synthesis of High Crystalline Carbon-Nitrogen Layered Compounds by CVD Using Nickel and Cobalt Catalysts," *Carbon*, **35** [2] 203-08 (1997).
47. A. Tanaka, S.-H. Yoon, and I. Mochida, "Preparation of Highly Crystalline Nanofibers on Fe and Fe-Ni Catalysts with a Variety of Graphene Plane Alignments," *Carbon*, **42** [3] 591-97 (2004).
48. "PHI Quantera XPS Microprobe" (2006) Physical Electronics, Inc. Accessed on: November, 2006. Available at <<http://www.PHI.com/genf.asp?ID=724>>

6 Structure and Structure-related Chemistry of Boron-doped Carbon Nanotubes and Nanofibers

6.1 Introduction

Carbon nanotubes and nanofibers are graphitic filaments with diameters in the range of 0.4 to 500 nm and lengths in the range of several microns to millimeters.¹ Via a catalytic CVD process, carbon nanotubes and nanofibers can be grown by the diffusion of carbon through a metal catalyst, and subsequent precipitation as graphitic filaments.²⁻⁴ There are three identified structural types of graphitic filaments based on the angle of the graphene layers with respect to the filament axis,^{5,6} i.e., platelet stacked, herringbone stacked (or cup-stacked), and tubular stacked, as shown in Figure 6.1.

It can be seen that the carbon layers are perpendicular to the filament axis in the platelet stacked form (Figure 6.1(a)), the carbon layers are at an angle to the filaments axis in the herringbone form (Figure 6.1(b)), and tubular carbon layers are parallel to the filament axis in the tubular form (Figure 6.1(c)). The herringbone form is a transition form from the point of the angle to the filament axis. In the common practice today, researchers classify the platelet stacked and the herringbone forms of graphitic filaments under the nomenclature of “nanofibers”; whereas, they describe the tubular stacked form as “nanotubes”. In our work, we will keep these terminologies because the nanotube structure has unique properties that distinguish it from the nanofiber structure. With carbon layers parallel to the filaments axis, nanotubes would adopt several important properties of carbon layers, such as high electrical conductivity, thermal conductivity,

and mechanical strength along their axis. Nanotubes are also very inert and chemically stable due to very few open edges and dangling bonds in the structure compared to nanofibers.

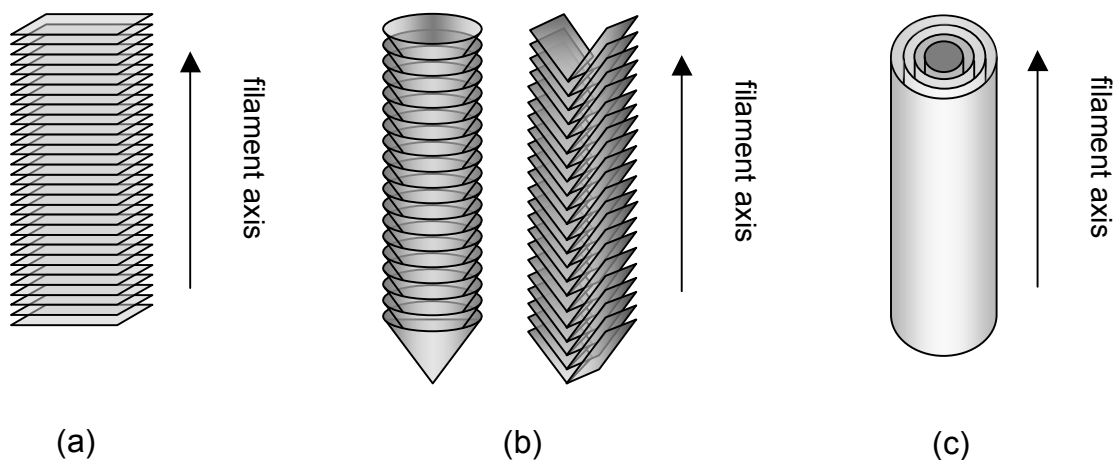


Figure 6.1. The three structural types of carbon filaments, classified by the angle of graphene layers with respect to the filament axis. (a) platelet stacked, (b) herringbone, and (c) tubular. Adapted from Rodriguez *et al.*⁵

Boron-doped carbon nanotubes and nanofibers have been synthesized via a catalytic CVD method, as described in Chapter 4. We use X-ray powder diffraction and Raman spectroscopy to characterize the crystal structures of the as-deposited products, and use high-resolution transmission electron spectroscopy (TEM) to analyze the structures of the product at the nanometer scale. Nanofiber structure (i.e. platelet and herringbone stacked) is the primary structure in the products, so in most cases we use the term nanofiber for the general deposited products. There is an interest in the analysis of boron concentrations and locations as a function of these structures. For this reason, a combination of Z-contrast imaging and electron energy loss spectroscopy (EELS) conducted in the scanning transmission electron spectroscopy (STEM) is used to

characterize the structure-related chemistry, i.e., the structure and chemistry on the atomic level.

6.2 Experimental Procedures

6.2.1 X-Ray Diffraction

X-ray diffraction data are collected using a Siemens/Bruker D500 diffractometer equipped with a 1° divergence slit, a 0.05° receiving slit, a graphite monochromator, and a scintillation detector. The Cu K_{α} X-ray source (Cu K_{α} $\lambda=1.54056\text{\AA}$) is used at 40 kV and 30 mA. Diffraction patterns from the samples as-deposited on the fused quartz slides are collected in a step-scanned mode, with an interval of $0.02^{\circ} 2\theta$, and a dwell time of 10 sec/step at room temperature. The NIST SRM 640b silicon⁷ is used as the external standard to calibrate the peak position, and account for systematic line broadening. The XRD patterns are analyzed using Jade 7 software (Materials Data Inc, 2004).

The interplanar spacing of d_{002} is calculated using Bragg's law. Crystallite size L_c is calculated using the Scherrer equation:⁸

$$L_c = k\lambda / \beta \cos\theta \quad (6.1)$$

where k is the Scherrer constant taken as 0.9,⁹ and β is the corrected FWHM value in radians. The corrected FWHM value, β , is the true FWHM without instrumental broadening, determined by the following:

$$\beta = \sqrt{\beta_{\text{obs}}^2 - \beta_{\text{std}}^2} \quad (6.2)$$

where β_{obs} is the observed FWHM value in radians, and β_{std} is the value of silicon in radians. The (002) reflection is used to obtain an average crystallite height, L_c .

6.2.2 Raman Spectroscopy

The Raman spectra of samples are acquired using a Renishaw System 1000 Raman spectroscope, equipped with a Leica DMLM integral microscope. Radiation of 632.8 nm from a 25 mW air-cooled He-Ne laser (Renishaw) is used for excitation. Raman scattering is collected with a 50x, 0.75NA dry objective. A silicon wafer with a Raman band at 520 cm^{-1} is used to calibrate the spectrometer to a spectral accuracy approaching 1 cm^{-1} . The spectra are recorded in an air atmosphere at room temperature.

6.2.3 High-resolution TEM

High-resolution electron microscopy is performed with a Hitachi HF-2000 Cold Field-emission Electron Microscope (FE-TEM). The accelerating potential is 200 kV, and no coating is used.

6.2.4 Electron Energy-Loss Spectroscopy (EELS) combined with Z-contrast imaging

EELS measurements are carried out with a Gatan 678 imaging filter attached to a Philips CM200-FEG TEM/STEM microscope. With a 200 keV field-emission gun, this microscope provides an electron probe of $\sim 1 \text{ nm}$. Z-contrast images are obtained and used to position the electron probe for EELS measurements. The EELS line scan technique is employed with a step size of 2 nm/step .

The peak integration intensity over the energy window of element X, I_X , is used for EELS quantification analysis:¹⁰

$$I_X(\alpha, \beta, \Delta, E_0) = I_{ZL} \cdot \sigma_X(\alpha, \beta, \Delta, E_0) \cdot n_X \cdot t \quad (6.3)$$

where α is the convergence semi-angle of incident beam, β is the collection semi-angle of scattered electrons, Δ is energy window width, E_0 is incident beam energy, I_{ZL} is elastic zero loss peak intensity at 0 eV energy loss, σ is atom partial ionization cross-section which is a function of α , β , Δ and E_0 , n_X is atoms per unit volume, and t is specimen thickness. According to the integrated intensity over the energy window of boron and carbon, the B/C atom ratio is determined by:

$$\frac{n_B}{n_C} = \frac{I_B}{I_C} \cdot \frac{\sigma_C}{\sigma_B} \quad (6.4)$$

where σ_C and σ_B are the carbon and boron atom partial ionization cross-sections, respectively.

6.3 Results and Discussion

6.3.1 Structure Analysis of Boron-doped Carbon Nanofibers

6.3.1.1 X-ray Diffraction Studies

All the XRD patterns for the boron-doped carbon nanofibers exhibit only 00 l peaks. In all instances the 002 reflection is observed, and in some case the 004 peak is discernable, but weak. This suggests that preferred orientation effects are present in all samples due to the basal sheet-like structure of graphite-like crystalline structures; this is also observed in boron-doped carbon films.¹¹ Therefore, XRD only provides information pertaining to the 002 peak position and shape. Figure 6.3 and Figure 6.4 show the XRD patterns of boron-doped carbon nanofibers in the range 23-30° 2 θ . Table 6.1 lists the calculated results and their accuracies of interlayer spacing (d_{002}) and average crystallite height size (L_c) from 002 peaks of the samples. The calculation of accuracies of d_{002} and L_c were described in Chapter 2. We recognize that L_c should be reported only to ± 2 nm. Boron concentrations determined by AES are also given in Table 6.1.

In the sample Group I, d_{002} and L_c change little with the reactant ratio $\text{BCl}_3/\text{C}_6\text{H}_6$, or boron concentration in the samples. However, for sample Group II, d_{002} and L_c are correlated with the deposition temperature. The interlayer spacings increase from 0.3343-0.3397 nm, and crystallite height sizes decrease from 17.3-5.8 nm with an increase in deposition temperatures from 750-900 °C. Lower d_{002} and larger L_c indicates improved crystallization along the hexagonal c -axis.^{12,13} Compared to d_{002} and L_c of the boron-doped carbon film, all the boron-doped carbon nanofiber samples have a lower d_{002} and a larger L_c . This suggests that boron-doped carbon nanofibers are better crystallized than the films along the c -axis in the layered structure.

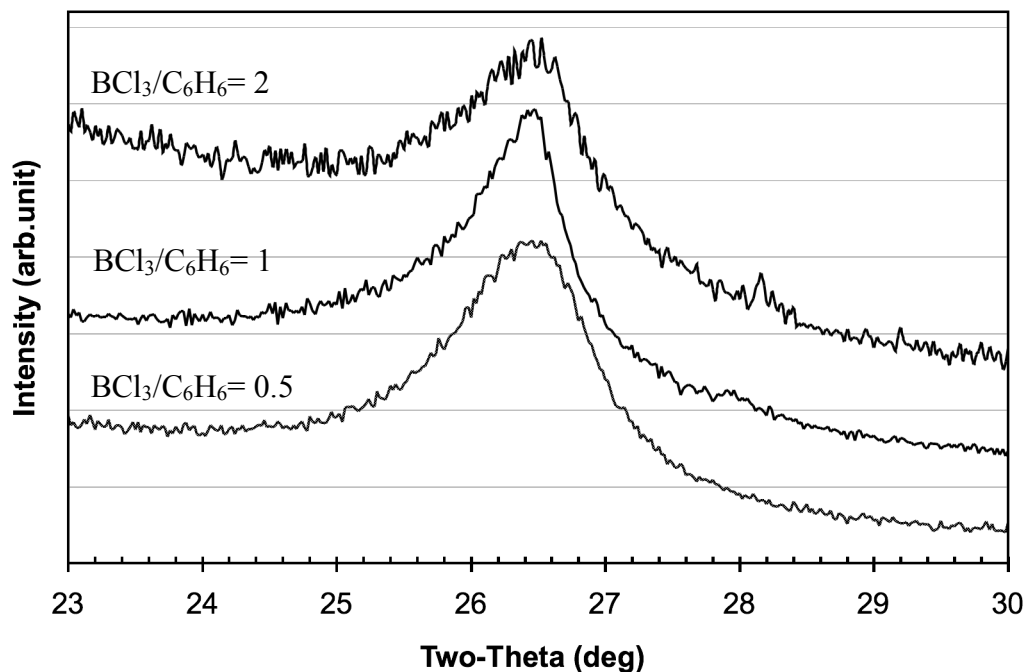


Figure 6.2. XRD patterns of boron-doped carbon nanofibers deposited with the reactant ratios $\text{BCl}_3/\text{C}_6\text{H}_6 = 0.5$, 1, and 2.

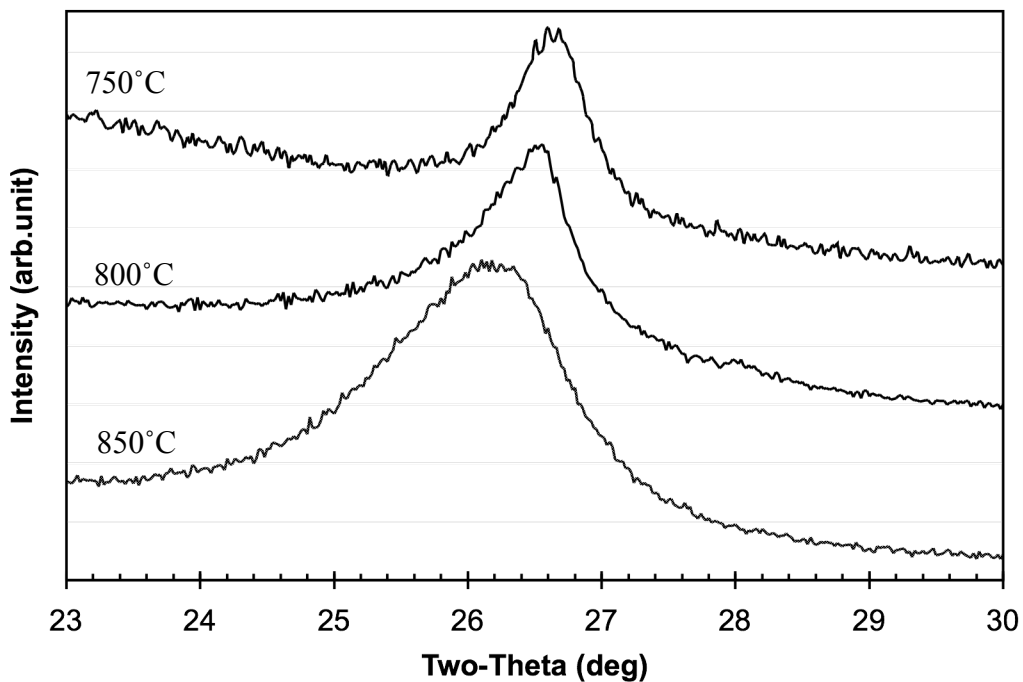


Figure 6.3. XRD patterns of boron-doped carbon nanofibers deposited at temperatures of 750°C , 800°C and 850°C .

Table 6.1 XRD Analysis of Boron-doped Carbon Nanofibers

Samples ^a	B at.% by AES	2 θ (002) (degree)	d ₀₀₂ (nm)	FWHM (002) (degree)	L _c (002) (nm)
I-2	18.4%	26.46 (0.02)	0.3366 (0.0005)	1.217 (0.025)	8.3 (2)
I-1	13.3%	26.44 (0.02)	0.3368 (0.003)	1.104 (0.016)	9.1 (2)
I-0.5	10.1%	26.47 (0.02)	0.3365 (0.0003)	1.250 (0.012)	8.1 (2)
II-750C	6.3%	26.64 (0.02)	0.3343 (0.0003)	0.631 (0.010)	17.3 (3)
II-800C	11.3%	26.52 (0.02)	0.3359 (0.0003)	0.902 (0.015)	11.4 (2)
II-850C	8.4%	26.21 (0.02)	0.3397 (0.0003)	1.590 (0.011)	5.8 (2)
A (C _x B film)	11.2%	26.20 (0.02)	0.3399 (0.0003)	3.148 (0.001)	3.0 (2)

^a The synthesis conditions of samples are described in Appendix A.

Note that sample II-750C has an interlayer spacing ($d_{002}=0.3343$ nm) that is even lower than the interlayer spacing of well-crystallized graphite, SP-1 ($d_{002}=0.3355$ nm).¹⁴ SP-1 has been referenced as a standard for well-crystallized graphite with a crystallite size of more than 1000 nm.¹⁵ So what causes the very low d_{002} of sample II-750C? A reasonable explanation is that a strain caused by a uniformly compressive stress in the structure leads to a peak shift to the higher 2θ , i.e., a smaller lattice parameter. More proof of the strain in sample II-750C will be visually observed from the real space structure characterization using high-resolution TEM present in Section 6.3.1.3.

The crystal strain ε along c -axis parallel to the tube axis for Sample II-750C can be calculated by:

$$\varepsilon = \Delta d / d_0 \quad (6.5)$$

where d_0 is the equilibrium interlayer spacing for a boron-doped carbon structure, and Δd is the difference in the interlayer spacing induced by the stress, respectively. We use the interlayer spacing of boron-doped carbon film (sample A) as d_0 since the film are synthesized under an approximately equilibrium condition. The stress, σ , along the c -axis can be calculated by:

$$\sigma = \varepsilon \cdot E \quad (6.6)$$

where E is elastic modulus (36.5 GPa)¹⁶ of the inter-graphite networks, which is perpendicular to the direction of covalent bonds. Hence, the calculated strain and stress of sample II-750C are 1.6 % and 0.58 GPa, respectively.

In summary, XRD analysis reveals that boron-doped carbon nanofibers are highly orientated, and possess a graphite-like structure. The interlayer spacings, d_{002} , range from 0.3343 to 0.3397 nm, while the crystallite sizes, L_c (002), range from ~5 to 20 nm. The interlayer spacings increase, and crystallite sizes decrease with increasing deposition temperatures. Additionally, strains occur in the samples, and ultimately lead to a small lattice parameter, d_{002} , relative to pure, well-crystallized graphite.

6.3.1.2 Raman Spectroscopy

Raman spectroscopy is an effective method for studying structures of different carbon materials, including carbon nanofibers and nanotubes.¹⁷⁻²⁰ It is well known that carbon has two forms of crystalline structures, diamond and graphite, and a wide range of disordered forms. The Raman spectrum of a face-centered cubic (FCC) lattice of diamond is quite simple. The Raman-active phonon of diamond is a single, triply

degenerate zone-centered vibrational mode, which is characteristic of the C–C single bonds between sp^3 -carbon atoms in its cubic structure. The Raman spectrum of diamond exhibits only one sharp band at 1332 cm^{-1} .²¹ The Raman spectrum of graphite is more complicated. In the case of hexagonal crystal graphite, the first order Raman spectrum consists of a very strong, high-frequency, in-plane stretching mode (E_{2g}^2 or G-band) at 1582 cm^{-1} and a weaker, low-frequency, shear mode at 42 cm^{-1} (E_{2g}^1).^{21,22} When disorder is introduced into the graphite structure, the existing bands broaden, and additional bands are found at about 1360 cm^{-1} (D-mode) and 1620 cm^{-1} (D'-mode), which are attributed to disorder-induced Raman activity of zone boundary A_{1g} phonons.^{23,24} In the rather small, or disordered crystals with very little three-dimensional order, the G- and D'-bands merge into a single broader feature. The line broadening, especially the broadening of the G-band, is related to disorder within the carbon sheet.¹⁹ Stacking disorder of the sheets is related to vibrations along the c -axis, and exhibits a feature on the second order band at 2700 cm^{-1} .²⁵

Raman spectroscopy has been developed as a standard method for determining the planar coherence length L_a in graphitic carbon that possesses limited long-range order.^{19,22} The integral intensity ratio I_D/I_G is inversely proportional to the planar crystallite size L_a over a range of 2.5-300 nm for laser wavelengths of 400-700 nm:^{19,22}

$$\frac{I_D}{I_G} = \frac{4.4\text{nm}}{L_a} \quad (6.7)$$

Both the band positions and bandwidths of G- and D-modes are sensitive to L_a , and the downshifting of the G-band position has been correlated with the presence of bond-angle

disorder. The D- and G-modes were also found to be sensitive to the type of carbon bonding, i.e. sp^2 or sp^3 hybridization. Information on the sp^2/sp^3 -bonded fraction of carbon can be obtained from the band position of D- and G-modes, and from the integral intensity of D-band.²⁶

In an early Raman study on boron-doped natural graphite (0.6 wt.% B),²⁷ it was found that substitutional boron doping into the graphite lattice led to an upshift of Raman bands at 1580 cm^{-1} to 1590 cm^{-1} , accompanied by a slight broadening. The boron doping also caused a remarkable increase in intensity of the D-band at 1360 cm^{-1} , which is a defect-induced vibration mode. The upshift of Raman band at 1580 cm^{-1} was explained by a decrease in repulsion between the graphite layers as a result of the presence of substitutional boron.²⁷ Similar results have been observed in the studies of boron-doped carbon films deposited by thermal CVD processes.^{11,28} Therefore, substitutional boron doping in carbon causes distortions in the graphite lattice, and results in both an upshift and broadening of G-band coupled with an increase in the intensity and broadening of D-band. Interstitial boron doping in carbon has no such effects.²⁹

Raman spectra of the boron-doped carbon nanofibers are given in Figure 6.4 and Figure 6.5. Raman bands appear at approximately 1350 cm^{-1} (D-band) and 1570 cm^{-1} (G-band), as listed in Table 6.2. Boron concentrations of samples determined by AES are also given in Table 6.2. As-deposited boron-doped carbon film (sample A) exhibits Raman bands at 1360 and 1590 cm^{-1} , as expected by the effect of substitutional boron doping in graphite lattice. The G-bands of boron-doped carbon nanofibers are lower, ranging

from 1561-1580 cm^{-1} . The widths of G-bands of nanofibers are between 100-118 cm^{-1} , are similar to the film. The D-bands of boron-doped carbon nanofibers are in the range of 1344 -1361 cm^{-1} , with their widths between 212-260 cm^{-1} . For all the boron-doped carbon nanofibers, both G-bands and D-bands have no dependence on the boron concentration. However, the widths of G-bands increase slightly, and the band ratios, I_D/I_G , decrease with an increase in deposition temperatures (Table 6.2). The broadening of G-bands is directly related to disorder within the carbon layers, and I_D/I_G reveals a statistical crystallite size along carbon layers of the samples. The planar crystallite size (L_a , or called crystallite width) for each sample is calculated using Equation 6.7, and is given in Table 6.2. There is no dependence of the L_a on the boron concentration, but L_a increases with increasing deposition temperatures. Figure 6.6 shows a linear increase in L_a of boron-doped carbon nanofibers with an increase in deposition temperature.

There are several questions raised based on the Raman results. First, why does the position of G-bands of boron-doped carbon nanofibers drop to a lower frequency which is in the range of G-band of undoped graphite crystal ($\sim 1575 \text{ cm}^{-1}$) instead of shifting to a higher frequency as predicted by Hagio *et al.* (1590 cm^{-1})?²⁷ Second, why do the results reveal both a slight increase in G-band broadening with deposition temperature and a linear increase in L_a with deposition temperatures? Third, X-ray diffraction analysis shows that there is a decrease in the crystallite height (L_c) with deposition temperatures and this is an apparent conflict with the increase in crystal width (L_a).

To answer these questions, we have to consider the influence of both B-doping and the nano-scaled structural form. We have pointed out that compressive stress and strain exists in the nanofiber samples, which decreases the interlayer spacing. The compressive stress (up to 0.58 GPa) would counterbalance the decrease in repulsion between the graphite layers resulting from the presence of substitutional boron.²⁷ As a result, boron-doped carbon nanofibers do not exhibit an upshift of G-bands as would the boron-doped carbon thin films.

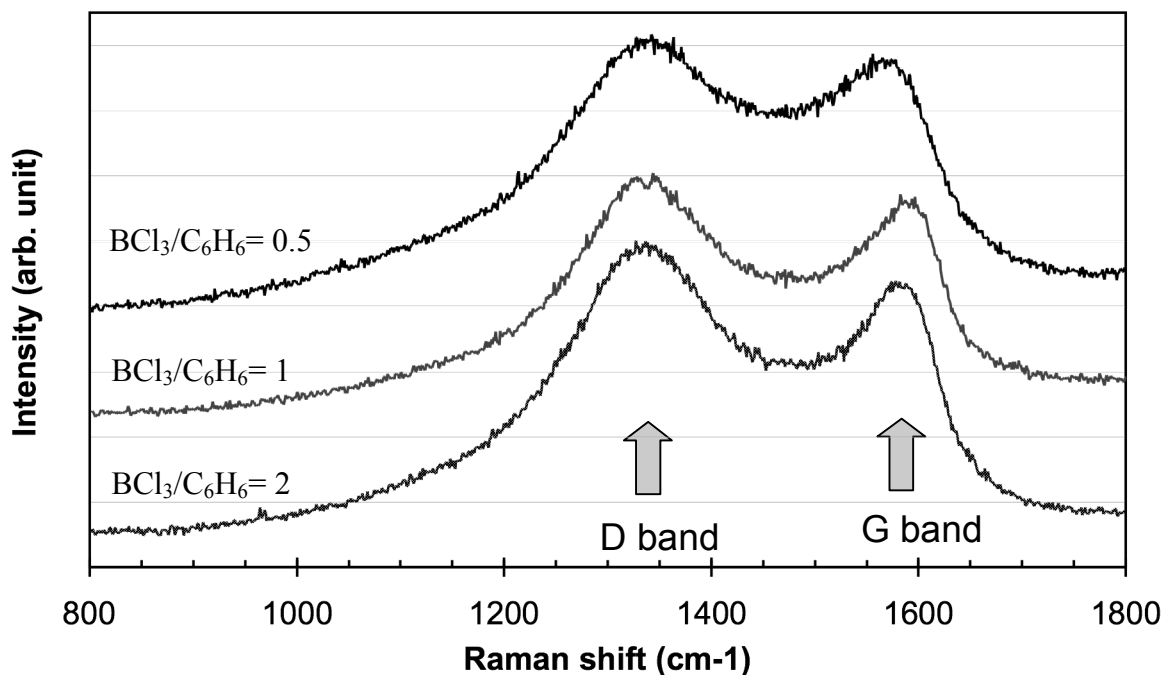


Figure 6.4. Raman spectra of boron-doped carbon nanofibers deposited with the reactant ratios $\text{BCl}_3/\text{C}_6\text{H}_6 = 0.5, 1, \text{ and } 2$ at 800°C for 30 min.

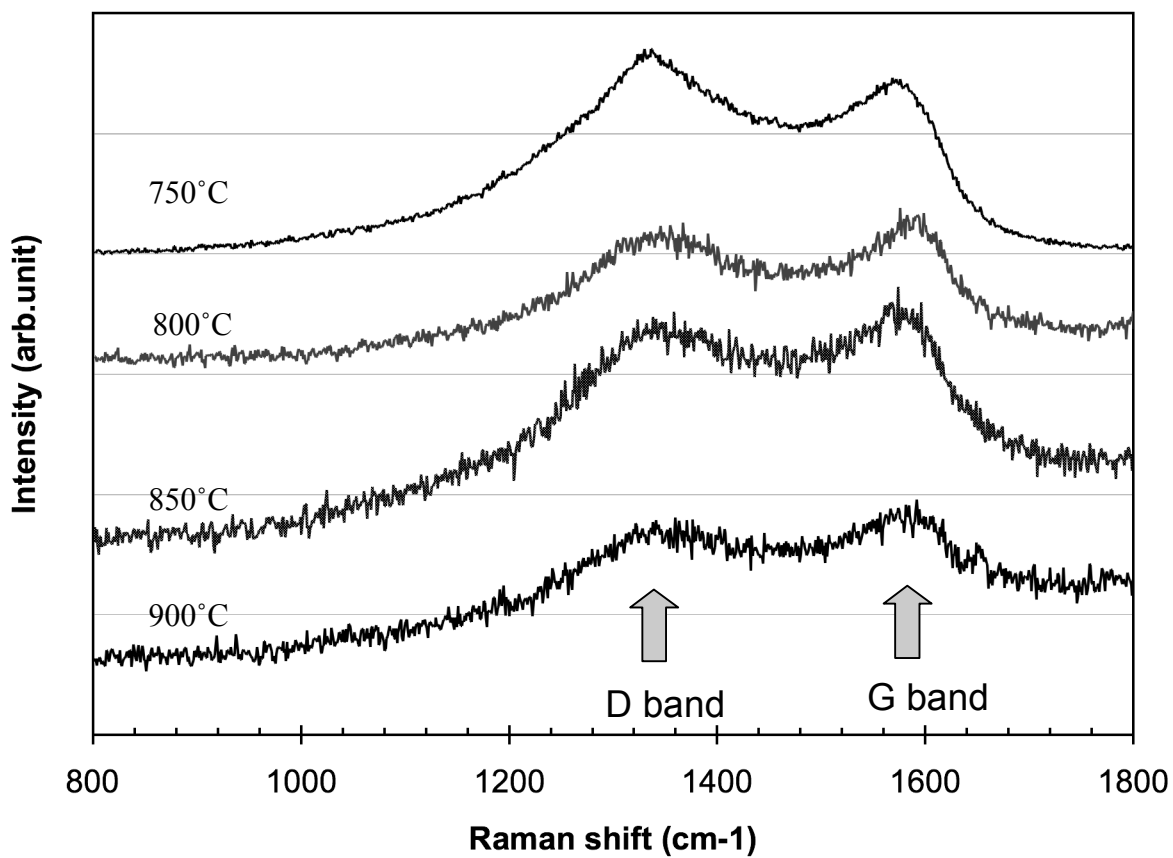


Figure 6.5. Raman spectra of boron-doped carbon nanofibers deposited at temperatures from 750-900°C with a reactant ratios $\text{BCl}_3/\text{C}_6\text{H}_6 = 1$.

Table 6.2 Raman Analyses on Boron-doped Carbon Nanofibers

Samples	B at.% by AES	G Band		D Band		I_D/I_G	L_a (nm)
		ν_G (cm ⁻¹)	$\Delta\nu_G$ (cm ⁻¹)	ν_D (cm ⁻¹)	$\Delta\nu_D$ (cm ⁻¹)		
I-2	18.4%	1575	100	1344	245	1.44	3.06
I-1	13.3%	1575	102	1344	250	1.34	3.28
I-0.5	10.1%	1561	105	1349	283	1.58	2.78
II-750C	6.3%	1567	101	1347	260	1.51	2.91
II-800C	11.3%	1580	102	1351	215	1.33	3.31
II-850C	8.4%	1576	111	1361	223	1.21	3.64
II-900C	4.8%	1574	118	1349	212	1.04	4.23
A (C _x B film)	11.2%	1590	110	1360	245	1.26	3.06

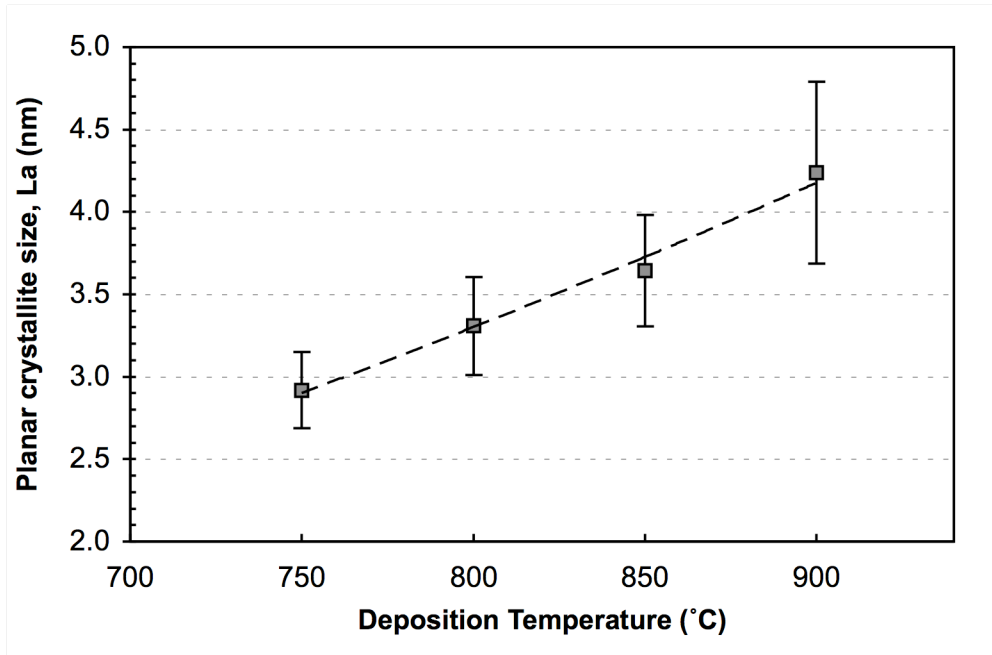


Figure 6.6. Planar crystallite size L_a as a function of deposition temperatures.

Having substitutional boron present, the larger B-C bond length (1.56 Å) compared to C-C bond length (1.42 Å) leads to a symmetry disruption, which occurs at boron atoms that are responsible for G-band broadening. Accordingly, the slight increase in the G-band broadening, allows one to deduce that higher deposition temperatures cause more disordering of the layers. In addition, Raman spectroscopy is very sensitive with respect to the intrinsic defects of graphite lattice. Equation 6.7 assumes that graphite becomes uniformly nanocrystalline, and the smaller crystallites are therefore taken into account more.^{22,30} On the other hand, XRD is more sensitive to the largest crystallites. For a system with mixed grain sizes, we can explain why the XRD dimensions (L_c) are larger than the Raman dimensions (L_a): Equation 6.7 will underestimate L_a due to the dominant effect of small crystallites.^{17,30}

Based on the observations from electron microscopy, we realize the microstructure of the boron-doped carbon nanofibers is inhomogeneous. Therefore, we conclude that the crystal structure of these nanofibers is also inhomogeneous, and has mixed crystallite sizes of both L_a and L_c . Lower deposition temperatures favor the growth of larger crystallites along the c -axis, while higher deposition temperatures enable an increase in planar crystallite width. For this reason, the L_a and L_c dependencies on the deposition temperature exhibit opposing effects.

6.3.1.3 Transmission Electron Microscopy

High-resolution TEM has been carried out on Group I (Figures 6.7-6.9) and Group II (Figures 6.10-6.14) samples to study the micro- and nano-structure of boron-doped carbon nanofibers. The morphologies of these samples vary considerably. The synthesis conditions for each sample are listed in Appendix A.

Group I samples (assigned as I-0.5, I-1 and I-2) are synthesized with reactant ratios ($\text{BCl}_3/\text{C}_6\text{H}_6$) at 0.5, 1 and 2, respectively. There are fibers with diameters of two scales observed in each sample. The fat fibers have a diameter on the submicron scale (0.1-0.9 μm), and the small fibers have a diameter on the nanometer scale (<100 nm). Sample I-0.5 (Figure 6.7) has both submicron fibers with a diameter of 0.5-0.7 μm , and nanofibers with a diameter of 60-100 nm. The submicron fibers were previously observed by SEM. The nanofibers have open tips, and two textures along the fiber axis (Figure 6.7b): herringbone stacked in the core and tubular stacked on the exterior. The herringbone stacked layers, with an angle of $\sim 20^\circ$ to fiber axis, have the effect of building up cones one over another. No catalyst particles are observed in the nanofibers.

The structure of sample I-1 (Figure 6.8) is similar to I-0.5. Both submicron fibers (a diameter of 0.3-0.4 μm), and nanofibers (diameter of 45-60 nm) exist. Figure 6.8c shows a nanofiber with a diameter of 60 nm. This nanofiber has an open tip, and two textures along the fiber axis. In the core, herringbone stacked layers with an angle of $\sim 15^\circ$ to the fiber axis build up conical compartments one over another. On the exterior, carbon layers are parallel to the fiber axis, but are not as ordered as the herringbone stacked layers in

the core. Between the two textures, there is a disordered transition area. No literature to date has reported such a structure for nanofibers based primarily on carbon. We propose this structure is correlated with the presence of boron, and consequently, a modified growth mechanism.

Sample I-2 (Figure 6.9) has submicron fibers with a diameter of 0.12-0.25 μm , and nanotubes with diameters in the range of 15-30 nm. The submicron fiber is tubular, and hollow in the center (Figure 6.9a), while the nanotubes have a closed tip without an encapsulated catalyst particle.

Group II samples are synthesized at deposition temperatures between 750-900°C. Samples are assigned as II-750C, II-800C II-850C and II-900C, respectively. The structures of Group II are also inhomogeneous. The structure of sample II-750C is distinguished from the others in that it has fibers with diameters of one scale (0.12-0.14 μm). Figures 6.10 and 6.11 show two fibers with a broken tip, or perhaps a closed tip of sample II-750C. The first fiber in Figure 6.10 has two textures along the fiber axis: platelet stacked in the core and tubular stacked on the exterior. The tubular stacked carbon layers on the exterior, though parallel, are randomly displaced with respect to one another, and this structure is referred to as a turbostratic structure.^{31,32} However, the platelet stacking of carbon layers in the core is perfect, and the crystallite size is large (> 100 nm). The interlayer spacing in the core is measured to be 0.333(0.01) nm based on the calibrated scale bar associated with the high-resolution TEM, which agrees with the

XRD measurement of 0.334 nm (note that XRD result is based on the whole sample, and is thus an average value).

Figure 6.11 shows a second fiber with a closed tip that has a hollow carbon onion of sample II-750C. Similar to the first fiber, it has two textures along the axis: platelet stacked in the core, and tubular stacked on the exterior. However, the external tubular layers peel off from the platelet core, and it is hollow between these two textures. A hollow, onion-skin tip forms by the extension of the exterior tubular carbon layers. The onion-skin tip has the same diameter as the fiber, but carbon layers are well ordered, stacked with 8-14 layers.

The TEM observation on sample II-750 gives us some clues to explain this unique structure. First, the growth rates along the fiber axis of the platelet core and of the exterior tubular carbon are different. On the second fiber (Figure 6.12), the exterior tubular carbon grows faster, thus a hollow carbon onion-skin tip forms. Second, the exterior carbon formed earlier might limit the growth of the platelet core, and lead to a compressive strain on the platelet layers along the *c*-axis. As a result, the interlayer spacing determined by XRD is 0.334 nm and by TEM is 0.333 nm. However, both values are lower than the 0.3354 nm of a perfect graphite crystal.¹⁴

Sample II-800C (Figure 6.12) has submicron fibers with a diameter of $\sim 0.5 \mu\text{m}$ and nanotubes with diameters of 10-20 nm. The nanotubes (4-14 layers) have closed tips, without encapsulated catalyst particles. Sample II-850C (Figure 6.13) has submicron

fibers with a diameter of $\sim 0.35 \mu\text{m}$, and no nanotubes or nanofibers are observed by TEM. At the broken tip of a submicron fiber, a tubular core is exposed out of the outer fiber. The tubular core (in Figure 6.13b) is well ordered, and exhibits a higher strength than the larger outer fiber. Sample II-900C has no nanotubes or nanofibers observable by TEM. The fragment of this sample (Figure 6.14) shows a structure characteristic of well-ordered carbon thin film.

Table 6.3 is a summary of the observations on boron-doped carbon deposits by TEM. The structure of boron-doped carbon deposits is a function of reactant ratio (or boron concentrations) and deposition temperature. The results are in agreement with the

Table 6.3 TEM Observations on Boron-doped Carbon Deposits

Samples	B at.% by AES	Submicron fiber diameter	Nanofiber diameter	Texture of nanofibers (or nanotubes)
I-2	18.4%	0.12-0.25 μm	15-30 nm	Multi-walled nanotubes with a closed tip
I-1	13.3%	0.3 -0.4 μm	45-60 nm	Core: herringbone stacked Exterior: tubular stacked
I-0.5	10.1%	0.5 -0.7 μm	60-100 nm	Core: herringbone stacked Exterior: tubular stacked
II-750C	6.3%	0.12-0.15 μm	NA	Core: platelet stacked Exterior: tubular stacked
II-800C	11.3%	~ 0.3 -0.5 μm	10-20 nm	Multi-walled nanotubes with a closed tip
II-850C	8.4%	$\sim 0.35 \mu\text{m}$	NA	Core: well-ordered tubular stacked Exterior: tubular stacked
II-900C	4.8%	$> 0.5 \mu\text{m}$	NA	NA

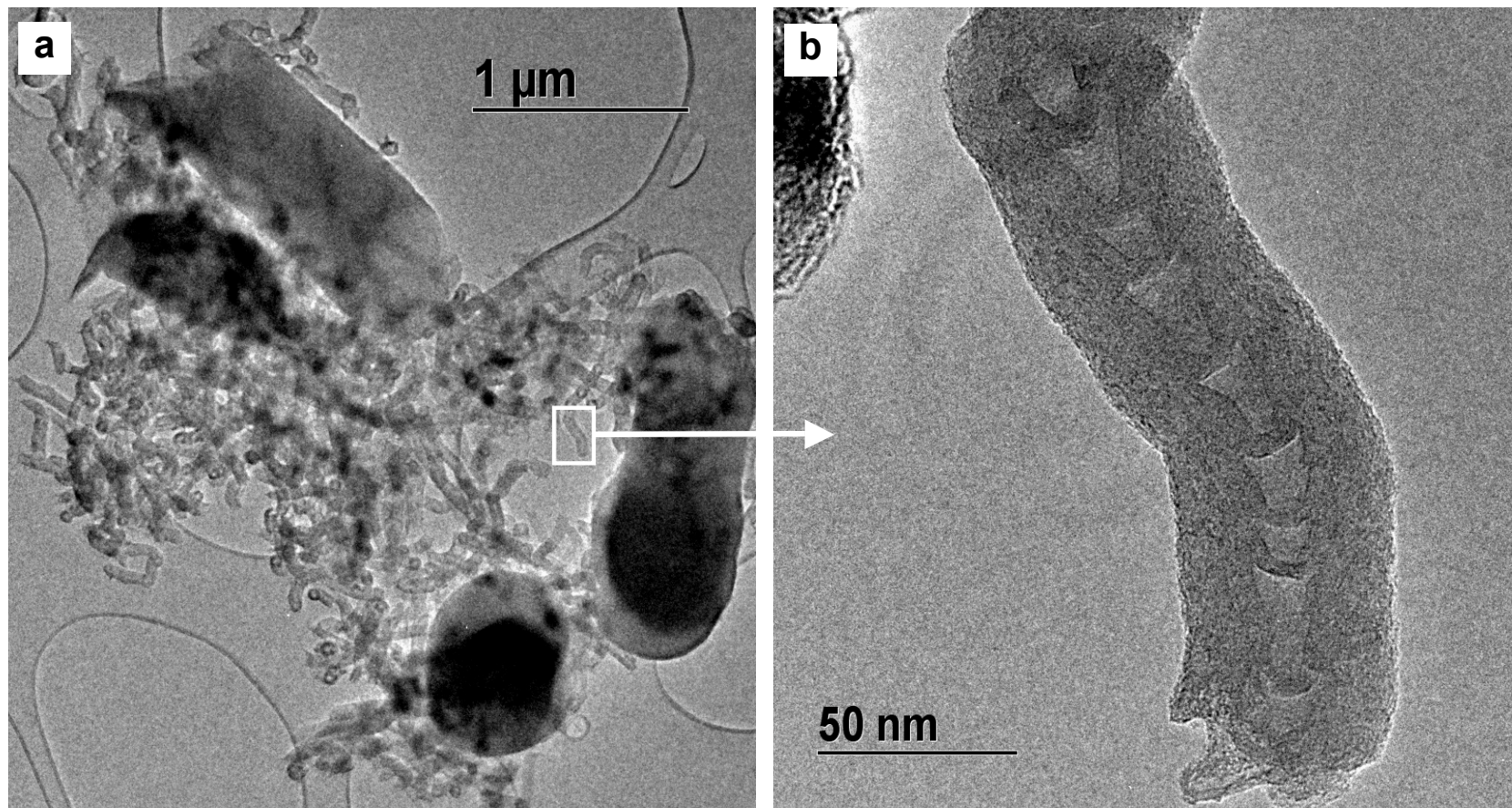


Figure 6.7. TEM images of Sample I-0.5. Both submicron fibers (diameter 0.5-0.7 μm) and nanofibers (diameter 60-100 nm) exist in this sample. The nanofibers have open tips, and two textures along the fiber axis: herringbone stacked in the core and tubular stacked on the exterior.

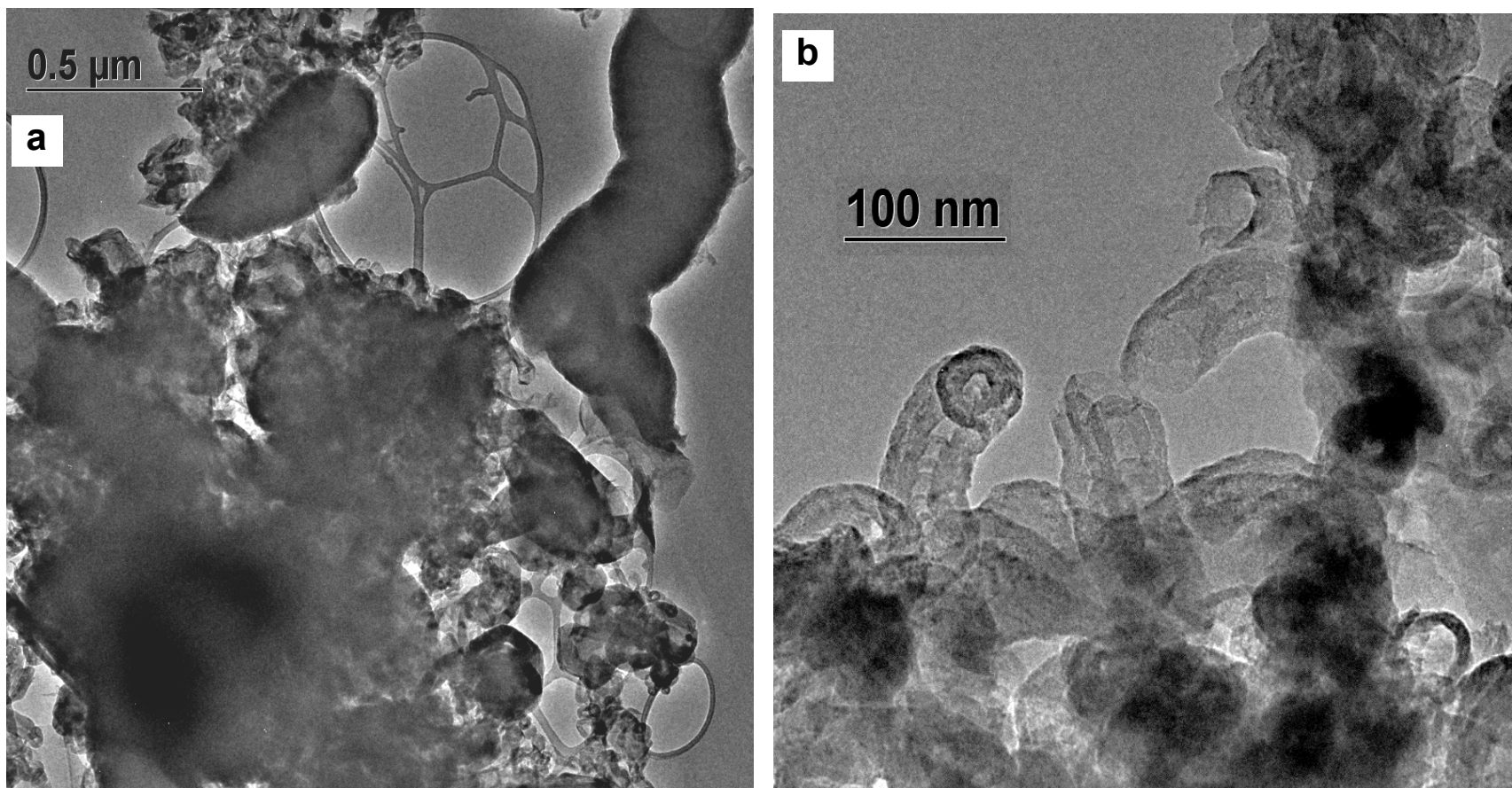


Figure 6.8. (a) and (b) TEM images of Sample I-1. Both submicron fibers (diameter 0.3-0.4 μm) and nanofibers (diameter 45-60 nm) exist in this sample. The nanofibers have open tips.

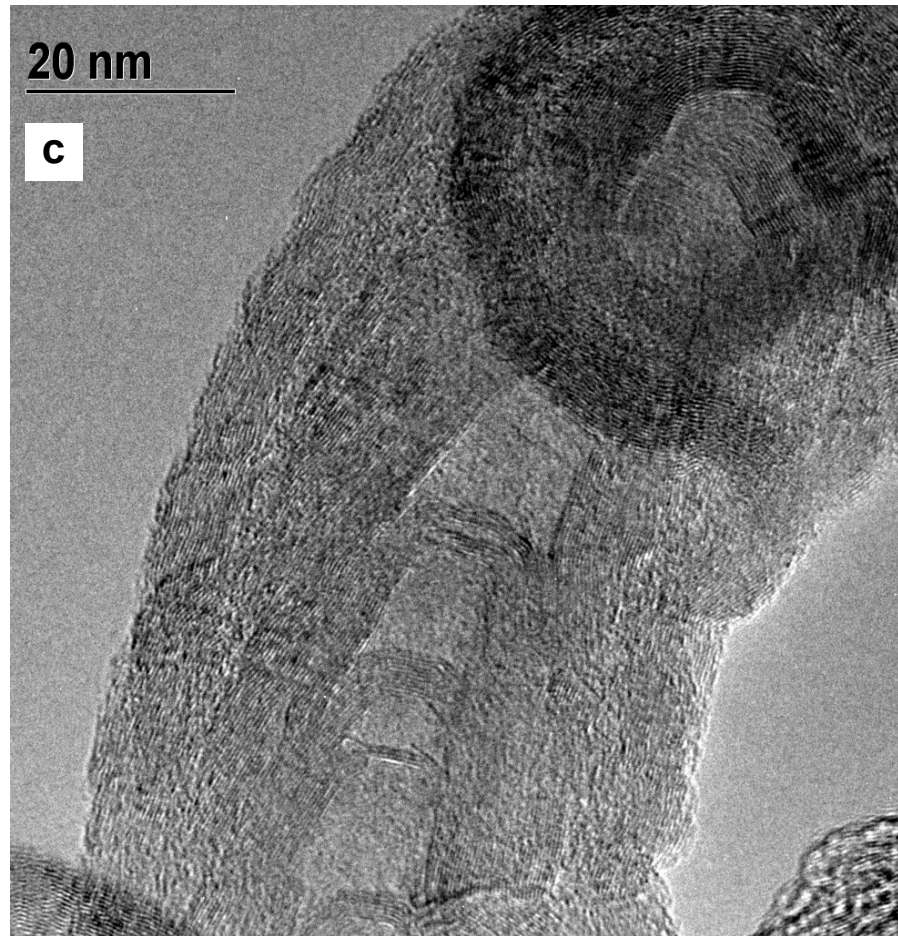


Figure 6.8. (c) High-resolution TEM image of a nanofiber in Sample I-1. The nanofiber has an open tip, and two textures: herringbone stacked in the core and tubular stacked on the exterior.

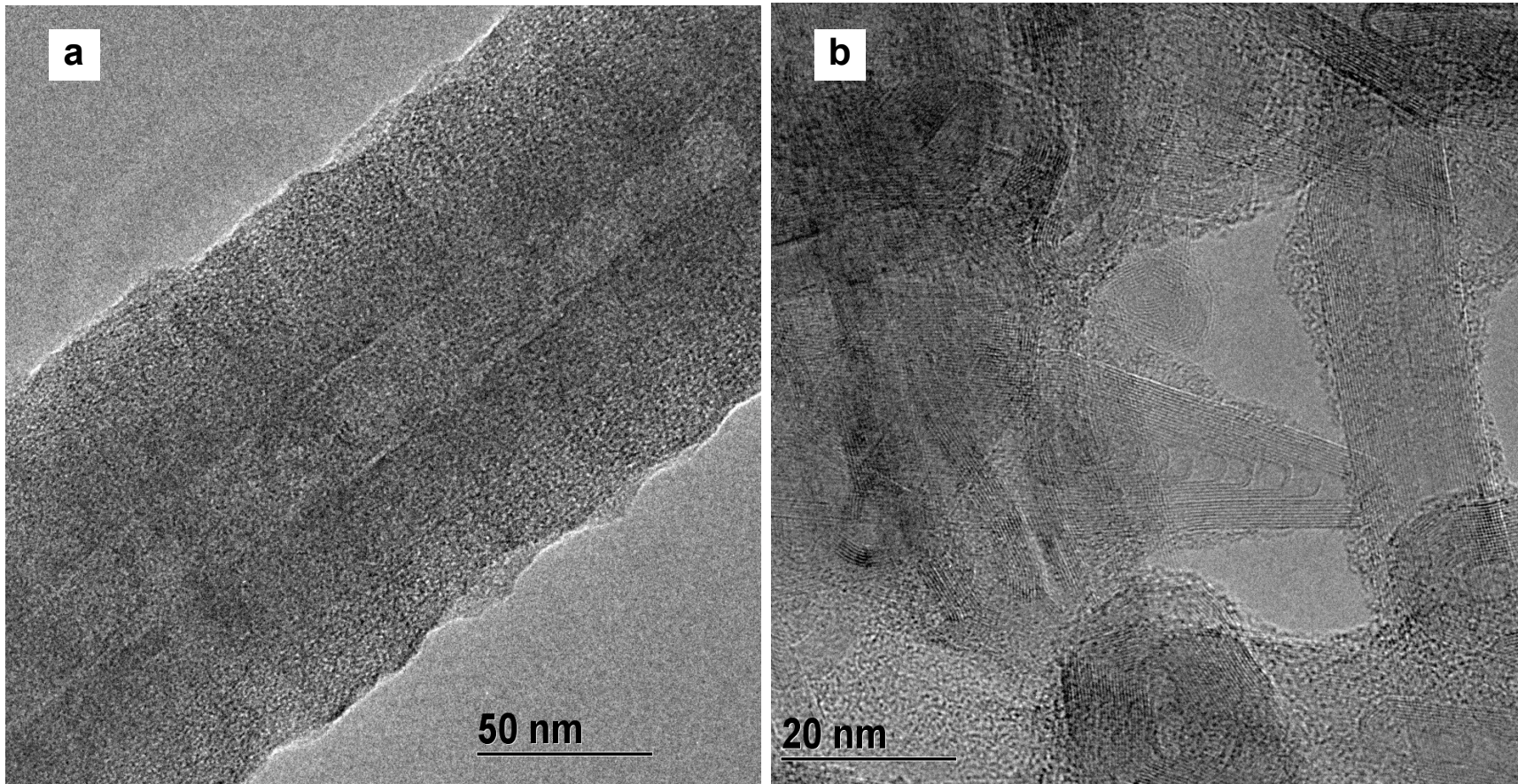


Figure 6.9. TEM images of Sample I-2. Both submicron fibers (diameter 0.12-0.25 μm) and nanofibers (diameter 15-30 nm) exist in this sample. Small fibers are multi-walled nanotubes with closed tips.

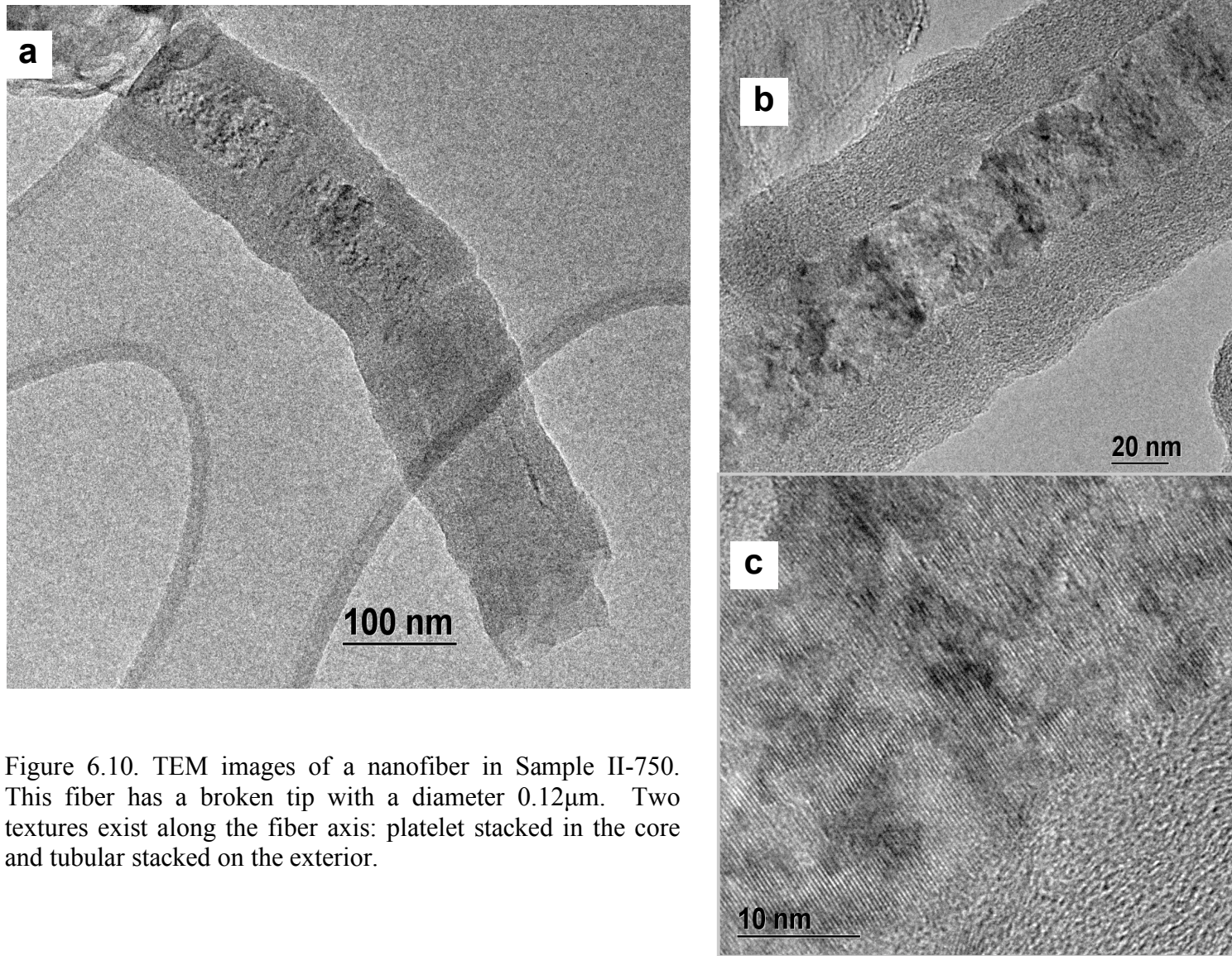


Figure 6.10. TEM images of a nanofiber in Sample II-750. This fiber has a broken tip with a diameter $0.12\mu\text{m}$. Two textures exist along the fiber axis: platelet stacked in the core and tubular stacked on the exterior.

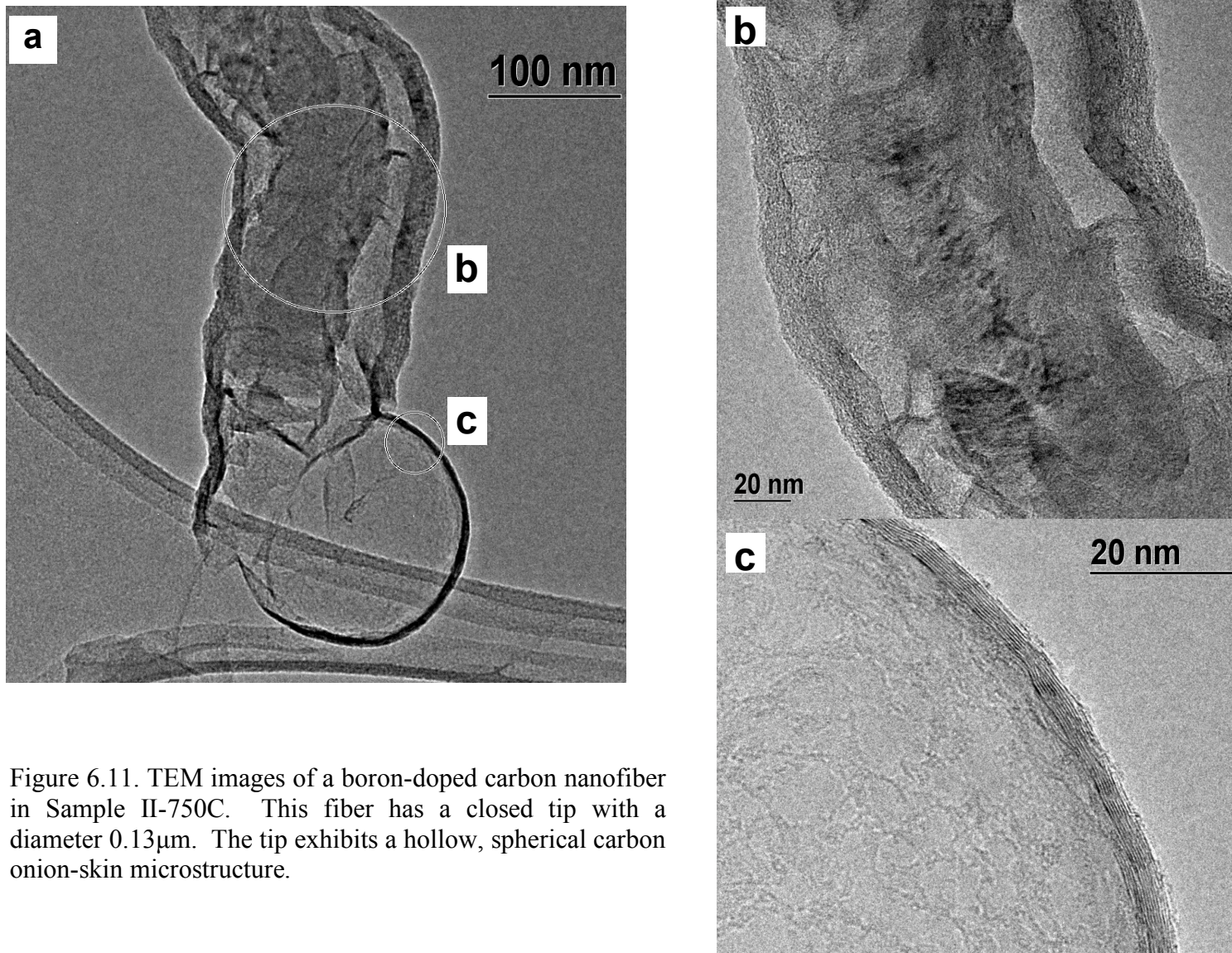


Figure 6.11. TEM images of a boron-doped carbon nanofiber in Sample II-750C. This fiber has a closed tip with a diameter $0.13\mu\text{m}$. The tip exhibits a hollow, spherical carbon onion-skin microstructure.

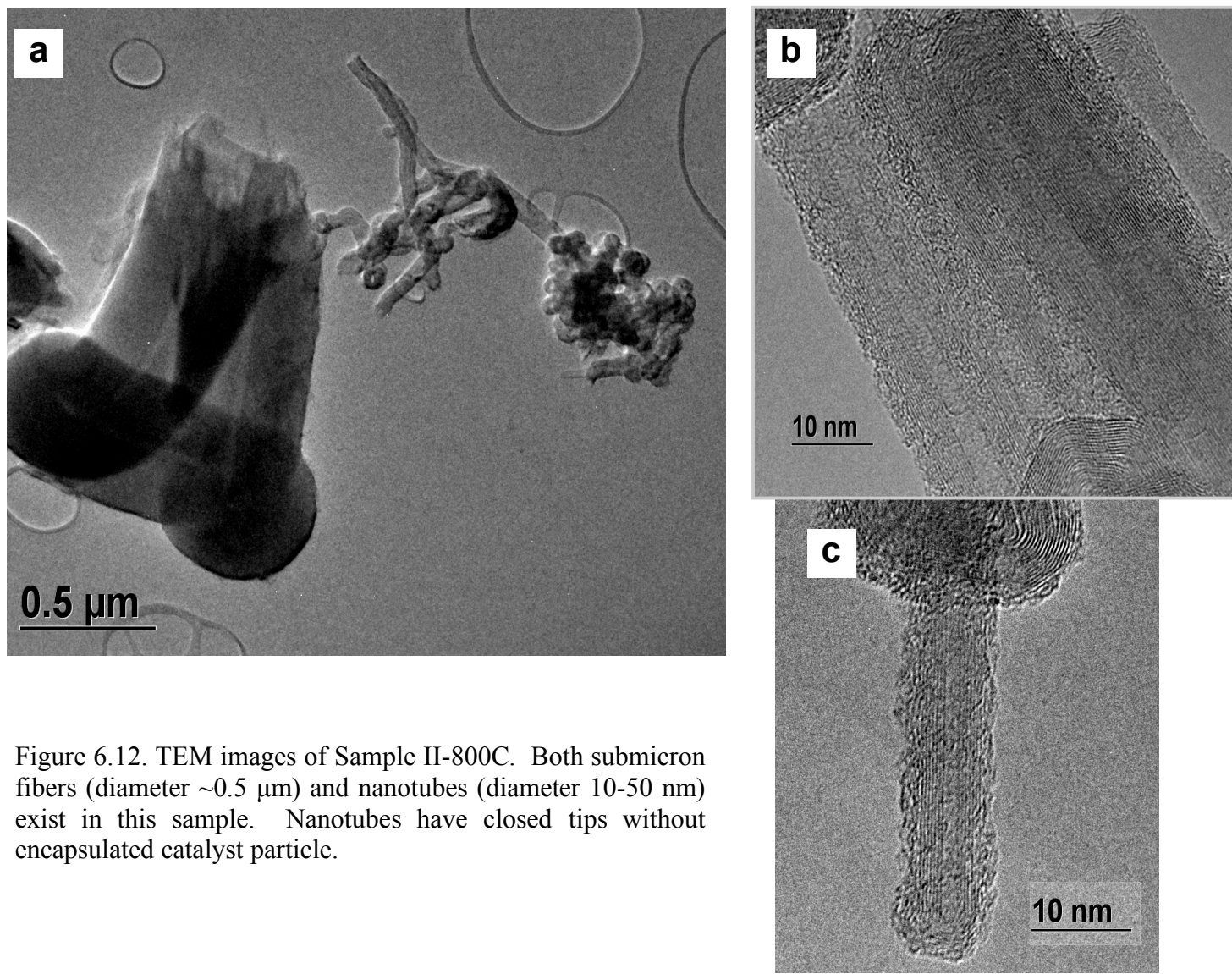


Figure 6.12. TEM images of Sample II-800C. Both submicron fibers (diameter $\sim 0.5 \mu\text{m}$) and nanotubes (diameter 10-50 nm) exist in this sample. Nanotubes have closed tips without encapsulated catalyst particle.

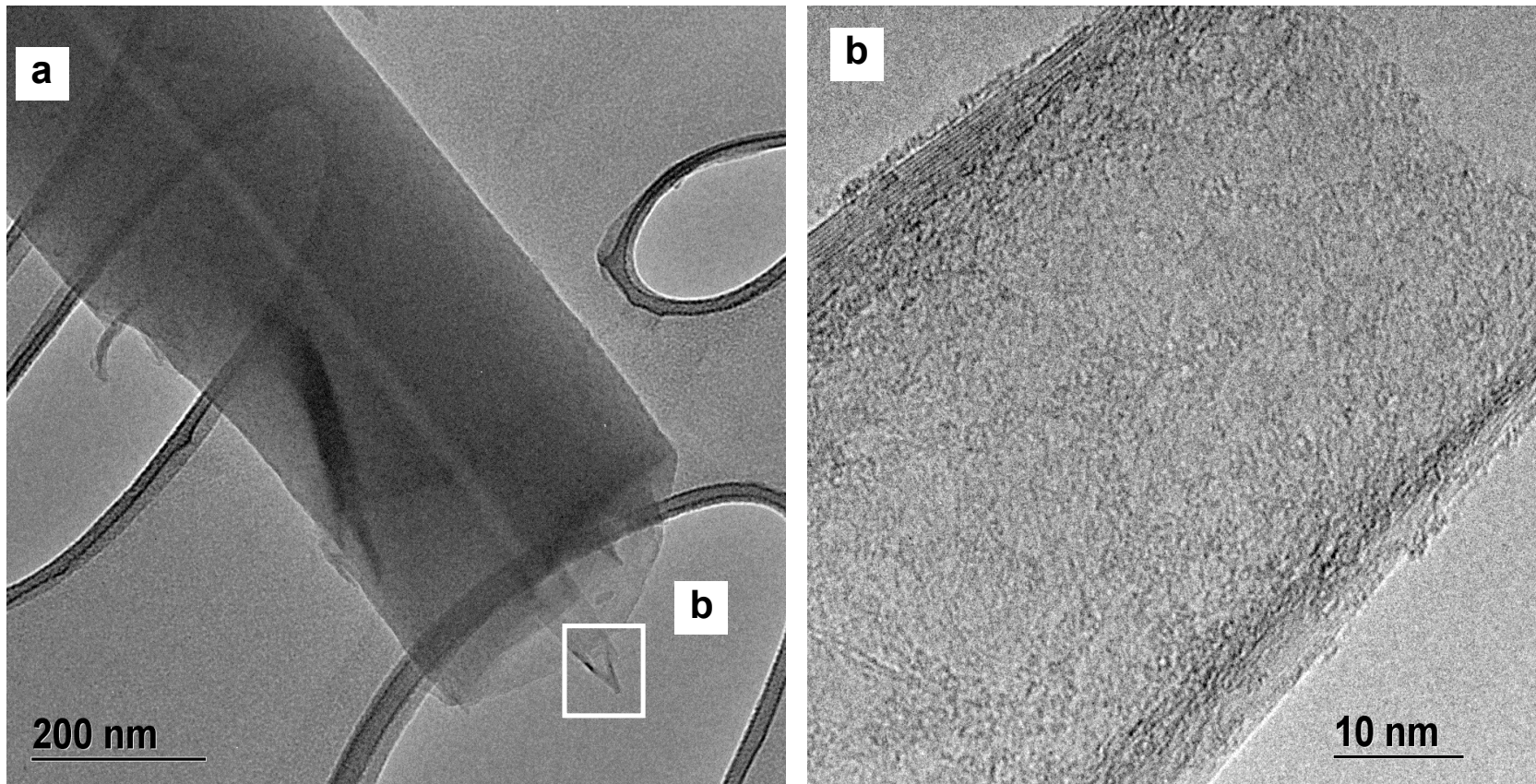


Figure 6.13. TEM images of a broken boron-doped carbon fiber of Sample II-850C. This fiber is tubular stacked, with a diameter $\sim 0.35 \mu\text{m}$. A well-ordered tubular core exists. Also shown is micrograph of the broken tip highlighted in a.

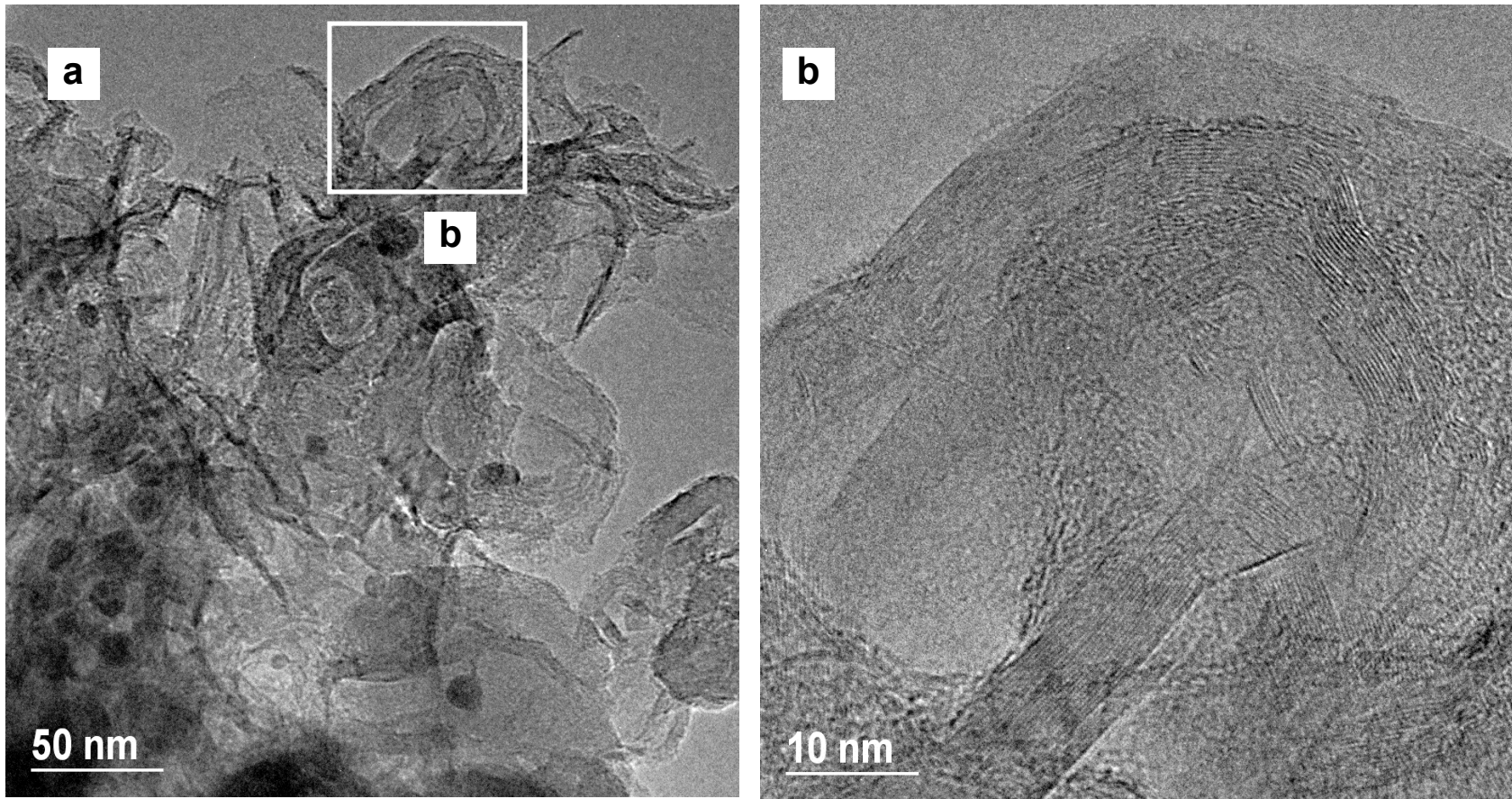


Figure 6.14. TEM images of the fragments of Sample II-900C.

observations by SEM. For Group I samples, the diameters of both the submicron fibers and nanofibers decrease with an increase in reactant ratio $\text{BCl}_3/\text{C}_6\text{H}_6$. When $\text{BCl}_3/\text{C}_6\text{H}_6$ reaches 2, multi-walled nanotubes grow instead of nanofibers. For Group II samples, an increase in deposition temperature not only increases the diameters of submicron fibers or nanofibers, but also changes the texture of the filamentous carbon. At a deposition temperature of 750°C , the fibers exhibit platelet stacking in the core, and disordered tubular stacking on the exterior zones. By increasing the deposition temperature, well ordered tubular stacking dominates the texture. Therefore, by TEM observation, the change in texture of filamentous carbon can be described as: (1) an increase in boron concentration changes the texture from herringbone form to tubular form; (2) an increase in deposition temperature helps to change the texture from platelet form to tubular form.

As shown in Figure 6.1, herringbone stacked texture is a form between platelet and tubular texture from the viewpoints of dangling bonds and the angle to the fiber axis. Although the herringbone form is not observed in the Group II samples, it is observed in Group I samples, which are deposited at an intermittent deposition temperature. We believe that the increase in deposition temperatures will transfer the texture from platelet stacking to herringbone stacking, ultimately to well-ordered tubular stacking. In addition, a high concentration of boron in the sample (>15 at.% B) favors the growth of filamentous carbon in samples of tubular texture.

Tanaka *et al.*³³ investigated the influence of deposition temperatures on the stacked texture of carbon nanofibers. Their results revealed that platelet stacked nanofibers were

deposited at low temperatures and tubular nanofibers were deposited at higher temperatures. Also the texture transition temperature depended on the metal composition of the catalyst particles. As a result, Tanaka *et al.* hence proposed that the alignment and degree of graphitization of carbon layers would be governed by the nature of the catalyst particles. But no further discussion was offered to explain the change in texture as a function of the deposition temperature.

Hofmann *et al.*³⁴ studied the low-temperature growth of carbon nanotubes and nanofibers by plasma-enhanced CVD, and found the activation energy for the growth rate is ~23 kJ/mol at low temperature (500-700°C), which is similar to the activation energy for surface diffusion, but much lower than that for bulk diffusion.³⁵ The researchers suggested that carbon diffusion on the catalyst surface is the rate-determining step in nanofiber growth at low temperature. The graphitic basal planes form on the surface of the catalyst surface, thus the carbon layers of the nanofibers are parallel to the metal surface, i.e., exhibit platelet stacking.

The surface diffusion mechanism explains the platelet stacked structure of the nanofibers deposited at low temperatures, 750°C. With an increase in the deposition temperatures, the solubility of C in Ni increases, and bulk diffusion becomes faster. Thus there is a transition at the point where growth is controlled by bulk diffusion through the Ni. Above this point (temperature), herringbone or tubular stacked carbon forms.

Boron concentration influences the stacked texture as well. When boron concentration in graphitic carbon is high (>15%), boron atoms exist as both substitutional and interstitial species.¹¹ The platelet stacked structure is well-ordered, and has the same interlayer spacing as graphite crystal (0.335 nm), but the interlayer spacing in nanotubes (or tubular texture) might be larger because of the curvature of the cylindrical graphene layers.^{36,37} The latter texture has a higher capacity to accommodate boron atoms as the concentration of defects in the structure. When the concentration of boron in the reactant source is high, more boron atoms would be introduced into the carbon structure as either substitutional or interstitial species. For this reason, a tubular texture is preferred for doping. From this point, the nanofibers are inhomogeneous not only in the context of structure, but in terms of boron atom distribution as well. In the following section we will study the structure-related chemistry in a single nanofiber using high-resolution EELS operated on a STEM microscope, which is an investigation into the boron-doped carbon nano-form structure on the atomic level.

6.3.2 Structure-related Chemistry Analysis of Boron-doped Carbon Nanofibers

6.3.2.1 A Background of EELS in Conjunction with Z-contrast Imaging

The technique of Z-contrast imaging in STEM was achieved by Pennycook and Browning at Oak Ridge National Laboratory in the early 1990's.^{38,39} A schematic diagram of Z-contrast imaging is given as Figure 6.15. In this technique, a finely focused beam with a convergent angle of ~ 10 mrad is used as the electron probe. The atomic columns of the thin specimen are illuminated as the probe scans across the specimen, generating a two-dimensional intensity map of scattered electrons at the annular detector, where the atomic positions always appear to be bright. Using the high-angle annular dark-field detector ($> \sim 50$ mrad at 200 kV) makes thermal diffuse scattering the dominant contribution to the detected intensity, and allows one to consider each atom as scattering independently with a cross-section that approaches the value of Z^2 , and is thus directly sensitive to the atomic number(s) of the atoms probed. Due to the Z^2 dependence, the number of electrons scattered by the sample is directly related to the composition. Because atoms of higher atomic number, or Z , scatter more electrons, they produce a brighter image. This technique is termed Z-contrast imaging because, although atoms are always white in the image, the heavier an atom is, the whiter it appears.^{38,39}

The Z-contrast image itself has chemical sensitivity but cannot identify unknown chemical species. Because only those electrons scattered through large angles are used for the Z-contrast imaging, the rest of the electrons may be analyzed by an electron spectrometer. This measures the energy loss that occurs when the electrons pass through the specimen. This technique, namely, electron energy loss spectroscopy (EELS), can

identify unknown chemical species from the fingerprint of energy loss. Since the two techniques do not interfere with each other, Z-contrast images can be used to accurately position the electron probe at the desired spot on the sample and to acquire EELS spectra.⁴⁰

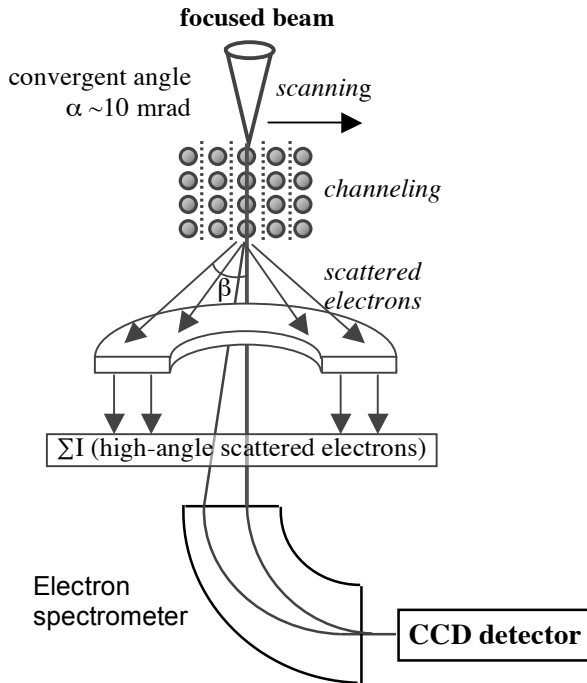


Figure 6.15. Schematic diagram of the Z-contrast imaging using high-angle scattering and EELS in STEM. Adapted from Browning *et al.*³⁸

6.3.2.2 EELS Analysis of Boron-doped Carbon Nanofibers

The boron-doped carbon nanofibers of Sample I-1 (Figure 6.8) and Sample II-750C (Figure 6.10 and 6.11) are analyzed by EELS. The nanofibers of Samples I-1 have two textures along the fiber axis, herringbone stacked in the core, and tubular stacked outside. Between the two textures, there is a disorder transition area that has turbostratic carbon structure. The nanofibers of Samples II-750C have a platelet stacked structure in the core, and disordered tubular stacked structure in the outside regions. We have opted to use the EELS line scan technique to probe the boron atom distribution across the nanofibers, with the aim to understand the influence of the structure on the boron atom distribution in the inhomogeneous nanofibers.

6.3.2.2.1 Nanofibers of Sample I-1

Figure 6.16 show a Z-contrast image of nanofibers in Sample I-1. Atoms are white in a Z-contrast image. The bright white area on the right bottom in Figure 6.16 is caused by the large sample thickness. A nanofiber has a diameter of ~50 nm and a length of 200 nm sitting at the sample edge. In the middle of the nanofiber, dark triangles run along the axis, which are the hollow conical compartments built up by the herringboned carbon layers, as shown in Figure 6.8c. We picked up paths in the perpendicular direction across this nanofiber to carry out EELS line scans. Scan A crosses a central dark triangle, and Scan B touches the tip of a dark triangle, as shown in Figure 6.16.

The integration intensity profiles of B, C and O K-edges by Scan A and Scan B are shown in Figure 6.17. Since the experimental parameters to run the EELS analysis are

constant, the integration intensity of a particular element is a function of the atom density (n_x) and the sample thickness (t), as given in Equation 6.3. Oxygen signals are very low. Boron signals by both Scan A and Scan B are similar, and the maximum values lie at the position between the surface and the axial center. Shapes of carbon signals are approximately symmetrical with respect to the nanofiber axis, and concave at the axial center. During Scan A, the width to cross the central hollow cone is about 16 nm, which means the actual thickness of sample reacted with the electron probe is less in the center because of the cylindrical shape of the fiber. Thus, the carbon profile from Scan A comes out with two maxima instead of a maximum at the axial center as a solid carbon fiber would. Scan B touched a tip of the hollow cone, so only has a small drop in the carbon intensity at the center.

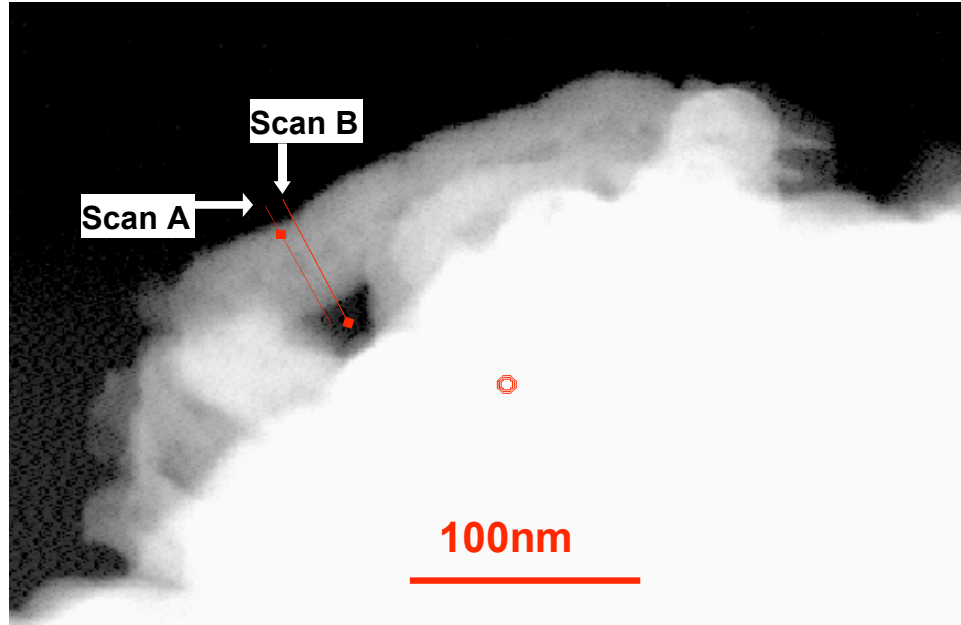
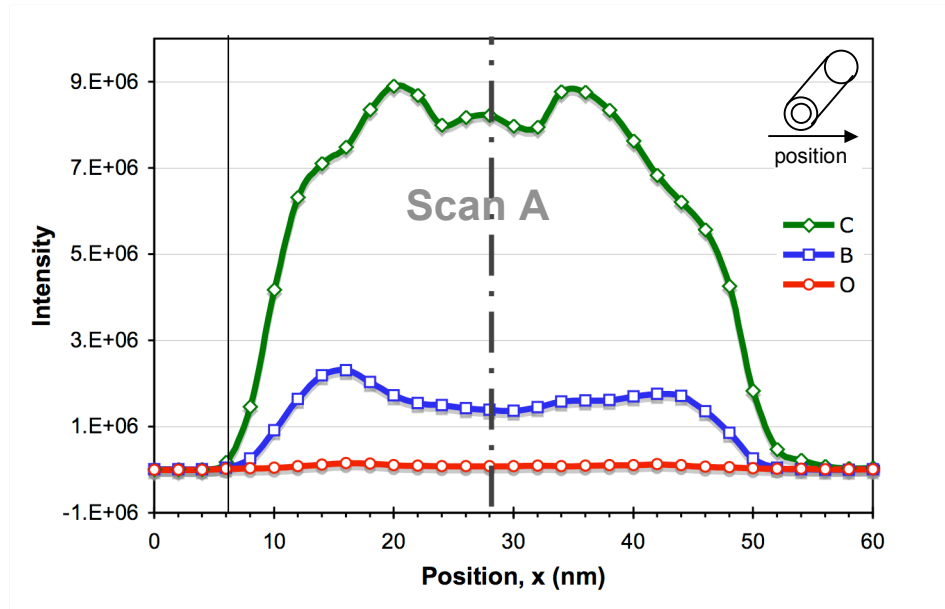
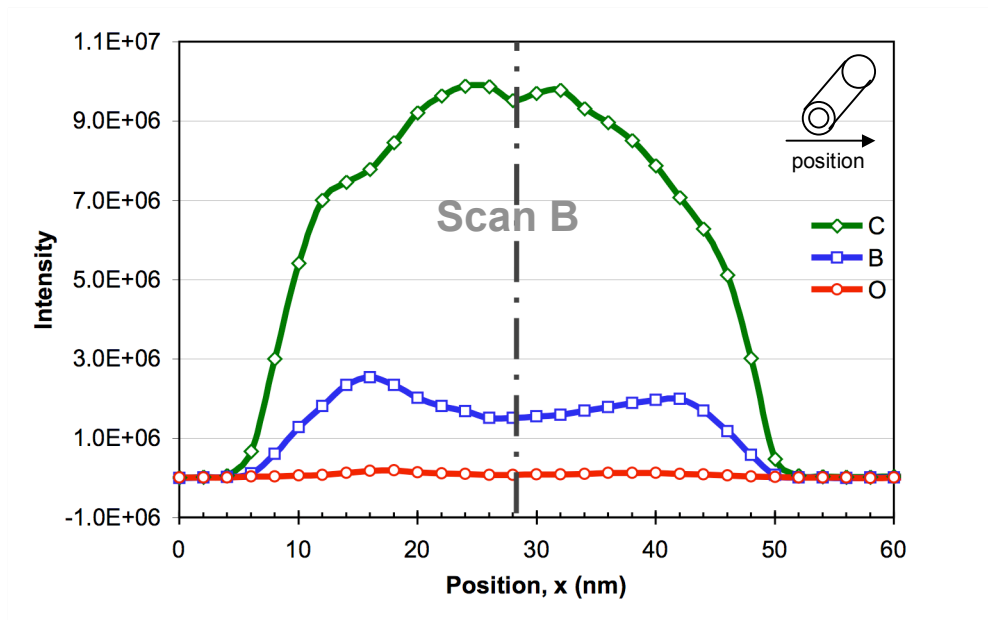


Figure 6.16. A Z-contrast image of a nanofiber with a diameter of 60 nm in sample I-1. Two EELS line scan paths across the nanofiber are labeled as Scan A and Scan B, respectively.



(a)

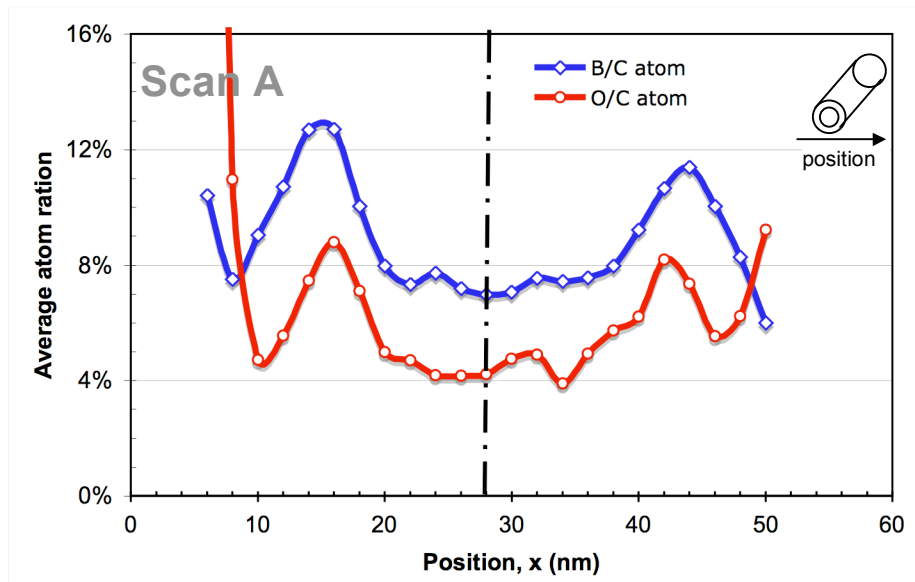


(b)

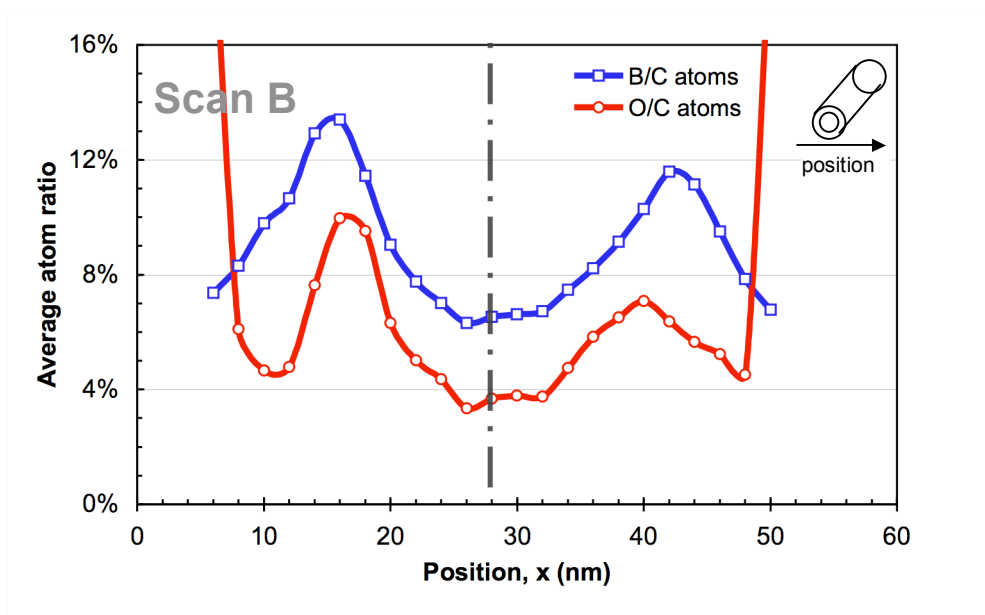
Figure 6.17. The integration intensity profiles of B, C and O K-edges of (a) Scan A and (b) Scan B perpendicular across a nanofiber in Sample I-1. The dash lines represent the nanofiber axis.

The average atom ratios of B/C and O/B are calculated using the integration intensity profiles, and are shown as position profiles in Figure 6.18. The asymmetry in the profile shape is attributed to the variations in the atom (B and O) distribution, and the shape imperfection of the nanofiber. In order to simplify the discussion, the asymmetry in the atom ratio profiles with respect to the nanofiber axis is ignored, and we will only look into the EELS results on the left side of the nanofiber axis in the profiles.

As shown in Figure 6.18, boron atoms are not uniformly distributed in the nanofiber of Sample I-1. B/C average ratios in the nanofibers are between 6-13%. The highest B/C average ratio appears at a position away from the axial center ~ 12 nm. The profiles of the O/C ratio have the same shape as those of the corresponding B/C ratio. O/C average ratios are calculated to be more than 4%, and have very high values ($>16\%$) on the nanofiber surface. In the body of the nanofiber, O/C average ratio profile peaks at 9-10% at the same position as the B/C peak. The O/C ratio of Sample I-1, measured by XPS (3.7%), or by AES (2.5%), are much lower than that analyzed by EELS. In the EELS analysis, small O/C ratio values are often magnified when using Equation 6.4 because the relatively small oxygen partial ionization cross-section ($\sigma_C/\sigma_O = 4.3$ in our case). Another inaccuracy in O/C ratios is caused by the very low oxygen integration intensity (Figure 6.16), and the resulting low signal-to-noise ratio. We suggest not using O/C ratios to represent the actual oxygen content for the sample. However, the similar shapes of the profiles between the B/C ratio and the O/C ratio imply that the boron-doping process involves a reaction with a small amount of oxygen, which may originate from the fused quartz substrates.



(a)



(b)

Figure 6.18. The profiles of average atom ratios of B/C and O/C of (a) Scan A and (b) Scan B. The dash lines represent the nanofiber axis.

The EELS analysis is undertaken using STEM, so every spectrum of EELS includes chemical information of the sample of the specific thickness the electron beam goes through. As for a nanofiber sample with a cylindrical shape, each detection in Scan A or Scan B consists of the information along the path of the electron beam from the upper surface into the body, and finally out of lower surface of the nanofiber. The boron atom distribution in the nanofiber is not uniform, and the profiles of B/C ratios in Figure 6.18 do not show the actual B/C ratio value at the radial position.

In order to find out the actual boron distribution in a nanofiber, we carry out a calculation using a geometric model of nanofiber. Figure 6.19 shows the models of the nanofiber cross-section for Scan A and Scan B. There are four assumptions employed when developing the models:

1. The nanofiber has perfect axial symmetry.
2. Carbon atoms are homogeneously distributed throughout the cross-section, i.e., the carbon concentration (n_C) is assumed to be constant.
3. The cross-section is divided into concentric rings, 2 nm thick, which are the same size as the EELS scanning step size.
4. Boron atom distribution is different between rings, but the same within one ring.

The shape of the models is built up based on the carbon integration intensity profiles in Figure 6.17. For Scan A, the outer diameter is 22 nm and inner diameter is 8 nm (Figure 6.19a). For Scan B, the outer diameter is also 22 nm, but inner diameter is only 2 nm (Figure 6.19b).

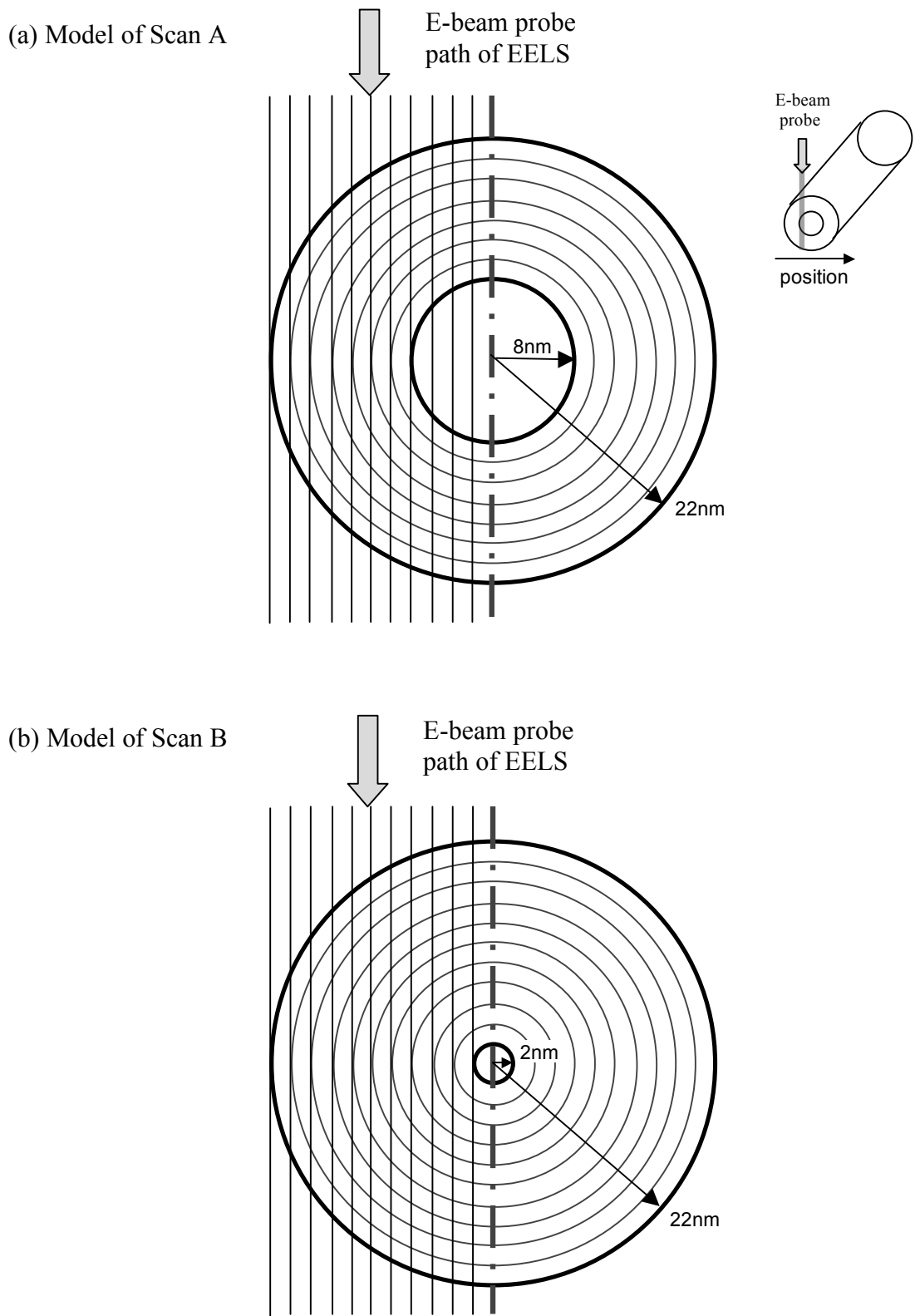


Figure 6.19. Nanofiber cross-section models built up based on the carbon profiles for (a) Scan A and (b) Scan B of a nanofiber in Sample I-1.

With these models, the boron and carbon integration intensity expressed by Equation 6.3 can be written as:

$$I_B = I_{ZL} \cdot \sigma_B \cdot \sum_i (n_{B,i} \cdot t_i) \quad (6.8)$$

$$I_C = I_{ZL} \cdot \sigma_C \cdot n_C \cdot t \quad (6.9)$$

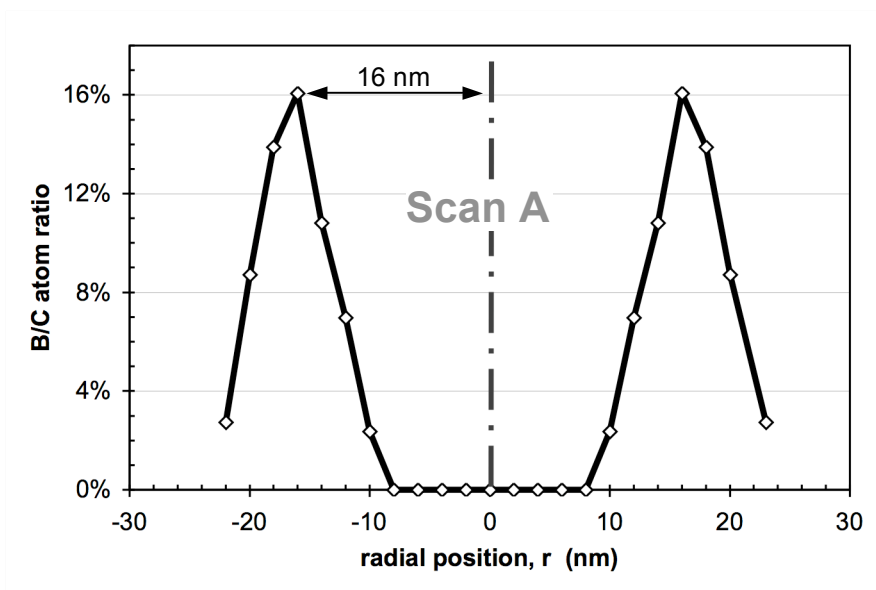
where i is the ring number, $n_{B,i}$ is the boron concentration in the i th ring, and t_i is the thickness that the electron probe goes through in the i th ring, respectively. The total thickness t equals $\sum_i t_i$, where t_i can be calculated according to the models in Figure 6.19.

Since n_C is a constant, then $n_C = n_{C,i}$ at any ring. We derive the relationship as:

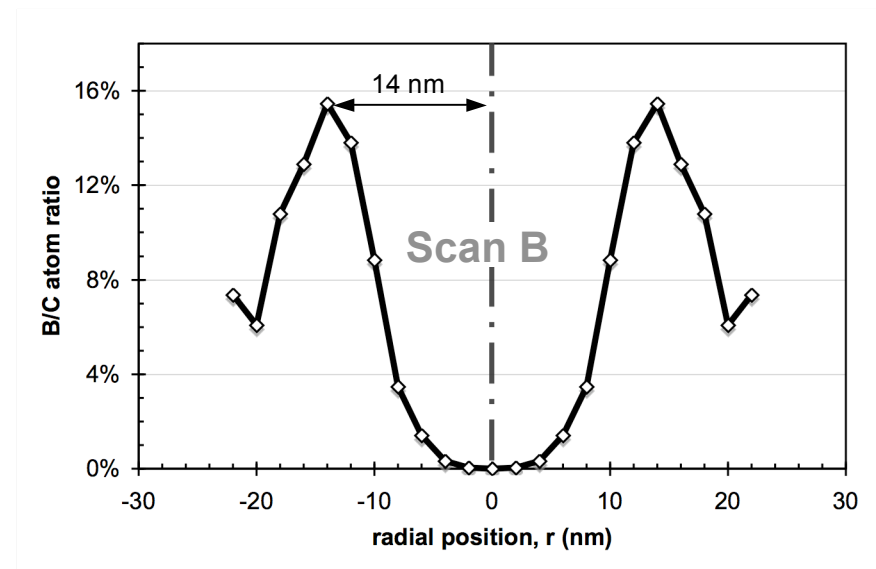
$$\sum_i \left(\frac{n_B}{n_C} \right)_i \cdot \left(\frac{t_i}{t} \right) = \frac{I_B}{I_C} \cdot \frac{\sigma_C}{\sigma_B} \quad (6.10)$$

where t is the total thickness of the sample, and $\left(\frac{n_B}{n_C} \right)_i$ denotes the B/C atom ratio in the i th ring. The results of $\left(\frac{n_B}{n_C} \right)_i$ represent the boron distribution in the nanofiber, as given in Figure 6.20.

The profile shapes of calculated B/C atom ratios from Scan A and Scan B in Figure 6.20 are similar. Both profiles have a maximum peak of 16% B/C at the position of 14-16 nm away from the axial center. Discrepancies occur at the surface and the central position of the nanofiber. At the surface, both carbon and boron integration intensity are low due to the low sample thickness, thus a high variation in I_B/I_C is possible. The difference in the center part is due to the cross-section difference (Figure 6.19): Scan A crosses a hollow cone while Scan B does not. The calculated B/C ratio profiles of Scan A and Scan B are in good agreement with the boron distribution in the nanofiber of sample I-1.



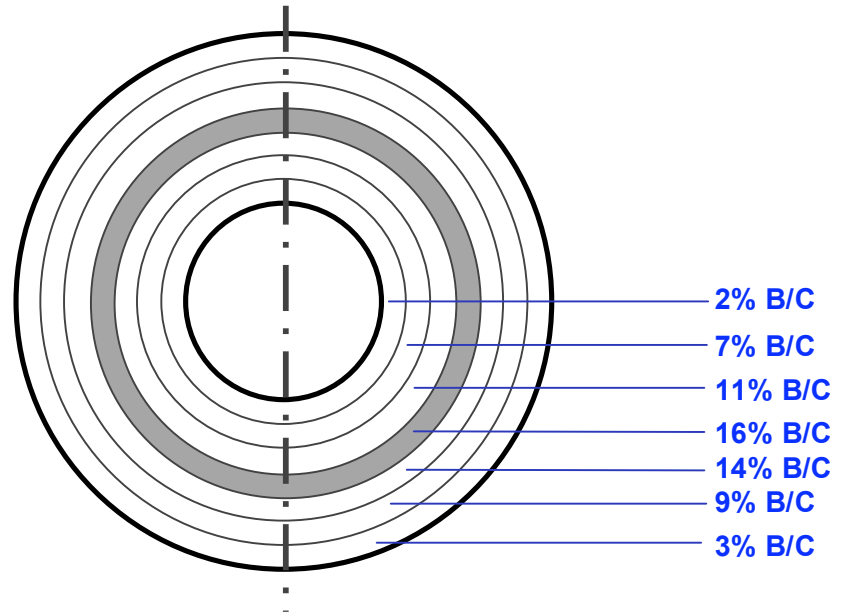
(a)



(b)

Figure 6.20. The profiles of calculated B/C atom ratios based on the nanofiber models of (a) Scan A and (b) Scan B. The dash lines represent the nanofiber axis.

(a) Model of Scan A



(b) Model of Scan B

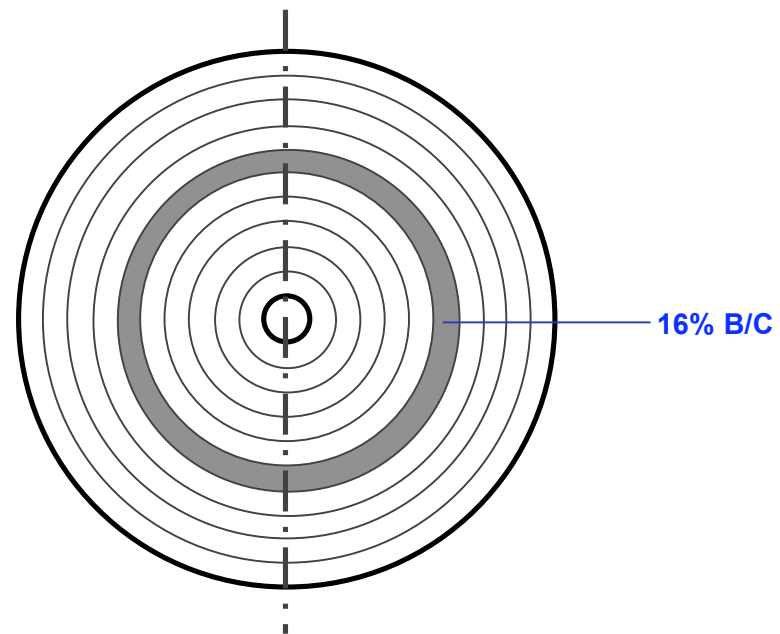


Figure 6.21. Models of boron distribution in the nanofiber of Sample I-1. (a) Model of Scan A, and (b) model of scan B. The areas highlighted in gray have the highest boron concentration of 16% B/C.

Based on the cross-section models, boron distribution in the nanofiber of Sample I-1 are displayed in Figure 6.21. The highlighted ring in each cross-section model represents the area having the highest B/C atom ratio of 16%, where the boron-doped carbon formula is C_6B .

6.3.2.2.2 Nanofibers of Sample II-750C

A Z-contrast image of nanofibers in Sample II-750C is shown in Figure 6.22. A nanofiber with a diameter of ~ 80 nm is selected to run the EELS line scan, whose path is along the red line. This nanofiber is solid, and its structure is similar to the nanofiber in Figure 6.10. Figure 6.23 shows the integration intensity profiles of B and C K-edges by Scan C. Both profiles are symmetric with respect to the axis. As expected, carbon profile has the maximum at the center line because the fiber is not hollow. The boron profile has two maxima at the positions of $x=30$ and 66 nm, where both are away from the axis position ($x=48$ nm) for 18 nm. It indicates that the boron atom concentration is the greatest at, or near, the position away from the axis for 18 nm.

The profile of average B/C atom ratios is calculated using Equation 6.4, and is given in Figure 6.24. The asymmetry in the profile shape is attributed to the variations in the boron atom distribution, and the shape imperfection of the nanofiber. Boron atoms are not uniformly distributed in the nanofiber of Sample II-750C. B/C average ratios in the nanofibers are between 5-10%. The values are very low in the center, and stay at 8-10% in the external part. There is a fluctuation at the positions close to the surface. Again, because of the transmission electron probe used for EELS, the profile of B/C average

ratios in Figure 6.24 does not represent the radial boron distribution in the nanofibers.

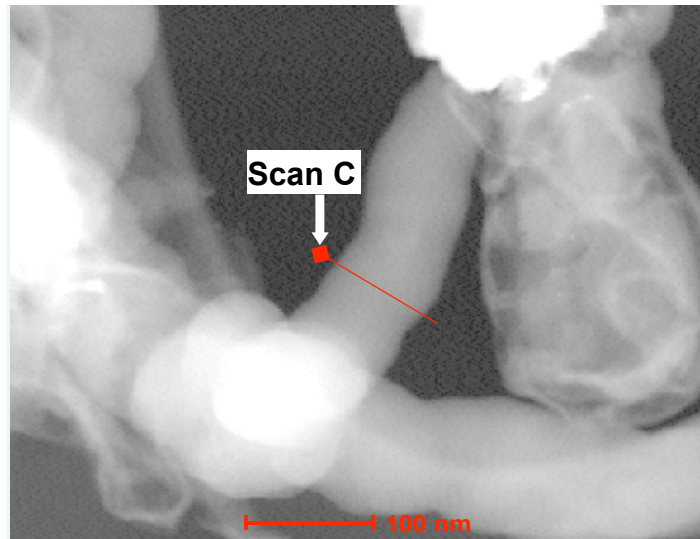


Figure 6.22. A Z-contrast image of a nanofiber with a diameter of 80 nm in sample II-750C. An EELS line scan path across the nanofiber is labeled as Scan C.

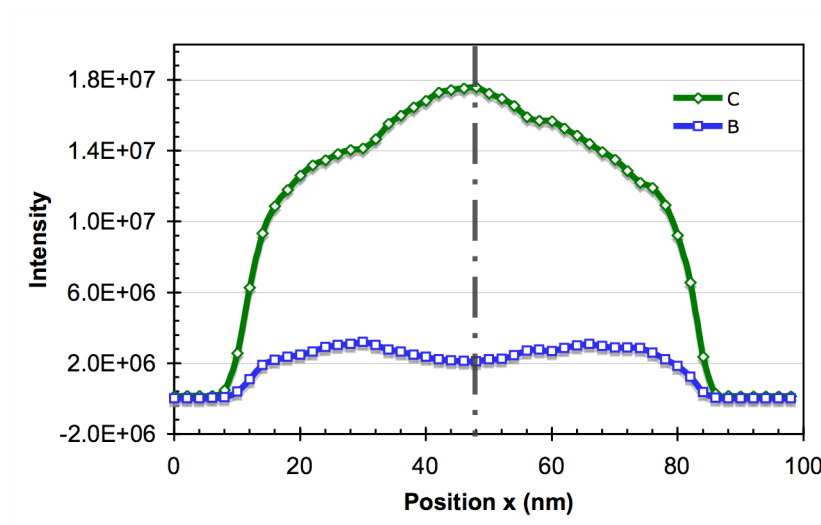


Figure 6.23. The integration intensity profiles of B and C K-edges of Scan C across a nanofiber in Sample II-750C. The dash lines represent the nanofiber axis.

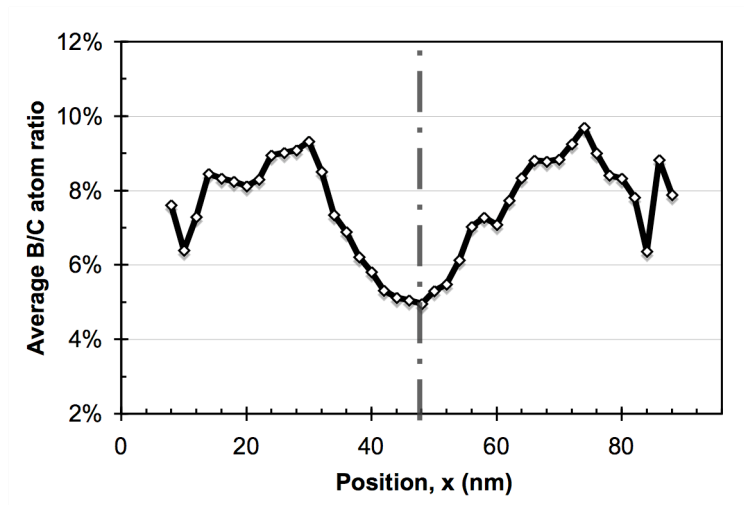
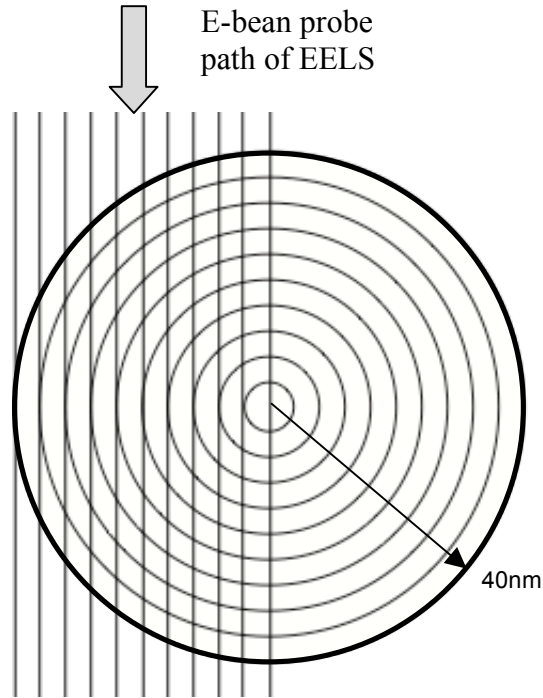


Figure 6.24. The profile of average B/C atom ratio of Scan C on a nanofiber in Sample II-750C. The dash line represents the nanofiber axis.

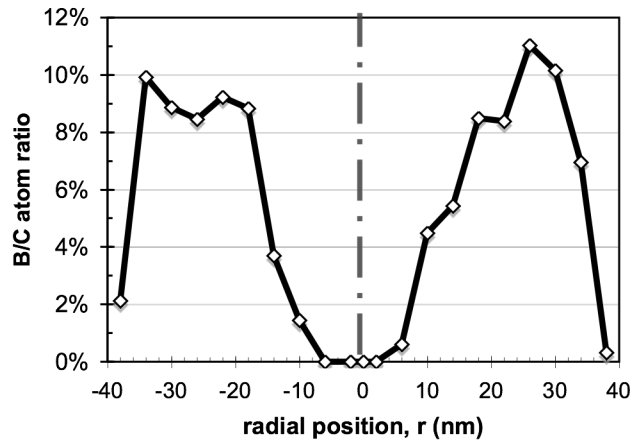
In order to find out the radial boron distribution in the nanofiber, a geometric model of the nanofiber cross-section is built up based on four assumptions. These four assumptions are similar to those made in section 3.2.1:

1. The nanofiber has axial symmetry.
2. Carbon atoms are homogeneously distributed in the cross-section.
3. The cross-section is divided into concentric rings, 4 nm thick.
4. Boron atom distribution is different between rings, but the same within one ring.

The diameter of the cross-section of Scan C is identified to be 80 nm from the carbon integration profile in Figure 6.23. A cross-section model of the nanofiber in Sample-II-750C is shown in Figure 6.25a. Based on this model and boron and carbon integration intensity profiles, B/C atom ratios versus radial position are calculated using Equation 6.10, and shown in Figure 6.25b.



(a) Nanofiber cross-section model based on the carbon profile for Scan C on a nanofiber in Sample II-750C.



(b) The profile of calculated B/C atom ratios based on the nanofiber model of Scan C.

Figure 6.25. (a) The nanofiber model and (b) calculated radial boron distribution in a nanofiber of Sample II-750C.

The profile of B/C atom ratios represents the radial boron distribution in the nanofibers in Sample II-750C. The shape of this B/C profile exhibits some different features compared to those in Figure 6.20, which belong to sample I-1. The B/C atom ratio is very low in the central part of the nanofiber ($< 2\%$ for radius $r < 10$ nm). There is a rapid increase in the B/C atom ratio to $\sim 8\%$ with an increase in radius from 10-18 nm. Thereafter the B/C ratios are relatively stable at 8-10% between a radius of 18 and 34 nm. The B/C ratio on the surface is calculated based on low boron/carbon integration intensities (due to the low sample thickness), and so are not very reliable. The radial boron distribution is closely related with the structure of the nanofiber in Sample II-750. The following section, we will discuss the relationship between the chemistry and the structure of the boron-doped carbon nanofibers.

6.3.2.3 Structure-related Chemistry in Boron-doped Carbon Nanofibers

The boron distribution from EELS analysis displays a close relationship with the structure in the nanofiber. Figure 6.26 shows a high-resolution TEM image of a nanofiber in Sample I-1. In this nanofiber, there are ordered herringbone stacked carbon-rich structures in the core, and ordered tubular stacked structures in the external regions. Between these two textures, a disordered transition area (~ 5 layers thick) is present, and coincides with the highest B/C atom ratio (16%, C_6B). The disordered stacking in the transition area indicates that with such a high boron concentration, a combination of substitutional and interstitial doping occurs during the nanofiber growth.

The high-resolution TEM image of a nanofiber in Sample II-750C is given in Figure 6.27. There are well-ordered platelet stacked carbon-rich structures in the core, and turbostratic tubular stacked carbon in the external regions. A transition between these two textures occurs quickly, only 2-3 layers thick, as shown in Figure 6.27b. These regions apparently are correlated with the boron concentration (see Figure 6.25b). The B/C atom ratio is low ($< 2\%$) in the central platelet stacked texture, while it stays at 8-10% in the external turbostratic tubular stacked texture.

In summary, three structural types, platelet, herringbone and tubular, exist in the boron-doped carbon nanofibers. It is shown that the boron atom distribution has a direct influence on the local structure. Platelet stacked structures exist as highly ordered regions with correspondingly low boron concentration ($< 2\%$ B/C). Herringbone structures, while ordered, possess relatively low boron concentration (2-8% B/C). Tubular structures occur either as ordered regions of low boron concentration (ratio of 3-8% B/C), or turbostratic with a B/C ratio in excess of 8%. A disordered transition area dividing herringbone and tubular structured regions in a nanofiber of Sample I-1 is observed where a B/C atom ratio of 16%, i.e., a composition of C_6B is present.

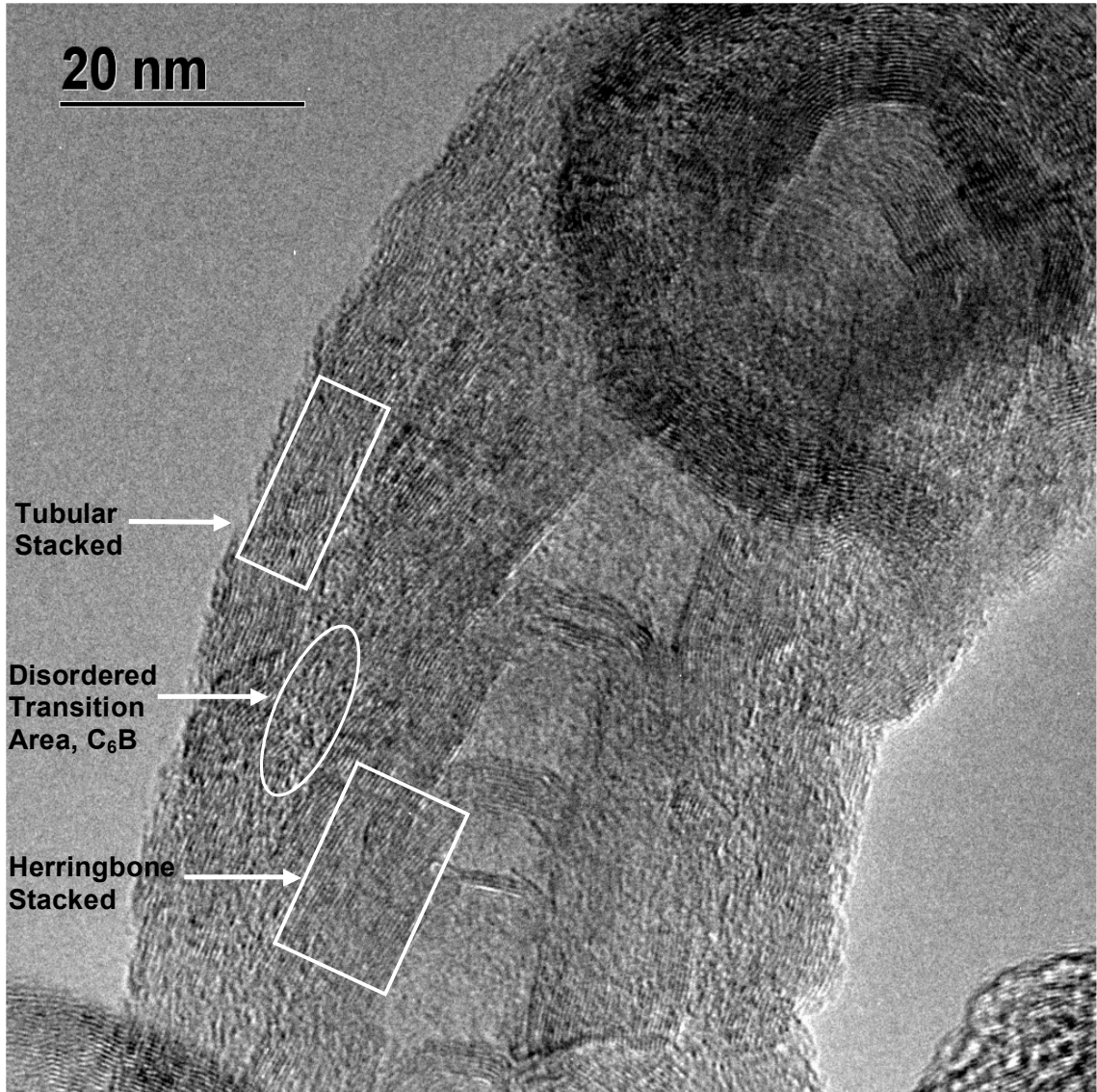


Figure 6.26. The relationship between the structure and the boron distribution in a nanofiber of Sample I-1.

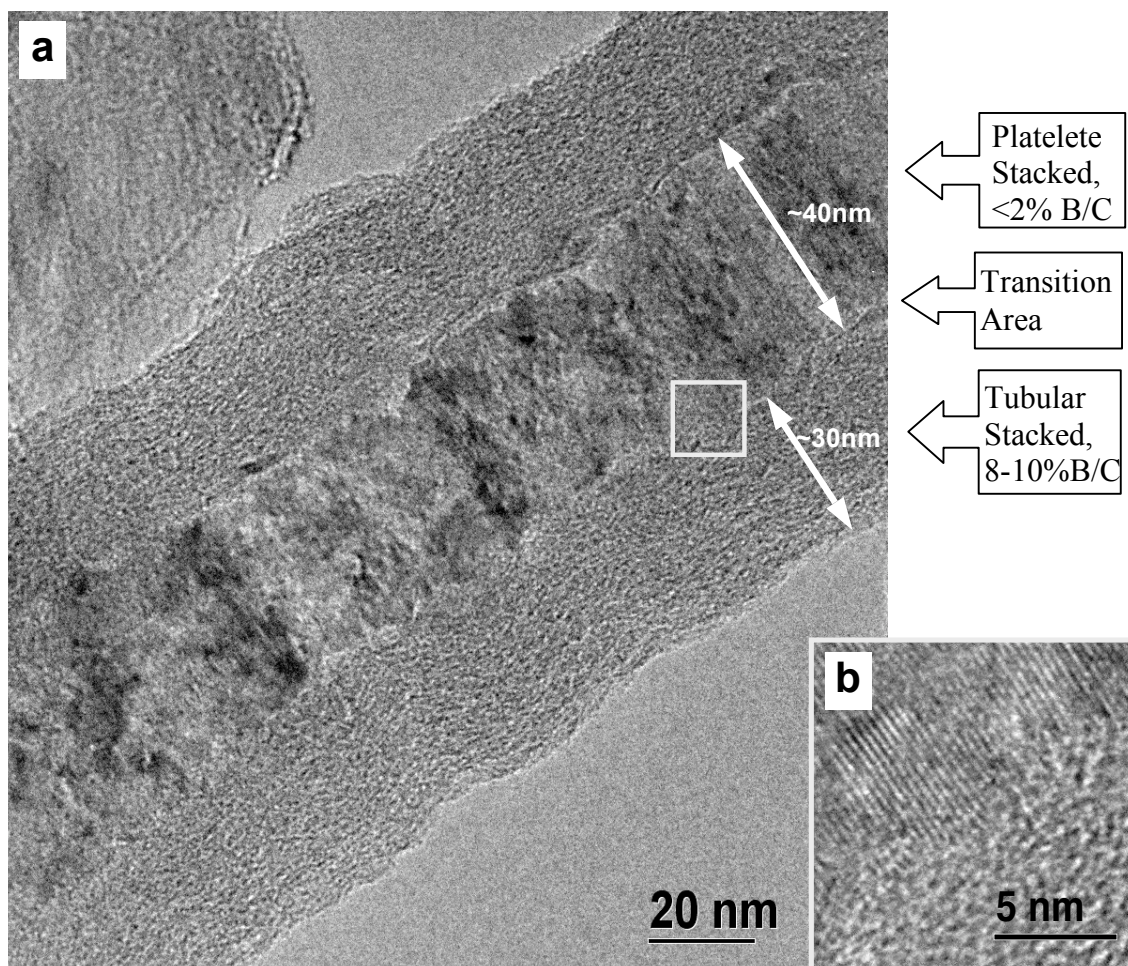


Figure 6.27. The relationship between the structure and the boron distribution in a nanofiber of Sample II-750. (a) The high-resolution TEM image of a nanofiber, and (b) a magnified image of the transition area between two textures of the nanofiber structure.

6.3.3 Growth Mechanism of Boron-doped Carbon Nanofibers

Many of the existing models for CVD growth of carbon nanotubes and nanofibers are based on the bulk diffusion mechanism first proposed by Baker *et al.*⁴¹ The hydrocarbon molecules decompose at the catalyst surface and the carbon atoms dissolve into the metal. The dissolved carbon diffuses through the metal particle, and precipitates at the other opposite surface of the particle to form the body of the carbon filament. Baird *et al.*⁴² and Oberlin *et al.*⁴³ proposed another common growth mechanism involving the surface diffusion instead of bulk diffusion. The carbon atoms diffuse over the catalyst surface to form tubular structure that emanates from the circumference of the catalyst. They suggested that tubular structure is favored for carbon filaments with very small diameter because it decreases the total energy by reducing the number of dangling bonds. Hofmann *et al.*³⁴ proposed a surface diffusion mechanism for the low-temperature growth of carbon nanotubes and nanofibers by plasma-enhanced CVD based on a study of the activation energy for the growth rate. They found that the nanofibers are platelet stacked grown at low temperature.

We propose that both surface diffusion and bulk diffusion mechanisms are involved to form the boron-doped nanofibers. Temperature determines the growth mechanism by either surface diffusion or bulk diffusion. We have demonstrated the basic growth mode in Section 4.3.5. Figure 6.28 is a schematic presentation of the mechanisms involved with the boron-doped carbon nanofibers. At low temperature (750°C), surface diffusion dominates, thus platelet stacked structure exists in the core (Figure 6.28a). The Ni particles have higher curvature on the circumference, where carbon diffuses and

precipitates at higher rates compared to the middle surface. Consequently, a tubular structure grows along the circumference of the Ni particles, which also helps to terminate the dangling bonds on the platelet stacked layers. Thus, the nanofiber has two textures: well ordered platelet stacked in the core and disordered tubular structure on the outside. At high temperature ($\sim 900^{\circ}\text{C}$), bulk diffusion governs the nanofiber growth, and results in a tubular structure (Figure 6.28c). Because of the high curvature on the circumference of the Ni particles, two textures also appear: ordered tubular in the core and disordered tubular on the exterior. At intermediate temperatures ($\sim 800^{\circ}\text{C}$), both surface diffusion and bulk diffusion influence the carbon transport and precipitation that ultimately leads to the growth of herringbone structure in the core (Figure 6.28b).

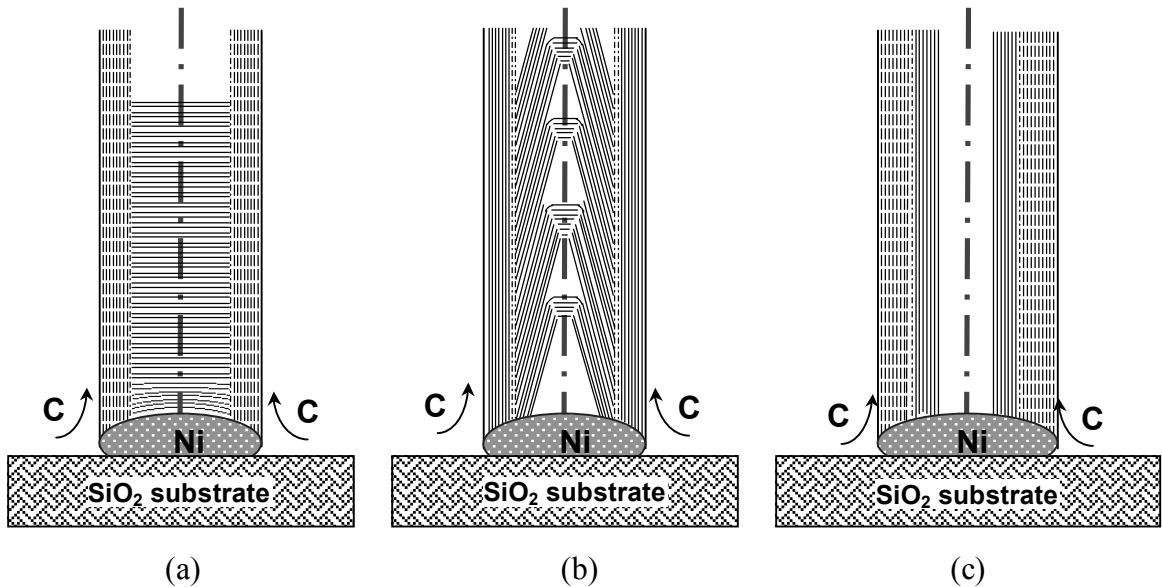


Figure 6.28. Schematic representation of the mechanism of boron-doped carbon nanofiber formation. (a) The formation of platelet stacked structure at low temperature, (b) the formation of herringbone structure at intermediate temperature, and (c) the formation of tubular structure at high temperature. Solid lines represent the ordered carbon layers, while dashed lines represent turbostratic carbon layers.

The dangling bonds at the edge of herringbone carbon are terminated by the tubular stacked carbon grown along the circumference of Ni particles.

The doping of boron atoms influences the ordering of the carbon layer stacking. Well ordered stacking, such as platelet carbon, has a very low boron concentration. On the other hand, carbon layers are disordered at the transition area between two textures where the boron concentration reaches ~16% B/C in Sample I-1. In addition, very high reactant ratios ($\text{BCl}_3/\text{C}_6\text{H}_6$) modify the stacked texture of the nanofibers. For example, there are nanotubes of 15-30 nm synthesized in Sample I-2 (18.4 at.%B). The high concentration of BCl_3 might change the surface properties of the Ni film, and modify the fragmentation of Ni film into nanoparticles. Smaller Ni particles naturally favor the formation of nanotubes.

6.4 Conclusions

The crystal structure of these nanofibers is inhomogeneous, and has mixed crystallite sizes of both L_a and L_c . XRD analysis reveals that boron-doped carbon nanofibers are highly orientated, and have a graphite-like structure. The interlayer spacings, d_{002} , range from 0.3343 to 0.3397 nm, and crystallite sizes, L_c (002), range from ~5 to 20 nm. The interlayer spacings increase, and the crystallite sizes decrease with an increase in deposition temperature. In addition, strains occur in the samples synthesized at low temperature (750°C), and lead to a small lattice parameter, d_{002} . Raman analysis reveals that lower deposition temperatures favor the growth of large crystallites along the c -axis, while higher deposition temperatures affect an increase in the planar crystallite width. The crystallite width (L_a), by Raman analysis, is in the range of 2.5-4.5 nm.

The nano-scaled structure shown by TEM is inhomogeneous. Submicron fibers and nanofibers coexist in each sample. The diameters of both the submicron fibers and nanofibers decrease with an increase in reactant ratio, $\text{BCl}_3/\text{C}_6\text{H}_6$. An increase in deposition temperature not only increases the diameters of submicron fibers or nanofibers, but also changes the texture of the filamentous carbon. The change in texture of filamentous carbon can be described as: (1) an increase in boron concentration causes the texture to transform from herringbone to tubular form; (2) an increase in deposition temperature helps to change the texture from platelet form to tubular form.

EELS analysis reveals that the boron doping into the carbon nanofibers is structure-related. The platelet stacked structure is always very well-ordered with very low boron

concentration ($< 2\%$ B/C). Herringbone structures are ordered with relatively low boron concentration (2-8% B/C). The tubular structure is either ordered with a B/C ratio of 3-8% B/C, or turbostratic with a B/C ratio of $> 8\%$. A disordered transition area between herringbone and tubular structure in a nanofiber of Sample I-1 is observed where the boron concentration is 16%, i.e., consistent with a composition of C_6B .

Finally, mechanisms of boron-doped nanofiber growth are proposed that involve both surface diffusion and bulk diffusion process. Temperature is the governing factor that determines the process by which either surface diffusion or bulk diffusion dominates. Boron doping also influences the ordering of the carbon layer plane stacking.

References

1. K.B. Teo, C. Singh, M. Chhowalla, and W.I. Milne, "Catalytic Synthesis of Carbon Nanotubes and Nanofibers," pp. 1-22 in *Encyclopedia of Nanoscience and Nanotechnology*, Vol. 10. Edited by H. S. Nalwa. American Scientific, New York, 2003. Available at http://www-g.eng.cam.ac.uk/cnt/papers/ken_enn.pdf
2. R.T.K. Baker, "Catalytic Growth of Carbon Filaments," *Carbon*, 27 [3] 315-23 (1989).
3. M. Endo, "Grow Carbon Fibers in the Vapor Phase," *Chemtech*, 18 [9] 568-76 (1988).
4. N.M. Rodriguez, "A Review of Catalytically Grown Carbon Nanofibers," *J. Mater. Res.*, 8 [12] 3233-50 (1993).
5. N.M. Rodriguez, A. Chambers, and R.T.K. Baker, "Catalytic Engineering of Carbon Nanostructures," *Langmuir*, 11 [10] 3862-66 (1995).
6. C.A. Bessel, K. Laubernds, N.M. Rodriguez, and R.T.K. Baker, "Graphite Nanofibers as an Electrode for Fuel Cell Applications," *J. Phys. Chem. B*, 105 [6] 1115-18 (2001).
7. L. Kieffer, R. McKenzie, C.R. Hubbard, C. Robbins, and W. Wong-Ng, "National Bureau of Standards Certificate: Standard Reference Material 640b," National Bureau of Standards, Gaithersburg, MD, 1987.
8. R. Jenkins and R.L. Snyder, *Introduction to X-Ray Powder Diffraction*; pp. 89-91. John Wiley, New York, 1996.
9. P.A. Throver, D.C. Nagle, and W.S. Horton, "The Anisotropy of Pyrolytic Graphite," *J. Appl. Crystallogr.*, 6 [5] 347-51 (1973).
10. R. Brydson, *Electron Energy Loss Spectroscopy*; pp. 69-78. BIOS Scientific, Oxford, UK, 2001.
11. C.T. Hach, L. E. Jones, C. Crossland, and P.A. Throver, "An Investigation of Vapor Deposited Boron Rich Carbon - A Novel Graphite-Like Material - Part I: The Structure of BC_x (C₆B) Thin Films," *Carbon*, 37 [2] 221-30 (1999).
12. R.E. Franklin, "The Structure of Graphitic Carbons," *Acta Crystallogr.*, 4 [3] 253-61 (1951).
13. A. Oberlin, "High-Resolution TEM Studies of Carbonization and Graphitization," pp. 1-143 in *Chemistry and Physics of Carbon*, Vol. 22. Edited by P. A. Throver. Dekker, New York, 1989.

14. J.Y. Howe, C.J. Rawn, L.E. Jones, and H. Ow, "Improved Crystallographic Data for Graphite," *Powder Diffr.*, 18 [2] 150-54 (2002).
15. P.L. Walker, L. Austin, and J. Tietjen, "Oxygen Chemisorption Effects on Graphite Thermoelectric Power," pp. 327-65 in *Chemistry and Physics of Carbon*, Vol. 1. Edited by P. L. Walker. Dekker, New York, 1965.
16. B.T. Kelly, *Physycs of Graphite*; p. 80. Applied Science, London,UK, 1981.
17. A. Cuesta, P. Dhamelincourt, J. Laureyns, A. Martinez-Alonso, and J.M.D. Tascon, "Comparative Performance of X-Ray Diffraction and Raman Microprobe Techniques for the Study of Carbon Materials," *J. Mater. Chem.*, 8 [12] 2875-79 (1998).
18. T. Jawhari, A. Roid, and J. Casado, "Raman Spectroscopic Characterization of Some Commercially Available Carbon Black Materials," *Carbon*, 33 [11] 1561-65 (1995).
19. D.S. Knight and W.B. White, "Characterization of Diamond Films by Raman Spectroscopy," *J. Mater. Res.*, 4 [2] 385-95 (1989).
20. R. Escribano, J.J. Sloan, N. Siddique, N. Sze, and T. Dudev, "Raman Spectroscopy of Carbon-Containing Particles," *Vib. Spectrosc.*, 26 [2] 179-86 (2001).
21. K. Nakamoto, *Infrared and Raman Spectra of Inorganic and Coordination Compounds*; pp. 153-210. Wiley, New York, 1997.
22. F. Tunistra and J.L. Koenig, "Raman Spectrum of Graphite," *J. Phys. Chem.*, 53 [3] 1126-30 (1970).
23. J.R. Dennison, M. Holtz, and G. Swain, "Raman Spectroscopy of Carbon Materials," *Spectroscopy*, 11 [8] 38-46 (1996).
24. M.J. Matthews, M.A. Pimenta, G. Dresselhaus, M.S. Dresselhaus, and M. Endo, "Origin of Dispersive Effects of the Raman D Band in Carbon Materials," *Phys. Rev. B: Condens. Matter Mater. Phys.*, 59 [10] 6585-88 (1999).
25. P. Lespade, R. Al-Jishi, and M.S. Dresselhaus, "Model for Raman Scattering from Incompletely Graphitized Carbons," *Carbon*, 20 [5] 427-31 (1982).
26. L.H. Robins, E.N. Farabaugh, and A. Feldman, "Line Shape Analysis of the Raman Spectrum of Diamond Films Grown by Hot-Filament and Microwave-Plasma Chemical Vapor Deposition," *J. Mater. Res.*, 5 [11] 2456-66 (1990).

27. T. Hagio, M. Nakamizo, and K. Kobayashi, "Studies on X-Ray Diffraction and Raman Spectra of B-Doped Natural Graphite," *Carbon*, 27 [2] 259-63 (1989).
28. D.L. Fecko, L.E. Jones, and P.A. Throver, "The Formation and Oxidation of BC₃, a New Graphitelike Material," *Carbon*, 31 [4] 637-44 (1993).
29. P.C. Eklund and G.L. Doll, Ch. 4 in *Graphite Intercalation Compounds II: Transport and Electronic Properties*. Edited by H. Zabel and S. A. Solin. Springer Verlag, Berlin, Germany, 1992.
30. A.C. Ferrari and J. Robertson, "Interpretation of Raman Spectra of Disordered and Amorphous Carbon," *Phys. Rev. B: Condens. Matter Mater. Phys.*, 61 [20] 14095-107 (2000).
31. D.V. Badami and G. Kaye, "The Nature of Turbostratic Carbon," *Carbon*, 1 [3] 375 (1964).
32. M.A. Short and J.P.L. Walker, "Measurement of Interlayer Spacings and Crystal Sizes in Turbostratic Carbons," *Carbon*, 1 [1] 3-9 (1963).
33. A. Tanaka, S.-H. Yoon, and I. Mochida, "Preparation of Highly Crystalline Nanofibers on Fe and Fe-Ni Catalysts with a Variety of Graphene Plane Alignments," *Carbon*, 42 [3] 591-97 (2004).
34. S. Hofmann, C. Ducati, J. Robertson, and B. Kleinsorge, "Low-Temperature Growth of Carbon Nanotubes by Plasma-Enhanced Chemical Vapor Deposition," *Appl. Phys. Lett.*, 83 [1] 135-37 (2003).
35. J.F. Mojica and L.L. Levenson, "Bulk-to-Surface Precipitation and Surface Diffusion of Carbon on Polycrystalline Nickel," *Surf. Sci.*, 59 [2] 447-60 (1976).
36. Y. Saito, T. Yoshikawa, S. Bandow, M. Tomita, and T. Hayashi, "Interlayer Spacing in Carbon Nanotubes," *Phys. Rev. B: Condens. Matter Mater. Phys.*, 48 [3] 1907-09 (1993).
37. X. Sun, C.H. Kiang, M. Endo, K. Takeuchi, T. Furuta, and M.S. Dresselhaus, "Stacking Characteristics of Graphene Shells in Carbon Nanotubes," *Phys. Rev. B: Condens. Matter Mater. Phys.*, 54 [18] R12629-32 (1996).
38. N.D. Browning, M.F. Chisholm, and S.J. Pennycook, "Atomic-Resolution Chemical Analysis Using a Scanning Transmission Electron Microscope," *Nature*, 366 [6451] 143-46 (1993).
39. S.J. Pennycook and D.E. Jesson, "High-Resolution Z-Contrast Imaging of Crystals," *Ultramicroscopy*, 37 [1-4] 14-38 (1991).

40. W. Grogger, B. Schaffer, K.M. Krishnan, and F. Hofer, "Energy-Filtering TEM at High Magnification: Spatial Resolution and Detection Limits," *Ultramicroscopy*, 96 [3] 481-89 (2003).
41. R.T.K. Baker, M.A. Barber, P.S. Harris, F.S. Feates, and R.J. Waite, "Nucleation and Growth of Carbon Deposits from the Nickel Catalyzed Decomposition of Acetylene," *J. Catal.*, 26 [1] 51-62 (1972).
42. T. Baird, J.R. Fryer, and B. Grant, "Carbon Formation on Iron and Nickel Foils by Hydrocarbon Pyrolysis--Reactions at 700°C," *Carbon*, 12 [5] 591-602 (1974).
43. A. Oberlin, M. Endo, and T. Koyama, "Filamentous Growth of Carbon through Benzene Decomposition," *J. Cryst. Growth*, 32 [3] 335-49 (1976).

7 Conclusions

This study addresses carbon nanotubes and nanofibers having a high boron concentration (> 10 at.%B). I have built upon our laboratory's experience with the novel form of carbon (C_6B). Additionally, I have used the vast literatures regarding boron-doped carbon nanotube growth, as a reference.

Three difficulties or challenges were surmounted during this study. The first addressed the use of CVD as an effective method to produce boron-doped carbon nanotubes and nanofibers. There is not much in the literature reporting this technique for the synthesis boron-rich carbon nanotubes. The reported results are controversial regarding the boron concentrations and the scale of the filamentous carbon produced. In our work, an extensive investigation of the experimental parameters associated with CVD process has been carried out and the effects of these parameters are demonstrated. A highly boron-rich nanofiber was achieved by the CVD methods described in this thesis.

The second difficulty is the need for accurate measurement of boron concentrations. Boron is a very light element ($Z = 5$) and difficult to assess via many microprobes. XPS and AES are both surface chemistry analysis techniques (5-50 Å deep) and sensitive to boron atoms. The probe size of XPS ($> \sim 10$ μm) is larger than that of AES (which can be small as 10 nm). XPS signals include much information from the surface species that interferes the quantitative analysis. Thus, careful pre-treatment has been taken to remove the surface species before the XPS measuring. Among all the tools, AES is most suitable

to probe boron concentration in nano-scaled structure. We have taken the advantage of the HTML User facility at ORNL and measure boron concentration of the deposited nanofibers by AES. Results by both XPS and AES on the CVD products are in good agreement with boron concentrations of the CVD products in the range between 5-18 at.%.

The third challenge is determining the influence of boron on structure at the atomic level. High-resolution TEM and EELS from HTML User facility help us to address on this issue. Electron probe resolutions of both tools are less than 1 nm, that is, both the structure and chemistry probing are at an atomic level. Based on the observations, a structure-related chemistry that exists in the boron-doped carbon nanofibers is revealed.

The major pieces of knowledge that we have reached in this study are the following:

1. Boron-doped carbon nanofibers with 5-18 at.% boron can be successfully synthesized by a catalytic CVD method.
2. The structure of the boron-doped carbon nanofibers is inhomogeneous. The local structure is intimately correlated with the boron distribution and their imposing strain.

Based upon this knowledge we have proposed a model for nanotube/nanofiber growth that potentially provides effective control on the structure and chemistry of the boron-doped carbons.

Appendix A: The Synthesis Conditions of Boron-doped Carbon Nanofibers of Group I and Group II

Sample No.	Material	Deposition Temp. & Time	Catalyst	Flow rate and Partial Pressure		Annealing	
				Total flow	Total pressure		
Group I	I-1	B-doped C nanofibers	800°C 30min	Ni film 4.2 nm	65 ml/min 93.5 kPa	10: 10: 45	900°C for 50 h in He
	I-2	B-doped C nanofibers	800°C 30min	Ni film ~4 nm	65 ml/min 93.5 kPa	10: 5: 50	900°C for 50 h in He
	I-0.5	B-doped C nanofibers	800°C 30min	Ni film 4.2 nm	65 ml/min 93.5 kPa	10: 20: 35	900°C for 50 h in He
Group II	II-750C	B-doped C nanofibers	750°C 30min	Ni film 5 nm	60 ml/min 93.5 kPa	10: 17: 33	900°C for 10 h in He
	II-800C	B-doped C nanofibers	800°C 30min	Ni film 5 nm	60 ml/min 93.5 kPa	10: 17: 33	900°C for 10 h in He
	II-850C	B-doped C nanofibers	850°C 30min	Ni film 5 nm	60 ml/min 93.5 kPa	10: 17: 33	900°C for 10 h in He
	II-900C	B-doped C fibers	900°C 30min	Ni film 5 nm	60 ml/min 93.5 kPa	10: 17: 33	900°C for 10 h in He
A	B-doped C film	750°C 8h	N/A	35 ml/min 93.5 kPa	4: 4: (He) 27	900°C for 20 h in He	
B	Carbon nanofibers	800°C 30min	Ni film 4.2 nm	65 ml/min 93.5 kPa	0: 10: 55	900°C for 24 h in He	